

NASA Contractor Report 4679

11-14
67020
p. 153

Advanced k-epsilon Modeling of Heat Transfer

Okey Kwon and Forrest E. Ames

CONTRACT NAS3-25950
JULY 1995



National Aeronautics and
Space Administration

N95-31423

Unclas

H1/34 0057854

(NASA-CR-4679) ADVANCED K-EPSILON
MODELING OF HEAT TRANSFER Final
Report (Allison Engine Co.) 153 p

NASA Contractor Report 4679

Advanced k-epsilon Modeling of Heat Transfer

Okey Kwon and Forrest E. Ames
Allison Engine Company
Indianapolis, Indiana

Prepared for
Lewis Research Center
under Contract NAS3-25950



National Aeronautics and
Space Administration

Office of Management

Scientific and Technical
Information Program

1995

Table of Contents

Table of Contents	iii
List of Figures	v
List of Tables	xi
Nomenclature	xii
Summary	1
I. Introduction	3
II. Analysis	6
1. Boundary Layer Equations	6
2. k- ϵ Transport Equations and Base k- ϵ Low Reynolds Number Turbulence Model	8
3. $v'l$ Formulations	12
(1) $v'l$ -I Closure Model	12
(2) $v'l$ -II Closure Model	16
III. Computation Results and Discussions	24
1. Two-dimensional Fully Developed Turbulent Channel Flows	24
(1) For $Re_\tau = 395$	24
(2) For $Re_\tau = 180$	25
2. Flat Plate Turbulent Boundary Layers	26
3. Turbulent Boundary Layers Developing with Favorable Pressure Gradient	28
(1) Mild Favorable Pressure Gradient Flow: Flow 2700	29
(2) Strong Favorable Pressure Gradient Flow: Flow 2800	29
4. Turbulent Boundary Layers Developing in Adverse Pressure Gradient	30
(1) Mild Adverse Pressure Gradient Flow: Flow 2500	31
(2) Moderate Adverse Pressure Gradient Flow: Flow 2600	32
(3) Flow Under the Sudden Application of an Adverse Pressure Gradient: Flow 3300	33
(4) Samuel-Joubert Flow	34
5. Turbulent Boundary Layer Heat Transfer	35
6. Turbine Airfoil Heat Transfer	37
(1) C3X Airfoil Heat Transfer Measured by Ames	42
(2) C3X Airfoil Heat Transfer Measured by Turner, et al.	43
(3) VKI Airfoil Heat Transfer Measured by Arts, et al.	45
IV. Conclusions	113
References	115
Appendix A. Initial Profiles	119
1. Laminar Flow	119
2. Turbulent Flow	121
Appendix B. Airfoil Surface Velocities	124
1. C3X Airfoil Measured by Ames	124
2. C3X Airfoil Measured by Turner, et al.	126
3. VKI Airfoil Measured by Arts, et al.	128

(1)	For MUR129, 217, and 235	128
(2)	For MUR224, 226, and 228	130
(3)	For MUR239, 245, and 247	132
(4)	For MUR232	134
(5)	For MUR237	136

List of Figures

2.1	Comparison of DNS v'^+ with various models for zero pressure gradient boundary layer at $Re_\theta = 1410$	20
2.2	Comparison of DNS mixing length with linear model for a zero pressure gradient boundary layer at $Re_\theta = 1410$	21
2.3	Comparison of DNS mixing length with $v'l$ -I model for a zero pressure gradient boundary layer at $Re_\theta = 1410$	22
2.4	Comparison of DNS mixing length with $v'l$ -II model for a zero pressure gradient boundary layer at $Re_\theta = 1410$	23
3.1	Comparison of mean velocity profiles predicted by using various k- ϵ based turbulence models with DNS data for a two-dimensional fully developed turbulent channel flow at $Re_\tau = 395$	47
3.2	Comparison of turbulent kinetic energy profiles predicted by using various k- ϵ based turbulence models with DNS data for a two-dimensional fully developed turbulent channel flow at $Re_\tau = 395$	48
3.3	Comparison of dissipation rate profiles predicted by using various k- ϵ based turbulence models with DNS data for a two-dimensional fully developed turbulent channel flow at $Re_\tau = 395$	49
3.4	Comparison of turbulent shear stress profiles predicted by using various k- ϵ based turbulence models with DNS data for a two-dimensional fully developed turbulent channel flow at $Re_\tau = 395$	50
3.5	Comparison of normal component velocity profiles predicted by using various k- ϵ based turbulence models with DNS data for a two-dimensional fully developed turbulent channel flow at $Re_\tau = 395$	51
3.6	Comparison of mean velocity profiles predicted by using the $v'l$ -I, $v'l$ -II, and base k- ϵ turbulence models with DNS data for a two-dimensional fully developed turbulent channel flow at $Re_\tau = 180$	52
3.7	Comparison of turbulent kinetic energy profiles predicted by using the $v'l$ -I, $v'l$ -II, and base k- ϵ turbulence models with DNS data for a two-dimensional fully developed turbulent channel flow at $Re_\tau = 180$	53
3.8	Comparison of dissipation rate profiles predicted by using the $v'l$ -I, $v'l$ -II, and base k- ϵ turbulence models with DNS data for a two-dimensional fully developed turbulent channel flow at $Re_\tau = 180$	54
3.9	Comparison of wall skin friction coefficients predicted by using the $v'l$ -I, $v'l$ -II, and base k- ϵ turbulence models with measured data for a two-dimensional zero pressure gradient turbulent boundary layer	55
3.10	Comparison of mean velocity profiles predicted by using various	

	k- ϵ based turbulence models with Spalart's DNS data for a two-dimensional zero pressure gradient turbulent boundary layer at $Re_\theta = 1410$	56
3.11	Comparison of mean velocity profiles predicted by using the $v'l$ -I, $v'l$ -II, and base k- ϵ turbulence models with measured data and the Clauser curve ($\kappa = 0.41$, $A = 5.0$) for a two-dimensional zero pressure gradient turbulent boundary layer at $Re_\theta = 6,228$ and $14,703$	57
3.12	Comparison of turbulent kinetic energy profiles predicted by using various k- ϵ based turbulence models with Spalart's DNS data for a two-dimensional zero pressure gradient turbulent boundary layer at $Re_\theta = 1410$	58
3.13	Comparison of dissipation rate profiles predicted by using various k- ϵ based turbulence models with Spalart's DNS data for a two-dimensional zero pressure gradient turbulent boundary layer at $Re_\theta = 1410$	59
3.14	Comparison of shear stress profiles predicted by using various k- ϵ based turbulence models with Spalart's DNS data for a two-dimensional zero pressure gradient turbulent boundary layer at $Re_\theta = 1410$	60
3.15	Comparison of normal component turbulent velocity profiles predicted by using the $v'l$ -I and $v'l$ -II models with Spalart's DNS data for a two-dimensional zero pressure gradient turbulent boundary layer at $Re_\theta = 1410$	61
3.16	Comparison of mean velocity profiles predicted by using various k- ϵ based turbulence models with measured data and the Clauser curve ($\kappa = 0.41$, $A = 5.0$) for an equilibrium boundary layer with favorable pressure gradient (Herring and Norbury measurements: Flow 2700) at $x = 0.0$ m	62
3.17	Comparison of mean velocity profiles predicted by using various k- ϵ based turbulence models with measured data for an accelerating flow (Herring and Norbury measurements: Flow 2800) at $x = 0.0$ m	63
3.18	Comparison of wall skin friction coefficients predicted by using various k- ϵ based turbulence models with measured data for an equilibrium boundary layer with favorable pressure gradient (Herring and Norbury measurements: Flow 2700)	64
3.19	Comparison of mean velocity profiles predicted by using various k- ϵ based turbulence models with measured data and the Clauser curve ($\kappa = 0.41$, $A = 5.0$) for an equilibrium boundary layer with favorable pressure gradient (Herring and Norbury measurements: Flow 2700) at $x = 1.524$ m	65
3.20	Comparison of mean velocity profiles predicted by using various k- ϵ based turbulence models with measured data for an equilibrium	

	boundary layer with favorable pressure gradient (Herring and Norbury measurements: Flow 2700) at $x = 1.524$ m	66
3.21	Comparison of wall skin friction coefficients predicted by using various k - ϵ based turbulence models with measured data for an accelerating flow (Herring and Norbury measurements: Flow 2800)	67
3.22	Comparison of mean velocity profiles predicted by using various k - ϵ based turbulence models with measured data and the Clauser curve ($\kappa = 0.41$, $A = 5.0$) for an accelerating flow (Herring and Norbury measurements: Flow 2800) at $x = 1.219$ m	68
3.23	Comparison of mean velocity profiles predicted by using various k - ϵ based turbulence models with measured data for an accelerating flow (Herring and Norbury measurements: Flow 2800) at $x = 1.219$ m	69
3.24	Freestream velocity distributions for Bradshaw's experiments of flow 2500, 2600, and 3300. The solid lines represent the approximated distributions used in the calculations	70
3.25	Freestream velocity distributions for the experimental data set of Samuel and Joubert. The solid line represents the approximated distribution used in the calculations	71
3.26	Comparison of wall skin friction coefficients predicted by using various k - ϵ based turbulence models with measured data for an equilibrium boundary layer with adverse pressure gradient (Bradshaw measurements: Flow 2500)	72
3.27	Comparison of mean velocity profiles predicted by using various k - ϵ based turbulence models with measured data for an equilibrium boundary layer with adverse pressure gradient (Bradshaw measurements: Flow 2500) at $x = 0.610$ m, 1.219 m, and 2.134 m	73
3.28	Comparison of mean velocity profiles predicted by using various k - ϵ based turbulence models with measured data for an equilibrium boundary layer with adverse pressure gradient (Bradshaw measurements: Flow 2500) at $x = 0.610$ m, 1.219 m, and 2.134 m	74
3.29	Comparison of wall skin friction coefficients predicted by using various k - ϵ based turbulence models with measured data for an equilibrium boundary layer with adverse pressure gradient (Bradshaw measurements: Flow 2600)	75
3.30	Comparison of mean velocity profiles predicted by using various k - ϵ based turbulence models with measured data for an equilibrium boundary layer with adverse pressure gradient (Bradshaw measurements: Flow 2600) at $x = 0.584$ m and 2.108 m	76
3.31	Comparison of mean velocity profiles predicted by using various k - ϵ based turbulence models with measured data for an equilibrium boundary layer with adverse pressure gradient (Bradshaw measurements: Flow 2600) at $x = 0.584$ m, 1.194 m, and 2.108 m	77
3.32	Comparison of wall skin friction coefficients predicted by using	

	various k- ϵ based turbulence models with measured data for a boundary layer with sudden adverse pressure gradient (Bradshaw measurements: Flow 3300)	78
3.33	Comparison of mean velocity profiles predicted by using various k- ϵ based turbulence models with measured data for a boundary layer with sudden adverse pressure gradient (Bradshaw measurements: Flow 3300) at $x = 0.610$ m, 1.219 m, and 2.134 m	79
3.34	Comparison of mean velocity profiles predicted by using various k- ϵ base turbulence models with measured data for a boundary layer with sudden adverse pressure gradient (Bradshaw measurements: Flow 3300) at $x = 0.610$ m, 1.219 m, and 2.134 m	80
3.35	Comparison of skin friction coefficients predicted by using various k- ϵ based turbulence models with measured data for an increasingly adverse pressure gradient flow of Samuel and Joubert	81
3.36	Comparison of shape parameter distributions predicted by using various k- ϵ based turbulence models with measured data for an increasingly adverse pressure gradient flow of Samuel and Joubert	82
3.37	Comparison of mean velocity profiles predicted by using various k- ϵ based turbulence models with measured data for an increasingly adverse pressure gradient flow of Samuel and Joubert at $x-x_1 = 0.935$ m and 2.535 m	83
3.38	Comparison of mean velocity profiles predicted by using various k- ϵ based turbulence models with measured data for an increasingly adverse pressure gradient flow of Samuel and Joubert at $x-x_1 = 0.935$ m and 2.535 m	84
3.39	Comparison of kinetic energy and v'^2 profiles predicted by using various k- ϵ based turbulence models with measured data for an increasingly adverse pressure gradient flow of Samuel and Joubert at $x-x_1 = 0.935$ m	85
3.40	Comparison of kinetic energy and v'^2 profiles predicted by using various k- ϵ based turbulence models with measured data for an increasingly adverse pressure gradient flow of Samuel and Joubert at $x-x_1 = 2.535$ m	86
3.41	Comparison of shear stress profiles predicted by using various k- ϵ based turbulence models with measured data for an increasingly adverse pressure gradient flow of Samuel and Joubert at $x-x_1 = 0.935$ m	87
3.42	Comparison of shear stress profiles predicted by using various k- ϵ based turbulence models with measured data for an increasingly adverse pressure gradient flow of Samuel and Joubert at $x-x_1 = 2.535$ m	88
3.43	Comparison of surface heat transfer distributions calculated using the $v'l$ -I, $v'l$ -II, and base k- ϵ turbulence models with measured data for a uniformly heated flat plate ($Re_{L=1} = 1.0 \times 10^6$ and 2.0×10^6)	89

3.44	Comparison of mean velocity and temperature profiles predicted by using the $v'l$ -I, $v'l$ -II, and base k - ϵ turbulence models with measured data for a uniformly heated flat plate ($Re_{L=1} = 1.0 \times 10^6$; $Re_\theta = 3,350$; $Re_\delta = 3,540$)	90
3.45	Comparison of surface heat transfer distributions calculated using various k - ϵ based turbulence models with measured data for a uniformly heated flat plate ($Re_{L=1} = 0.38 \times 10^6$; $Tu = 19\% - 7\%$)	91
3.46	Comparison of surface heat transfer distributions calculated using various k - ϵ based turbulence models with measured data for a uniformly heated flat plate ($Re_{L=1} = 0.75 \times 10^6$; $Tu = 19\% - 7\%$)	92
3.47	Comparison of surface heat transfer distributions calculated using various k - ϵ based turbulence models with measured data for a uniformly heated flat plate ($Re_{L=1} = 1.4 \times 10^6$; $Tu = 19\% - 7\%$)	93
3.48	Comparison of mean velocity and temperature profiles predicted by using the $v'l$ -I, $v'l$ -II, and base k - ϵ turbulence models with measured data for a uniformly heated flat plate ($Re_{L=1} = 0.38 \times 10^6$, 0.75×10^6 , and 1.4×10^6 ; $Tu = 19\% - 7\%$) at $x = 2.13$ m	94
3.49	Comparison of correlations for detecting the laminar-turbulent transition onset	95
3.50	Evaluation of the laminar-turbulent transition and heat transfer augmentation models in the presence of the freestream turbulence. The data were measured by Turner, et al. from a C3X airfoil at the condition of $Re_{C2} = 2.0 \times 10^6$, $M_1 = 0.16$, $M_2 = 0.9$, and $Tu = 6.55\%$	96
3.51	Evaluation of the heat transfer augmentation model in the presence of the freestream turbulence. The data were measured by Ames from a C3X airfoil at the condition of $Re_{C2} = 0.8 \times 10^6$, $M_1 = 0.08$, $M_2 = 0.27$, $Tu = 1\% - 8\%$, and $Lu = 1.3$ cm - 6.6 cm	97
3.52	C3X vane geometry as setup in cascade (Ames' measurements)	98
3.53	Comparison of airfoil surface pressures computed using a stream function analysis with measured data for a C3X vane at $M_2 = 0.27$	99
3.54	Comparison of measured and computed surface heat transfer distributions for a C3X vane at $Re_{C2} = 0.8 \times 10^6$, $M_1 = 0.08$, $M_2 = 0.27$, and $Tu = 1 - 12\%$. The computed data were obtained by using the $v'l$ -I model	100
3.55	Comparison of measured and computed surface heat transfer distributions for a C3X vane at $Re_{C2} = 0.8 \times 10^6$, $M_1 = 0.08$, $M_2 = 0.27$, and $Tu = 1 - 12\%$. The computed data were obtained by using the $v'l$ -II model	101

3.56	C3X vane geometry as setup in cascade (Turner, et al. measurements)	102
3.57	Comparison of airfoil surface velocities computed using an Euler analysis with measured data for a C3X vane at $M_2 = 0.9$, $Re_{C2} = 2.0 \times 10^6$	103
3.58	Comparison of C3X airfoil surface heat transfer coefficients computed with measured surface temperatures and uniform surface temperatures at $Re_{C2} = 2.0 \times 10^6$, $M_1 = 0.16$, $M_2 = 0.9$, and $Tu = 6.55\%$. The computed data were obtained by using the $v'l$ -I model	104
3.59	Comparison of computed C3X airfoil surface heat transfer coefficients with measured data at $Re_{C2} = 1.5 \times 10^6$, 2.0×10^6 , and 2.6×10^6 ; $M_1 = 0.16$; $M_2 = 0.9$; and $Tu = 6.55\%$	105
3.60	VKI vane geometry as setup in cascade (Arts, et al. measurements)	106
3.61	Comparison of airfoil surface velocities computed using an Euler analysis with measured data for a VKI vane at $M_2 = 0.9$, $Re_{C2} = 1.0 \times 10^6$	107
3.62	Comparison of airfoil surface velocities computed using an Euler analysis with measured data for a VKI vane at $M_2 = 1.02$, $Re_{C2} = 1.0 \times 10^6$	108
3.63	Comparison of computed VKI airfoil surface heat transfer coefficients with measured data at $Re_{C2} = 2.0 \times 10^6$, $M_2 = 0.9$, and $Tu = 1\% - 6\%$	109
3.64	Comparison of computed VKI airfoil surface heat transfer coefficients with measured data at $Re_{C2} = 1.0 \times 10^6$, $M_2 = 0.9$, and $Tu = 1\% - 6\%$	110
3.65	Comparison of computed VKI airfoil surface heat transfer coefficients with measured data at $Re_{C2} = 0.5 \times 10^6$, $M_2 = 0.9$, and $Tu = 1\% - 6\%$	111
3.66	Comparison of computed VKI airfoil surface heat transfer coefficients with measured data at $Re_{C2} = 1.0 \times 10^6$, $Tu = 6\%$, and $M_2 = 0.78 - 1.06$	112

List of Tables

2.1	The Coefficients Employed in the k and ϵ Model Equations	10
2.2	The Closure Coefficients Employed in the $v'l$ -I Model	16
2.3	The Closure Coefficients Employed in the $v'l$ -II Model	19
3.1	Flat Plate Turbulent Boundary Layer Integral Parameters	27
3.2	Boundary Layer Integral Parameters for Bradshaw Equilibrium Boundary Layer Developing in Mild Adverse Pressure Gradient	32
3.3	Boundary Layer Integral Parameters for Bradshaw Turbulent Boundary Layer Subjected to a Sudden Mild Adverse Pressure Gradient	34
3.4	Upstream Flow Conditions for C3X Cascade Heat Transfer Measurements of Ames	43
3.5	Upstream Flow Conditions for C3X Cascade Heat Transfer Measurements of Turner, et al.	44
3.6	Upstream Flow Conditions for VKI Cascade Heat Transfer Measurements of Arts, et al.	46

Nomenclature

Roman symbols

A	Constant in the Clauser curve formulation, Equation (3.1)
a_1	Constant in Equation (2.14)
b_1	Constant in Equation (A-9)
C	Constant in Equations (2.23) and (2.24)
C_D	Constant in Equation (2.36)
C_f	Friction coefficient
C_{f0}	Friction coefficient normalized on the upstream reference velocity
C_L	Constant in the length scale formulation, Equation (2.35)
C_p	Pressure coefficient
c_p	Specific heat
C_{Pr}	Constant in the turbulent Prandtl number correlation, Equation (2.5)
C_T	Constant in the time scale definition, Equation (2.15)
C_{TU}	Constant in the turbulence viscosity formulation, Equation (3.10)
C_{vl}	Constant in the v' formulation, Equation (2.27)
C_{v1}, C_{v2}, C_{v3}	Constants in the formulation of the normal component turbulent velocity, Equations (2.29)-(2.31)
C_x	Axial chord
$C_{\epsilon 1}, C_{\epsilon 2}$	Constants in the ϵ transport equation, Equations (2.13) and (2.14)
$C_{\epsilon 1}^*$	Function of the ratio of the energy production to the energy dissipation, defined by Equation (2.14)
C_μ	Constant in the turbulent viscosity formulations, Equation (2.16)
$E_2(\theta)$	One dimensional energy spectrum of v'
f_D	Damping function defined by Equation (2.36)
f_d	Empirical function defined by Equation (2.26)
f_μ	Damping function defined by Equation (2.17)
f_v	Damping function defined by Equation (2.33)
H	Total enthalpy
H	Boundary layer shape parameter, δ^*/θ
h	Channel half width
h	Heat transfer coefficient
\bar{h}	Enthalpy thickness
k	Kinetic energy
k^+	Nondimensional kinetic energy, k/u_τ^2
k_i	Kinetic energy in the inner region
k_o	Kinetic energy in the outer region
κ	Wavenumber
κ_d	Wavenumber range of main dissipation
k_m	Thermal conductivity

Lu	Energy scale, $\sqrt{(2/3)} k^{3/2}/\epsilon$
L_x	Longitudinal integral scale
L_y	Lateral (Normal to the surface) integral scale
l	Length scale
l_m	Mixing length
l_m^+	Nondimensional mixing length, $l_m u_\tau/\nu$
l_0	Length scale away from the wall
M_1	Mach number at the inlet
M_2	Mach number at the exit
P	Energy production rate
p	Static pressure
Pe_t	Turbulent Peclet number
Pr	Prandtl number
Pr_{eff}	Effective Prandtl number
P_{22}	Velocity-pressure gradient correlation + term related to dissipation tensor
q_w''	Wall heat flux rate
R	Gas constant
Re_{C2}	Reynolds number based on the airfoil chord and the airfoil exit flow condition
Re_h	Reynolds number based on the enthalpy thickness
$Re_{L=1}$	Reynolds number based on the unit length
Re_x	Reynolds number based on the longitudinal distance
Re_{δ^*}	Reynolds number based on the displacement thickness
Re_θ	Reynolds number based on the momentum thickness
$Re_{\theta t}$	Momentum thickness Reynolds number at the transition onset
Re_τ	Reynolds number based on the friction velocity and the channel half width
Re_y	Reynolds number defined by Equation (2.18)
s	airfoil surface arc length
St	Stanton number
T	Temperature or time scale defined by Equation (2.15)
T^+	Nondimensional temperature, $(T - T_w) u_\tau/[U_e St (T_e - T_w)]$
Tu	Freestream turbulence intensity
T_0	Freestream total temperature
U	Streamwise mean velocity
U^+	Nondimensional mean velocity, U/u_τ
u_τ	Friction velocity
u'	RMS streamwise fluctuation velocity
V	Cross stream mean velocity
v'	RMS normal fluctuation velocity
v'_i	RMS normal fluctuation velocity in the near wall region
w'	RMS spanwise fluctuation velocity
x	Horizontal coordinate

x_0	Unheated starting length
x_i	Longitudinal coordinate at the calculation start location
y	Vertical coordinate
y^+	Nondimensional vertical coordinate, $y u_\tau / \nu$
Δx	Grid size in the streamwise direction, $x_i - x_{i-1}$
Δy	Grid size in the vertical direction, $y_j - y_{j-1}$

Greek symbols

α	Constant in the freestream velocity correlation
β	Equilibrium parameter, $(\delta^*/\tau_w) dp/dx$
β_K	Nondimensional strain rate defined by Equation (2.22)
δ	Boundary layer thickness
δ^*	Displacement thickness
δ_T	Thermal boundary layer thickness
ε	Dissipation rate
ε^+	Nondimensional dissipation rate, $\varepsilon \nu / u_\tau^4$
ε_ν	Viscous dissipation rate defined by Equation (2.25)
γ_t	Intermittency factor for the laminar-turbulent transition
γ_{TU}	Intermittency factor for the laminar augmentation
η_K	Kolmogorov length scale
θ	Momentum thickness
κ	von Karman Constant
Λ	Acceleration parameter defined by Equation (A-2)
μ	Molecular viscosity
μ_{eff}	Effective viscosity
μ_{TU}	Turbulence viscosity
ν	Kinematic viscosity
ρ	Density
ρ'	Density fluctuation
σ_k	Empirical constant in the turbulent kinetic energy model equation, Equation (2.12)
σ_ε	Empirical constant in the dissipation rate model equation, Equation (2.13)
τ	Shear stress
τ_K	Kolmogorov time scale
τ_{22}	Lagrangian integral time scale

Subscripts

e	Boundary layer edge
i	Grid index in the horizontal direction
j	Grid index in the vertical direction
1	Grid point on the wall
2	Grid point next to the wall
in	Calculation start location
t	Turbulent flow
w	Wall
∞	Upstream infinity

Summary

Gas side heat transfer on a turbine airfoil is difficult to predict because of complex flow characteristics. The turbulence in turbine passage flow is often non-equilibrium and anisotropic, due to high freestream turbulence levels and strong pressure gradients. Conventional k - ϵ turbulence models, which are currently most widely used in the turbine gas path heat transfer prediction, can't provide correct analyses for anisotropic flows since they have no proper mechanism to deal with such an anisotropic turbulence behavior. Under the high turbulence environment, they mostly overpredict mixing inside the wall boundary layer. Recent experimental studies indicate that the influence of freestream turbulence on the boundary layer development is reduced significantly, due to the strong attenuation of the normal component of turbulence by the wall. A proper modeling, therefore, should implement the wall attenuation of the normal component of turbulence.

Lately in the turbulence modeling community, substantial efforts were directed to developing physically sound k - ϵ base models by incorporating experimental findings. The local anisotropy was implemented to a limited extent into some of the newly developed models. Attempts have been made to model the normal component turbulence fluctuation separately instead of evaluating it directly from the kinetic energy. Such efforts eliminated the 'ad hoc' damping function, but caused an additional modeling complexity. Furthermore, the success of such models for non-equilibrium anisotropic flows was still relatively limited.

This report describes two approaches to low Reynolds number k - ϵ modeling which formulate the eddy viscosity on the normal component of turbulence and a length scale. The normal component of turbulence is modeled based on the dissipation and distance from the wall and is bounded by the isotropic condition. The models account for the anisotropy of the dissipation and the reduced length of mixing due to the high strain rates present in the near wall region. The kinetic energy and dissipation rate were computed from the k and ϵ transport equations of Durbin. The models were tested for a wide range of turbulent flows and proved to be superior to other k - ϵ based models. They were also applied to turbine airfoil heat transfer prediction. For this task, the models implemented a set of empirical correlations for predicting laminar-turbulent transition and the laminar heat transfer augmentation due to the presence of the freestream turbulence.

In addition, the conventional eddy viscosity closure model, which provided a basis to the velocity and length scale closure model, is also presented. The model is formulated by combining the k and ϵ transport equations of Durbin and the eddy viscosity formulation of Yang and Shih. This kinetic energy and time base formulation of eddy

viscosity closure modeling features a singularity-free wall condition and provides good prediction capability compared to conventional low Reynolds number k - ϵ models.

I. Introduction

In the design and development of high performance gas turbines, cooling is an important factor as thermal protection is required for the components which are exposed to gas temperature far above the allowable metal temperatures. In particular, the turbine blades and vanes must be cooled in order to insure their reasonable lifetime by keeping their surface temperature relatively uniform and below critical limits. The cooling, however, often causes penalties to the engine cycle through the process of extraction of compressed potential working fluid and reintroduction of the cooler, low momentum coolant into the hotter high velocity mainstream. Therefore, accurate estimates of the rates of heat transfer from the gas stream to the airfoil and from the airfoil to the coolant are prerequisites for accomplishing effective cooling with the smallest possible penalty[1].

Difficulty in modeling the complex flow physics properly causes uncertainties in predicting hot gas side heat transfer rates on the turbine airfoil, which are critical in a cooling design. Although significant progress has been made lately in the development of direct numerical simulations (DNS), they are still impractical for the designers' use. The most common approach of heat transfer prediction today is to establish a framework computer code with the time-averaged governing equations and augment it with turbulence models [2]. The development of accurate turbulence models is, therefore, critical to transition turbine design from a mix of modeling and empiricism to a procedure more reliant on computational tools.

The existing turbulence models are based on physics and generally perform well for fully turbulent conditions. Among the turbulence models, two-equation $k-\epsilon$ (base) models are most popular in predicting turbine gas path heat transfer because of their capability of predicting a wide range of flows with minimal adjustment of the coefficients and their relative simplicity in formulation. The standard $k-\epsilon$ model was first introduced by Launder and Spalding for high Reynolds number turbulent flows[3]. The model requires wall functions for wall bounded turbulent flows, which often results in solution inaccuracies for complex flows. As an effort to overcome this deficiency, low Reynolds number $k-\epsilon$ models, which permit a direct integration down to the wall, have been developed following the first proposers, Jones and Launder[4]. These low Reynolds number models are generally based on quasi-homogeneous approximations. They require empirical damping functions in order to prevent the model failure near the wall where the turbulence is strongly nonhomogeneous and turbulent mixing is suppressed due to the wall blocking. These damping functions often involving exponential functions are rather arbitrary: they were derived to be consistent with experimental or numerical data for constant pressure boundary layers. Consequently, they are often

blamed for the inaccurate solutions of complex flows. A detailed discussion on the deficiency of the k- ϵ models can be found elsewhere[5].

Lately, the turbulence modeling community has directed a significant effort to developing more physically sound k- ϵ base models. The approaches of a renormalization group (RNG) method [6], the Kolmogorov time scale introduction approach[7] and an elliptic relaxation method for the near wall turbulence blocking effect[8] are among the most significant developments. The RNG k- ϵ model was first derived by Yakhot and Orszag[6] by means of the RNG method which uses dynamic scaling and invariance together with iterated perturbation methods. This theory provided an elimination of experimentally adjustable parameters in the model. A high Reynolds number version of the RNG k- ϵ model was successfully tested for separated flows downstream of a rearward facing step by Speziale and Thangam[9].

Yang and Shih[7] reformulated a low Reynolds number version of a k- ϵ model by introducing the Kolmogorov time scale into the transport equation for the turbulence dissipation rate. With the new time scale, they were able to eliminate the wall singularity of the equation and to keep the same model constants as those used in the standard high Reynolds number model. The model, however, still employs a damping function in the eddy viscosity formulation to account for kinematic blocking by the wall.

The elliptic relaxation model proposed by Durbin[8] was devised for the strongly nonhomogeneous region near the wall. In this model, the wall blocking effect which suppresses the normal component of turbulent intensity was modelled by an elliptic relaxation equation for the redistribution terms in the Reynolds stress equations. Durbin also introduced the 'local anisotropy' term in the dissipation rate equation of this model. The introduction of these two features into the model eliminated the 'ad hoc' damping functions from the model equations, however, at the cost of an increase of the size of the system by two model transport equations: one for the variance of the normal component of turbulent velocity, v'^2 , and another for the velocity-pressure-gradient correlation, p'_{22} .

These new approaches show improved modeling physics and appear to offer the prospect of improved predictions for anisotropic flows. However, they still need to be tested and verified for various practical flows, especially for turbine airfoil heat transfer under high levels of external turbulence at which conventional k- ϵ models fail to accurately respond to the distortion through turbine passages and at solid boundaries. Recent studies (see [10]) indicate that the normal component of turbulence, v' , is a key variable in the prediction of turbine airfoil heat transfer and skin friction, and the magnitude of v' can be tied to the dissipation rate. Durbin[8] also found that the normal fluctuation is a better velocity scale for characterizing the turbulent motion than the

kinetic energy in the near wall shear layer. It is, therefore, logical to formulate the turbulent eddy diffusivity in terms of the local velocity v' , which is modeled as of function of the local dissipation rate and the local length scale.

The objective of this study is to develop a new k - ϵ base model which will provide acceptable engineering answers for a significant range of turbulent flows that are of technological interest. This report presents two different closure models, designated $v'l$ -I and $v'l$ -II models, which formulated the eddy viscosity in terms of the normal component of turbulence, v' , and the length scale, l , based upon the aforementioned experimental observation. The normal component of turbulence, v' , was evaluated from a direct integration of the normal energy spectrum in both formulations; and the length scales from the local distance and a combination of the local distance and the length scale defined by $k^{3/2}/\epsilon$ in the $v'l$ -I and $v'l$ -II formulations, respectively. The kinetic energy, k , and dissipation rate, ϵ , were calculated by using a standard form of k - ϵ model transport equations suggested by Durbin[8].

In this report, a conventional eddy viscosity formulation of a low Reynolds number k - ϵ model is also presented. The model, named the base k - ϵ model, as it provided a basis for the $v'l$ models, was formulated by combining the k - ϵ transport equations of Durbin[8], and the eddy viscosity closure of Yang and Shih[7]. The base model implemented two time scales, the inner Kolmogorov scale and the outer scale of k/ϵ , and the Durbin's local anisotropy term, but included no damping function in the governing transport equations. The base k - ϵ model predicted various turbulent flows well. However, the prediction quality of the base model similar to other k - ϵ models was found to be degraded for non-equilibrium, anisotropic turbulent flows. Both $v'l$ -I and $v'l$ -II models, meanwhile, provided excellent predictions for various turbulent flows including those non-equilibrium, anisotropic turbulent flows considered in this study.

This report also presents correlations for predicting the laminar-turbulent transition and the laminar heat transfer augmentation due to the presence of freestream turbulence. These phenomena are prominent in turbine airfoil heat transfer. Since the $v'l$ closures, like other two-equation models, do not have the capability of predicting these phenomena accurately, such explicit correlations are required for airfoil heat transfer prediction. These additional features can be accommodated in the analysis using the effective viscosity/Prandtl number concept. The analyses presented in this report were made with the steady two-dimensional boundary layer equations.

II. Analysis

1. Boundary Layer Equations.

This study focused on the thin viscous region near a solid wall, called the boundary layer. In the steady two-dimensional boundary layer approximation, with the Reynolds shear stress and heat flux replaced by an "eddy" (or "turbulent") viscosity and a turbulent Prandtl number, the conservation of mass, momentum and energy can be written in the following form.

$$\frac{\partial}{\partial x}(\rho U) + \frac{\partial}{\partial y}(\rho V) = 0 \quad (2.1)$$

$$\rho U \frac{\partial U}{\partial x} + \rho V \frac{\partial U}{\partial y} = -\frac{dP}{dx} + \frac{\partial}{\partial y} \left[\left(\mu + \mu_t \right) \frac{\partial U}{\partial y} \right] \quad (2.2)$$

$$\rho U \frac{\partial H}{\partial x} + \rho V \frac{\partial H}{\partial y} = \frac{\partial}{\partial y} \left[\left(\frac{\mu}{Pr} + \frac{\mu_t}{Pr_t} \right) \frac{\partial H}{\partial y} \right] \quad (2.3)$$

$$+ \frac{\partial}{\partial y} \left\{ \left[\left(\mu + \mu_t \right) - \left(\frac{\mu}{Pr} + \frac{\mu_t}{Pr_t} \right) \right] U \frac{\partial U}{\partial y} \right\}$$

where U and V are the mass-weighted time-averaged mean velocities[11]; μ , the molecular viscosity; Pr , the Prandtl number; H , the total enthalpy; and x and y , the streamwise and normal coordinates. The subscript "t" denotes the turbulent quantity. Assuming that the gas is ideal, the state equation is

$$\rho = \frac{P}{R T} \quad (2.4)$$

where, R denotes the gas constant; and T , the temperature.

The turbulent Prandtl number, Pr_t , in Equation (2.3) is observed experimentally to be approximately 0.9 for air over most of the boundary layer and to increase to well above 1.0 very close to the wall. Therefore, a constant value of approximately 1.0 is often used in heat transfer analyses. This analysis, however, incorporates Kays' correlation[12] developed based on such experimental observations:

$$Pr_t = \left\{ \frac{1}{2Pr_{t\infty}} + C_{Pr} Pe_t \left(\frac{1}{Pr_{t\infty}} \right)^{1/2} - (C_{Pr} Pe_t)^2 \left[1 - \exp \left(- \frac{1}{C_{Pr} Pe_t \sqrt{Pr_{t\infty}}} \right) \right] \right\}^{-1} \quad (2.5)$$

where Pe_t is a turbulent Peclet number defined by the product of the Prandtl number and the turbulent to molecular viscosity ratio; $Pr_{t\infty}$, the turbulent Prandtl number far away from the wall; and C_{Pr} , an experimental constant. For air, $Pr_{t\infty} = 0.86$ and $C_{Pr} = 0.2$ were recommended by Kays.

Using the definition of the effective viscosity and effective Prandtl number, Equations (2.2) and (2.3) can be rewritten as

$$\rho U \frac{\partial U}{\partial x} + \rho V \frac{\partial U}{\partial y} = - \frac{dP}{dx} + \frac{\partial}{\partial y} \left[\mu_{eff} \frac{\partial U}{\partial y} \right] \quad (2.6)$$

$$\begin{aligned} \rho U \frac{\partial H}{\partial x} + \rho V \frac{\partial H}{\partial y} = & \frac{\partial}{\partial y} \left[\frac{\mu_{eff}}{Pr_{eff}} \frac{\partial H}{\partial y} \right] \\ & + \frac{\partial}{\partial y} \left\{ \left[\mu_{eff} - \frac{\mu_{eff}}{Pr_{eff}} \right] U \frac{\partial U}{\partial y} \right\} \end{aligned} \quad (2.7)$$

with

$$\mu_{eff} = \mu + \mu_t \quad (2.8)$$

$$Pr_{eff} = \frac{\mu + \mu_t}{\frac{\mu}{Pr} + \frac{\mu_t}{Pr_t}} \quad (2.9)$$

The system of equations, Equations (2.1), (2.6) and (2.7), are subjected to the following boundary conditions

at $y = 0$,

$$\begin{aligned} U &= 0, \quad V = 0, \quad \text{and} \\ H &= H_w \quad \text{or} \quad \frac{\partial H}{\partial y} = -\left(\frac{c_p}{k_m}\right) \dot{q}_w'' \end{aligned} \quad (2.10)$$

as $y \rightarrow \infty$,

$$U = U_e, \quad \text{and} \quad H = H_e \quad (2.11)$$

where c_p denotes the specific heat; k_m , the thermal conductivity; and \dot{q}_w'' , the rate of the wall heat flux. The subscripts 'w' and 'e' imply the wall and freestream conditions, respectively.

In addition to these boundary conditions, the system of equations requires a set of initial profiles for the velocity and total enthalpy because of its parabolic characteristics. The initial profiles can be specified either by using analytical and empirical correlations (see Appendix A), or by solving the stagnation point similarity equations especially for airfoil analyses (eg. see [13]). Provided that the eddy viscosity is specified, the governing equations then can be solved numerically. Although an implicit finite difference numerical scheme[14] was used in the present study, other numerical procedures also can be employed to solve the governing equations.

2. k- ϵ Transport Equations and Base k- ϵ Low Reynolds Number Turbulence Model.

Conventional low Reynolds number k- ϵ turbulence models suffer from the wall singularity caused by the vanishing time scale of k/ϵ at the wall. Recently, Yang and Shih[7] and Durbin[8] showed that the wall singularity could be eliminated by introducing the Kolmogorov time scale into their k- ϵ base models as the lower bound of the usual time scale in the near wall region. Furthermore, Durbin[8] was able to integrate the standard high Reynolds number form of his k and ϵ transport equations directly down to the wall. The k and ϵ transport equations implemented a local anisotropy term but no 'ad hoc' damping function or additional source terms. Durbin solved the k and ϵ equations in a coupled manner with the wall characteristics of the kinetic energy ($k = \partial k / \partial y = 0$) as the wall boundary conditions to the coupled system of equations (see reference [15]). Although the Durbin model formulates the k and ϵ transport equations in a simple and

singularity-free form, it is more sophisticated as the additional v'^2 - p_{22} system of equations are introduced to model the variance of the normal component of turbulent velocity, v'^2 .

Yang and Shih[7], meanwhile, utilized the conventional eddy viscosity formulation with a damping function which accounts for the wall effect, as practiced commonly in low Reynold number k - ϵ modeling. In addition, their explicit wall dissipation rate boundary condition of $\epsilon_w = 2\nu(\partial k^{1/2}/\partial y)^2$ kept the solution procedure for k and ϵ relatively simple compared to the Durbin model. The k and ϵ model equations of Yang and Shih are simple without having additional pseudodissipation, but they still retain the secondary source term of $\nu v_t(\partial^2 U/\partial y^2)$ in the dissipation rate equation.

The transport equations for the turbulent kinetic energy and the dissipation rate proposed by Durbin[8] were employed in this study because of their aforementioned attractive features of the simple and wall singularity-free formulation. The equations can be written as,

$$\rho U \frac{\partial k}{\partial x} + \rho v \frac{\partial k}{\partial y} = \mu_t \left(\frac{\partial U}{\partial y} \right)^2 - \rho \epsilon + \frac{\partial}{\partial y} \left[\left(\mu + \frac{\mu_t}{\sigma_k} \right) \frac{\partial k}{\partial y} \right] \quad (2.12)$$

$$\begin{aligned} \rho U \frac{\partial \epsilon}{\partial x} + \rho v \frac{\partial \epsilon}{\partial y} = & \frac{1}{T} \left[C_{\epsilon 1}^* \mu_t \left(\frac{\partial U}{\partial y} \right)^2 - C_{\epsilon 2} \rho \epsilon \right] \\ & + \frac{\partial}{\partial y} \left[\left(\mu + \frac{\mu_t}{\sigma_\epsilon} \right) \frac{\partial \epsilon}{\partial y} \right] \end{aligned} \quad (2.13)$$

where k denotes the turbulent kinetic energy; ϵ , the dissipation rate; T , the time scale; and σ_k , σ_ϵ , and $C_{\epsilon 2}$, empirical constants. $C_{\epsilon 1}^*$ is a function of the ratio of the energy production to the energy dissipation, representing the production by local anisotropy. Durbin suggested the following linearized equation for $C_{\epsilon 1}^*$:

$$C_{\epsilon 1}^* = C_{\epsilon 1} \left(1 + a_1 \frac{P}{\epsilon} \right) \quad (2.14)$$

where P is the rate of energy production $\nu_t(\partial U/\partial y)^2$; and $C_{\epsilon 1}$ and a_1 are constants. The time scale is defined by the usual scale, k/ϵ , with the lower bound by the Kolmogorov scale, $(\nu/\epsilon)^{1/2}$, as suggested by Durbin[8]:

$$T = \max \left[\frac{k}{\epsilon}, C_T \left(\frac{\nu}{\epsilon} \right)^{1/2} \right] \quad (2.15)$$

where C_T is a constant. The values of the closure coefficients used in this study for wall-bounded flow predictions are similar to those suggested by Durbin[8]. They are given in Table 1.

Table 2.1. The Coefficients Employed in the k and ϵ Model Equations

C_T	a_1	$C_{\epsilon 1}$	$C_{\epsilon 2}$	σ_k	σ_ϵ
6.0	0.09	1.44	1.9	1.0	1.3

In this study, a conventional eddy viscosity closure, designated the base low Reynolds number k- ϵ model, is formulated by combining the k and ϵ transport equations of Durbin[8] and the eddy viscosity closure of Young and Shih[7]. The base model, therefore, preserves important features of the two models such as the simple, wall singularity-free formulation of k and ϵ model equations and the good prediction capability. This model provides a basis to developing the ν/l closure model. With the base model, the eddy viscosity is given by

$$\mu_t = C_\mu f_\mu \rho k T \quad (2.16)$$

where C_μ is a closure constant; f_μ , the damping function; and T, the time scale. The damping function of Yang and Shih is written as,

$$f_\mu = \left[1 - \exp \left(-1.5 \times 10^{-4} R_y - 5.0 \times 10^{-7} R_y^3 - 1.0 \times 10^{-10} R_y^5 \right) \right]^{1/2} \quad (2.17)$$

where R_y is a Reynolds number defined by

$$R_y = \frac{k^{1/2} y}{\nu} \quad (2.18)$$

Equations (2.17) and (2.18) allow an easy application of the base k - ϵ model to separating/recirculating flows.

The closure constant C_μ is evaluated by using the eddy diffusivity formulation of Durbin[8]. Durbin correlates the eddy diffusivity in terms of the variance of the normal component turbulent velocity and the time scale as $\nu_t = C_\mu' \overline{v'^2} T$, where the constant $C_\mu' = 0.21$. The Spalart's direct numerical simulation data[16] for a turbulent flat plate boundary layer at $Re_\theta = 1410$ shows that the variance of the normal component turbulent velocity, $\overline{v'^2}$, can be approximately correlated to the kinetic energy by $\overline{v'^2} = 0.45 f_\mu k$ as shown in Figure 2.1. Here, the damping function f_μ is evaluated from Equation (2.17). The eddy diffusivity of Durbin, therefore, can be rewritten in terms of the kinetic energy and the time scale as $\nu_t = 0.45 C_\mu' f_\mu k T$. Comparing this to Equation (2.16) leads to $C_\mu = 0.45 C_\mu' = 0.0945$ which is 5% larger than the commonly used value of 0.09.

In order to solve the governing k and ϵ transport equations, appropriate boundary conditions should be imposed on the wall and freestream boundaries along with the initial profiles of k and ϵ upstream of the flow field. At the wall there exists no correct explicit condition of ϵ . As discussed by Durbin[8], the limiting behavior of k and ϵ is $k \rightarrow \epsilon(0)y^2/2\nu$ as $y \rightarrow 0$, which implies $\partial k/\partial y = 0$ at the wall. Therefore, the coupled system of transport equations should be solved in a coupled manner with the wall boundary conditions $k = \partial k/\partial y = 0$ or with the limiting behavior relationship between k and ϵ and the no-slip condition $k = 0$. For the present study, the latter set of the conditions is used since it is slightly less cumbersome to implement with the coupled numerical algorithm. In the freestream, the vanishing normal gradient condition was imposed. The initial profile generation procedures for k and ϵ are described in Appendix A.

The numerical procedure employed was a second order accurate implicit finite difference scheme. The streamwise convective terms were discretized by using a forward differencing algorithm which required data to be stored at the two immediate upstream stations ($i-1$ and $i-2$ in which i denotes the streamwise grid index). The time scale T in Equation (2.15) was evaluated based on the immediate upstream station condition. The wall dissipation rate was approximated from the limiting behavior as

$$\epsilon_{i,1} \equiv \frac{2 v_{i,2} k_{i,2}}{y_{i,2}^2} \quad (2.19)$$

where the subscripts 1 and 2 indicate the wall and next to the wall grid points, respectively, in the normal direction. At the freestream boundary, Equations (2.12) and (2.13) were simplified by applying the vanishing normal gradient conditions and, then, the resulting equations were discretized, instead of imposing the boundary conditions directly. The discretized equations formed a 2x2 block tridiagonal system of equation for the unknown variables k and ϵ at the grid points $(i, j+1)$, (i, j) , and $(i, j-1)$ in which i and j are the grid indexes in the streamwise and cross-streamwise directions, respectively. The system of equations were solved in a coupled manner by using a block tridiagonal solution procedure (see reference [17]). In addition, a secant iteration procedure was introduced to satisfy the approximated limiting wall condition, Equation (2.19)

3. $v'l$ Formulations.

From dimensional reasoning, the eddy viscosity given can be expressed in terms of a turbulent velocity scale and a length scale. For the velocity scale, the normal component turbulent velocity can be used as suggested by Durbin [15]. Durbin found that the normal fluctuation is a better velocity scale for characterizing the turbulent motion than the turbulent kinetic energy in the near-wall shear layers. Ames[10] also observed experimentally that the normal component turbulent velocity is a key variable in the prediction of surface heat transfer and skin friction. Equation (2.16), therefore, can be rewritten as

$$\mu_t = \rho v' l \quad (2.20)$$

where ρ denotes the density; v' , the magnitude of the normal component turbulent velocity; and l , the turbulent length scale. Turbulence studies of Ames[10] also indicate that the magnitude of the v' component of turbulence can be tied to the dissipation rate of the turbulence kinetic energy, and the length scale to a local scale. An approximate relationship between v' and the dissipation rate can be obtained by integrating the normal component power spectrum. Following are the two sets of formulations proposed for the v' component of turbulence and the length scale, designated $v'l$ -I and $v'l$ -II closure models, respectively.

(1) $v'l$ -I Closure Model.

As shown in Equation (2.20), eddy diffusivity has the dimensional units of a fluctuating velocity scale times a length scale. From the simplest physical model, an eddy with a normal fluctuation velocity, v' , takes a mass of fluid from one location in a flow to another a distance l away. If a gradient in a property exists, its diffusion across the flow will be proportional to the gradient times the product of this velocity scale and length scale. Tennekes and Lumley [18] suggested the local eddy diffusivity is roughly equal to the normal variance, v'^2 , times the Lagrangian integral time scale, τ_{22} . Durbin[15] formulated his eddy diffusivity in this manner observing that k - ϵ damping functions are approximately proportional to v'^2/k . Since the Lagrangian integral time scale times the magnitude of v' is the Lagrangian integral scale, this $v'^2\tau_{22}$ formulation of eddy viscosity is equivalently $v'l$.

Near the wall, the Eulerian integral scale is proportional to the normal distance, y , from the wall. Hunt and Graham [19] found this proportionality in their analysis of a shear free turbulent flow. This proportionality provides a simple yet sound way to model the mixing length through the boundary layer and near the wall.

The turbulent boundary layer statistics provided by the direct numerical simulation (DNS) calculation of Spalart [16] offers an opportunity to test the validity of these modeling assumptions. First, the turbulent scale of mixing, l , determined from the DNS data indicates that the distance to the wall constrains the near wall mixing. Figure 2.2 shows a comparison between the mixing length l estimated from the data, by dividing $-\overline{u'v'}$ by y^+ and dU^+/dy^+ , and a line represented by $0.38(y^+-5)$. From $y^+ = 10$ through the logarithmic law region, this mixing length is well represented by the linear relationship of $0.38(y^+-5)$. The offset in this representation in the sublayer region, where $y^+ < 10$, indicates that the turbulent mixing is less effective. The inviscid damping of the wall, viscous dissipation of small eddies, and high near wall strain rates contribute to the fall off of the near wall dependence of mixing length l^+ on y^+ .

In the $v'l$ -I formulation of eddy viscosity, the length scale was correlated based on the DNS data as,

$$l^+ = \kappa \frac{\left(y^+ - \frac{\eta_K}{4}\right)}{\left(1 + 0.4\beta_K\right)} \quad (2.21)$$

where η_K denotes the Kolmogorov length scale defined by $\eta_K = (\nu^3/\epsilon)^{1/4}$; and β_K , a nondimensional strain rate defined by

$$\beta_K = \tau_K \left(\frac{dU}{dy} \right) \quad (2.22)$$

in which the Kolmogorov time scale, τ_K , is defined by $\tau_K = (\nu/\epsilon)^{1/2}$; and the von Karman constant, κ , is set equal to 0.38. Figure 2.3 shows a comparison between l^+ determined from the DNS data, Equation (2.21), and the conventional k- ϵ model length scale of $(3/2)^{1/2} C_\mu k^{3/2}/\epsilon$ (or $0.116 k^{3/2}/\epsilon$ for $C_\mu = 0.0945$ as used for the base k- ϵ model). The conventional length scale can be obtained from the definition of the eddy diffusivity that $\nu_t = \nu' l = C_\mu k^2/\epsilon$. Since $\nu' = \sqrt{(2k/3)}$ for isotropic turbulence, the length scale becomes $l = (3/2)^{1/2} C_\mu k^{3/2}/\epsilon$. The dependence of mixing length with y^+ begins to drop off beyond the logarithmic law region or past a y^+ of about 90 to 100. This slowed growth of l is probably due to the intermittency of turbulent and freestream fluid in this region. Modeling l in this region can be readily accomplished by using the minimum of l and the k- ϵ formulation of mixing length, $0.116 k^{3/2}/\epsilon$.

Based on both experimental study of Thomas and Hancock [20] and analytical studies of Hunt and Graham [19] and Spalart [16], ν' is strongly attenuated by the wall. Modeling ν' can be accomplished by developing a model spectrum based on the dissipation rate. Energy from the attenuation of larger scale eddies due to wall blocking can be modeled by scaling a large scale cutoff wavenumber on $1/y$. The high wavenumber cutoff due to viscous effects can be based on the Kolmogorov length scale, η_K . In the inertial subrange of the ν' spectra can be modeled from the dissipation rate and the wave number,

$$E_2(\kappa) = C \epsilon^{2/3} \kappa^{-5/3} \quad (2.23)$$

where E_2 denotes the one dimensional energy spectrum of ν' ; ϵ , the dissipation rate; κ , the wavenumber; and C , a constant.

Substituting $1/y$ for the high wave number cutoff and $1/\eta_K$ for the low wavenumber cutoff, a simple spectrum model for ν'^2 becomes,

$$\nu'^2 = C \epsilon^{2/3} \left(2.5 y^{2/3} - 1.5 \eta_K^{2/3} \right) \quad (2.24)$$

Unfortunately, the viscous dissipation becomes highly anisotropic near the wall, particularly below a y^+ of 20 to 30. The anisotropy of ϵ can be modeled using an ϵ damping function. The damping function uses a nondimensionalized strain rate, β_K , to provide the majority of the damping and an exponential term to give the proper near wall dependence:

$$\epsilon_v = \epsilon \frac{\left[1 - \exp\left(-\frac{y}{1.2 \eta_K}\right) \right]^5}{\left(1 + 2\beta_K + 5\beta_K^2 + \beta_K^4 \right)} \quad (2.25)$$

The exponential term in Equation (2.25) is introduced to achieve a correct near wall limiting behavior of v' and its effect on the analysis is generally small. The variable β_K nondimensionalizes the strain rate using the Kolmogorov time scale, τ_K . This is an attempt to correlate the influence of strain on the attenuation of v' in the sublayer. The strain rate also correlates with anisotropy of ϵ through the near wall dissipation of u' and w' which are highly anisotropy.

A primary purpose of this $v'l$ model is to deal with the influence of large scale high intensity external turbulence on the boundary layer development. Based on experimental data showing the attenuation of v' outside the boundary layer (see Ames and Moffat [21]), the constant of proportionality between v' and $\epsilon^{1/3}$ changes between the logarithmic law layer and the outer region of the boundary layer. The following function is used across the boundary layer to change this proportionality:

$$f_d = \frac{1. + C \cdot 10^{-4} - \exp\left[-C \left(1.25 \frac{y}{\delta}\right)^4\right]}{1. + 1 \cdot 10^{-4} - \exp\left[-\left(1.25 \frac{y}{\delta}\right)^4\right]} \quad (2.26)$$

where δ denotes the boundary layer thickness where the mean velocity is 99% of the freestream velocity. For the calculations contained in this report, C was set equal to 2.85 but comparisons of v' profiles indicated that setting f_d a constant value of 2.85 produced better v' distributions for most cases and made little difference in the resulting calculations. The representation for v' is the following of dissipation, strain rate, and relative position through the boundary layer:

$$v' = C_{vl} f_d \left[\epsilon_v^{2/3} \left(2.5 y^{2/3} - 1.5 \eta_K^{2/3} \right) \right]^{1/2} \quad (2.27)$$

where the constant C_{vl} is set equal to 0.205. The DNS data of Spalart's was used to develop these formulas and Figure 2.1 shows a comparison between Spalart's v'^+ statistics and the equation for v' given above. The dissipation rate and strain rate statistics taken from the DNS data were used to develop the v' distribution.

The turbulent viscosity, μ_t , can be calculated from Equation (2.20) along with Equations (2.21) and (2.27). However, in order to bound v' and l in y , a check is made to ensure that μ_t obtained from Equation (2.20) is less than that from the formulation given below for the k - ϵ model:

$$\mu_t = C_\mu \rho \frac{k^2}{\epsilon} \quad (2.28)$$

where the constant C_μ is set equal to 0.0945 as used for the base k - ϵ model. Furthermore, v' is also bounded by $(2k/3)^{1/2}$ as an isotropic condition. The closure coefficients of the v' - l -I model are summarized in Table 2.2.

Table 2.2. The Closure Coefficients Employed in the v' - l -I Model

C_{vl}	C_μ	κ
0.205	0.0945	0.38

(2) v' - l -II Closure Model.

In the previous section, a correlation was developed between the variance of the normal component turbulent velocity and the local dissipation rate by integrating the normal component energy spectrum in the region of the inertial subrange. The correlation, Equation (2.24), can be applied to the whole flow field except for a narrow region adjacent to the wall of which the width is approximately half of the Kolmogorov length scale. Since this narrow region is dominated by the overwhelming effects of the

viscosity, the velocity fluctuation does not contribute much to the total stress. Therefore, in this region, an approximation of zero normal component turbulent velocity can be used as done with the $v'l$ -I model. Another approximation might be applying Equation (2.24) away from the wall where the normal distance from the wall is substantially larger than the Kolmogorov length scale, and limiting the magnitude of normal fluctuations in the near wall region with the geometric constraint and flow characteristics. This approach leads to simpler formulations for the velocity and length scales than the previous $v'l$ -I model.

In the region away from the wall where the transverse distance from the wall is substantially larger than the Kolmogorov length scale, Equation (2.24) can be simplified as

$$v'^2 = C_{v1} \epsilon^{2/3} y^{2/3} \quad (2.29)$$

where C_{v1} denotes a constant; ϵ , the dissipation rate; and y , the transverse distance from the wall. The magnitude of the normal component velocity becomes

$$v' = C_{v2} \epsilon^{1/3} y^{1/3} \quad (2.30)$$

In the near-wall region, the normal component turbulence velocity can be approximated by the constraint of the local transverse distance, y , from the wall divided by the local Kolmogorov time scale, τ_K . That is,

$$v'_i = C_{v3} \frac{y}{\tau_K} \quad (2.31)$$

where τ_K denotes the Kolmogorov time scale; and C_{v3} , a constant. The comparison with the direct numerical simulation (DNS) of Spalart [16] for a turbulent flat plate boundary layer at $Re_\theta = 1410$ showed that Equation (2.31) can be a reasonable representation of the normal component of fluctuations in the near wall region. However, in order to achieve a proper asymptotic behavior of v' , an empirical function was introduced as

$$v'_i = C_{v3} f_v \frac{y}{\tau_K} \quad (2.32)$$

with

$$f_v = 1 - \exp\left(-\frac{y}{\eta_K}\right) \quad (2.33)$$

where f_v denotes an empirical function; and η_K , the Kolmogorov length scale. As the wall is approached, f_v in Equation (2.33) behaves as $f_v \propto y$. The normal component turbulent velocity, therefore, becomes $v' \propto y^2$, as $y \rightarrow 0$. Since the empirical function, f_v , applies to the region close to the wall where the viscosity effect is overwhelming, it provides a negligible effect on the analysis.

Combining Equations (2.30) and (2.32) leads to the following expression for the normal component of turbulent velocity across the boundary layer:

$$v' = \min\left(C_{v2} \epsilon^{1/3} y^{1/3}, C_{v3} f_v \frac{y}{\tau_K}\right) \quad (2.34)$$

The closure constants C_{v2} and C_{v3} are set equal to 0.738 and 0.0967, respectively, based on the comparison with direct numerical simulation (DNS) data of Spalart[16] for a turbulent flat plate boundary layer at $Re_\theta = 1410$ (see Figure 2.1). For the wall bounded shear layer, v' outside of the boundary layer is set equal to the boundary layer edge value, that is, $v' = C_{v2} \epsilon^{1/3} \delta^{1/3}$.

As shown in Figure 2.2, the length scale away from the wall, l_o , can be written as

$$l_o = C_L \frac{k^{3/2}}{\epsilon} \quad (2.35)$$

where C_L denotes a constant; k , the turbulence kinetic energy; and ϵ , the dissipation rate. In the near wall region where $y^+ < 50$, Equation (2.35) overestimates the mixing length. The following empirical function, therefore, was introduced to match the near wall length scale obtained from Equation (2.35) to the DNS data of Spalart[19]:

$$f_D = \min \left[C_D \left(\frac{y}{\eta_K}\right)^{4/3}, 1.0 \right] \quad (2.36)$$

where C_D denotes a constant; y , the normal distance from the wall; and η_K , the Kolmogorov length scale. Equation (2.36) was developed based on the observation of the energy spectrum characteristics at high wavenumbers. According to Pao (see

Hinze[22]), the rapid decay of energy spectra at high wavenumbers can be written in the form of $\exp[-1.5 A (\kappa / \kappa_d)^{4/3}]$ in which A denotes a constant; κ , the wavenumber; and κ_d , the wavenumber range of main dissipation. Since $\kappa_d = 1 / \eta_K$ where η_K is the Kolmogorov length scale, the damping function can be assumed to be written in the form of $\{ 1.0 - \exp [-C (y / \eta_K)] \}^{4/3}$. Near the wall the $\{ 1.0 - \exp [-C (y / \eta_K)] \}^{4/3}$ is proportional to $(y / \eta_K)^{4/3}$, which led to obtaining Equation (2.36).

Combining Equations (2.35) and (2.36) results in a good correlation of the near wall length scale with the DNS data. However, at and near $y = C_D^{-3/4} \eta_K$, the length scale is still overpredicted. In order to prevent an excessive overestimation of the length scale in the region and to ensure a gradual transition from the inner to outer scales, the length scale, l , obtained Equations (2.35) and (2.36) is forced not to exceed the limit of $l = \kappa y$ in which κ is the von Karman constant. Therefore, the final form of the length scale, l , is written as

$$l = \min \left[C_L f_D \frac{k^{3/2}}{\varepsilon}, \kappa y \right] \quad (2.37)$$

A comparison with the Spalart's DNS data for $Re_\theta = 1410$ led to setting the closure coefficients of C_L and C_D equal to 0.148 and 0.02, respectively. Figure 2.4 compares the mixing lengths obtained from the DNS data and Equation (2.37).

The turbulent viscosity, μ_t , now can be obtained from Equation (2.20) with the velocity and length scales estimated by using Equations (2.34) and (2.37). The closure coefficients of the $v'l$ -II model are summarized in Table 2.3.

Table 2.3. The Closure Coefficients Employed in the $v'l$ -II Model

C_{v2}	C_{v3}	C_D	C_L	κ
0.738	0.0967	0.020	0.148	0.38

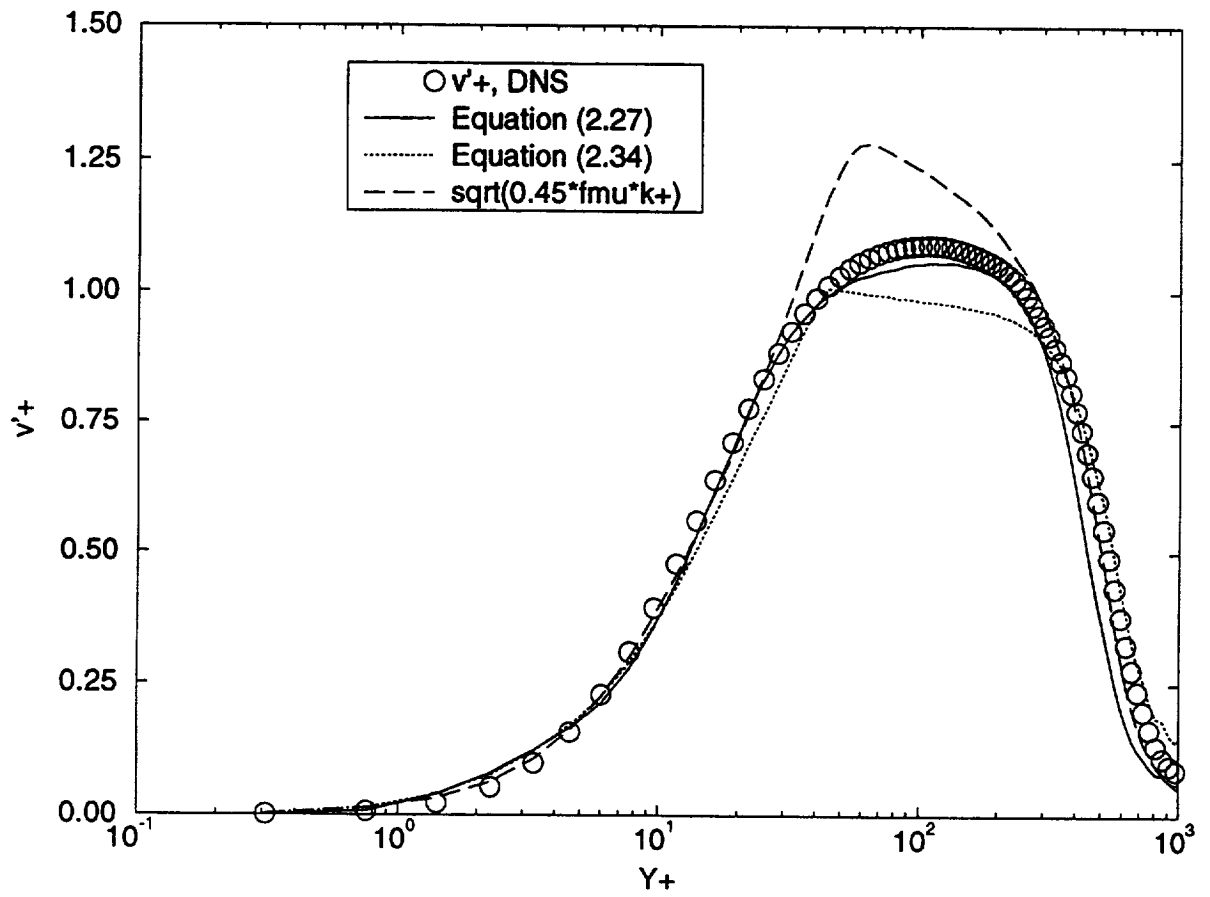


Figure 2.1 Comparison of DNS v'^+ with various models for a zero pressure gradient boundary layer at $Re_\theta = 1410$.

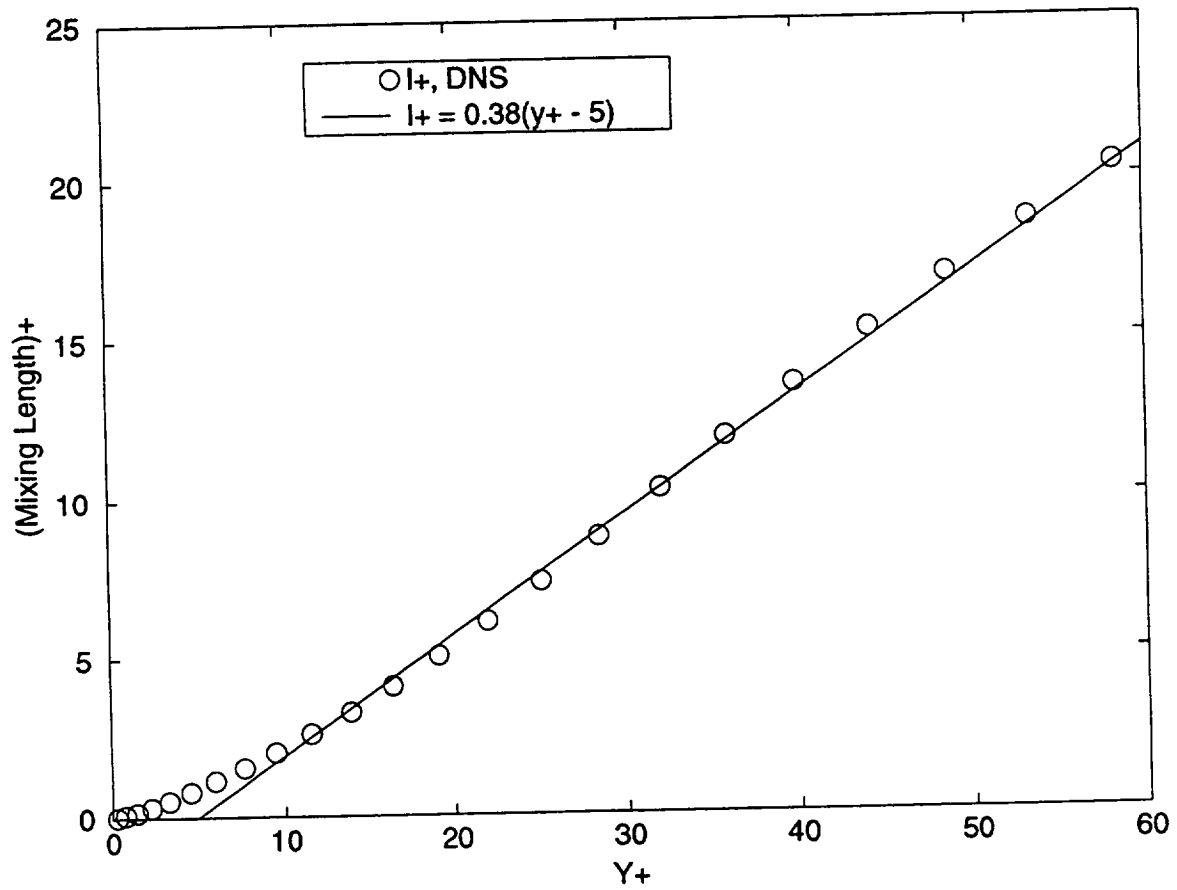


Figure 2.2 Comparison of DNS mixing length with linear model for a zero pressure gradient boundary layer at $Re_\theta = 1410$.

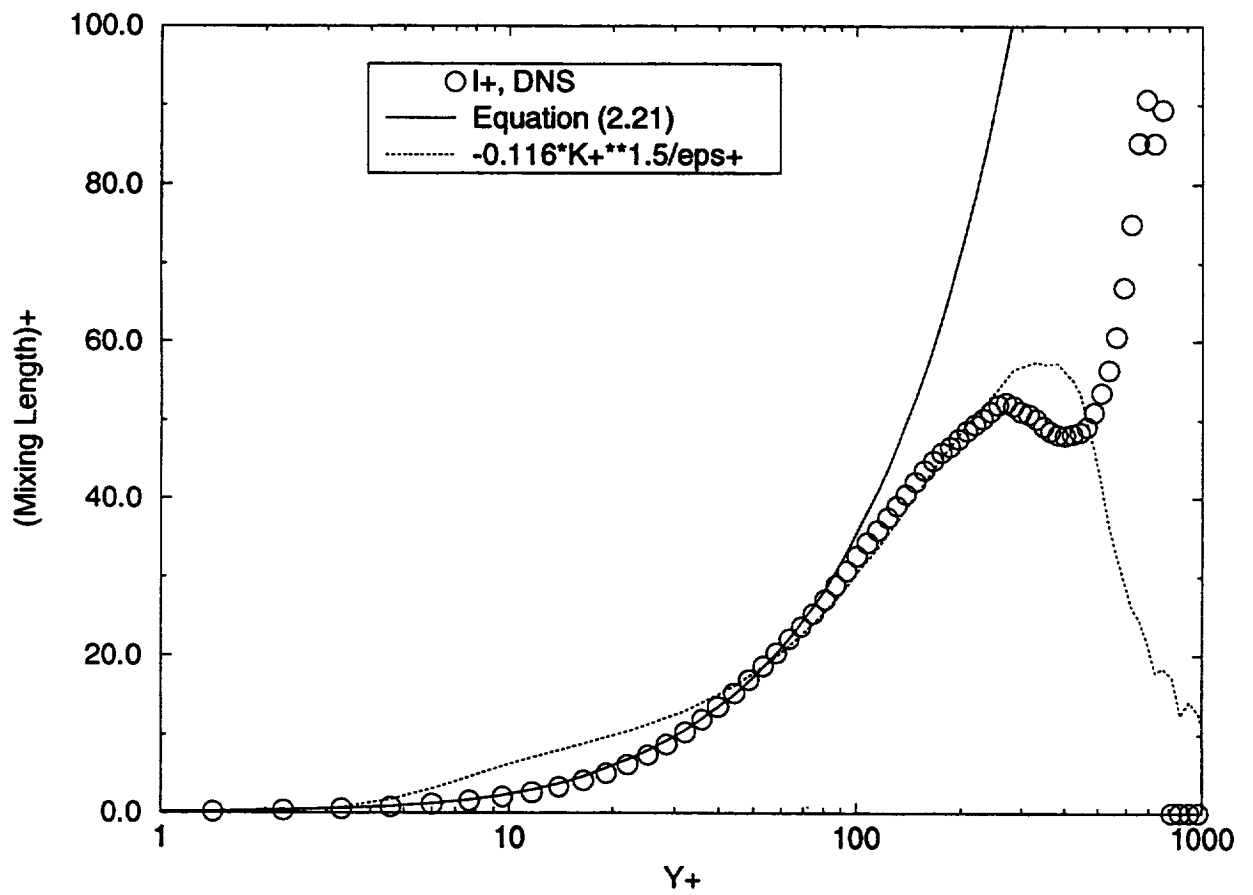


Figure 2.3 Comparison of DNS mixing length with $v'l$ -I model for a zero pressure gradient boundary layer at $Re_\theta = 1410$.

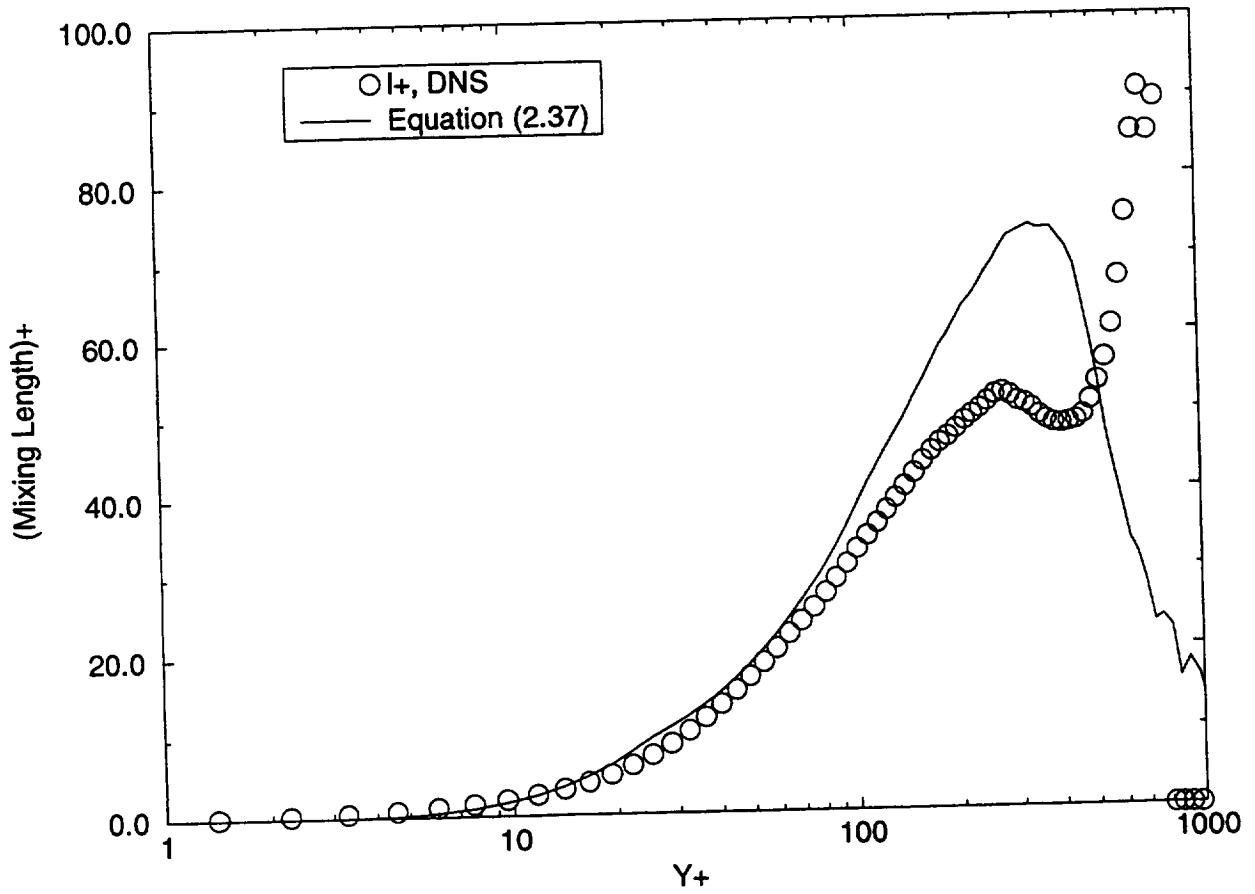


Figure 2.4 Comparison of DNS mixing length with $v'l$ -II model for a zero pressure gradient boundary layer at $Re_\theta = 1410$.

III. Computation Results and Discussions

The $v'l$ closure models were applied to analyzing various turbulent flows for model verification. For these analyses, the governing conservation equations for mass, momentum and energy, Equations (2.1), (2.6) and (2.7), were solved using an implicit finite difference scheme in an uncoupled manner. The turbulent kinetic energy and dissipation rate transport equations, Equations (2.12) and (2.13), were also solved using an implicit finite difference scheme, but in a coupled manner. For the turbulent transport equations, the convective terms were discretized by using a second order accurate scheme. A detailed solution procedure for a coupled system of equations can be found elsewhere [17]. All calculations were performed using double precision arithmetic on an IBM RS6000 work station.

1. Two-dimensional Fully Developed Turbulent Channel Flows

Two-dimensional fully developed channel flows were analyzed to test the proposed $v'l$ models. For these channel flows, there exist similarity solutions which are affected little by the initial conditions. The turbulence statistics are functions of the cross-stream coordinate only. Since recent direct numerical simulation (DNS) [23, 24] provided detailed flow information, these flows have often been used for developing and verifying turbulence models.

Since heat transfer was not analyzed, the governing continuity and momentum equations with turbulence models were solved. For the analyses, the boundary layer thickness δ used in the $v'l$ -I and $v'l$ -II models was replaced by the channel half width, h . In addition, for the $v'l$ -I model, the constant, κ , in the mixing length formulation was adjusted to 0.32, because the v' and l model equations developed based on the Spalart's DNS[16] for a turbulent flat plate boundary layer at $Re_\theta = 1410$ were found to provide too stiff eddy diffusivities near the wall for low Reynolds number channel flows.

The calculations were performed for $Re_\tau = 395$ and 180 where Re_τ is the Reynolds number based on the friction velocity, u_τ , and the channel half width, h . A total of 120 grid points were placed across the channel half width. The first grid point from the wall was located at $y^+ \approx 0.1$. At the channel center, the symmetry boundary condition was imposed for U , V , k and ϵ . Solutions were assumed to converge when the first five figures remained unchanged. Computed results were compared with DNS data.

(1) For $Re_\tau = 395$

The fully developed channel flow for $Re_\tau = 395$ was analyzed by using the proposed $v'l$ -I, $v'l$ -II, and base k - ϵ models along with the Durbin model[8] and the Yang-Shih model[7]. The models proposed by Durbin and Yang and Shih were chosen

since the base k- ϵ model originated from them. Furthermore, they provided a substantially better agreement of computed mean flow data and turbulent quantities with DNS data than other conventional k- ϵ models. The computed mean velocity profiles are compared with DNS data in Figure 3.1. The $v'l$ -I, $v'l$ -II, and base k- ϵ models provided good agreement with DNS data and the prediction of Durbin. Especially in the region where $y^+ = 10 - 30$, the $v'l$ -I and $v'l$ -II model predictions agreed better with the data than other predictions.

The computed turbulence kinetic energy profiles are presented in Figure 3.2 along with DNS data. The predictions from the $v'l$ -I, $v'l$ -II, and base k- ϵ models agreed very well with DNS data. The Durbin model and the Yang and Shih model gave over- and underpredictions, respectively, of the peak kinetic energy compared with the DNS data. For the dissipation rates shown in Figure 3.3, the $v'l$ -I model prediction agreed best with the DNS data. The base k- ϵ and Durbin relaxation models gave similar predictions. Their wall dissipation rates of $\epsilon_w^+ \approx 0.245$ were a little higher than the DNS. The $v'l$ -II model provided a reasonable wall dissipation rate ($\epsilon_w^+ \approx 0.20$), but it underpredicted in the near wall region where $y^+ < 10$. All of the computed dissipation rates formed an "S" shape in the near wall region with the overpredicted second peak at $y^+ \sim 10$ compared with the data. Among them, the overprediction of the second peak by the $v'l$ -I and $v'l$ -II models were least as shown in Figure 3.3. Such overpredictions might be caused by the large production term in the dissipation rate equation as discussed by Durbin[15].

Figure 3.4 presents computed turbulent shear stress profiles as well as DNS data. The $v'l$ -I, $v'l$ -II, and base k- ϵ models provided good comparison with DNS data as well as other predictions of the Durbin and Yang-Shih models. The normal component turbulent velocities computed using the proposed $v'l$ -I, $v'l$ -II, and base models as well as the Durbin model are shown in Figure 3.5 along with DNS data. For the base model, v' was computed from $v'^2 = 0.45f_\mu k$ with Equation (2.17). All four models provided good correlations with DNS data; although, in the outer region where $y^+ > 200$, the $v'l$ -I predicted a rapid decrease. Overall, the $v'l$ -II and Durbin models were better in the v' prediction than the $v'l$ -I and base k- ϵ models as compared with the DNS.

(2) For $Re_\tau = 180$

The fully developed channel flow at the lower Reynolds number of $Re_\tau = 180$ was analyzed by using the $v'l$ -I, $v'l$ -II, and base models. Figures 3.6 - 3.8 show the computed profiles of the mean velocity, turbulent kinetic energy, and dissipation rate, respectively, along with DNS data. The three models predicted the mean velocity as good as at the higher Reynolds number. For the turbulent kinetic energy, the $v'l$ -II model provided the best agreement with DNS data. The $v'l$ -I model underpredicted the peak kinetic energy, while the base k- ϵ models overpredicted slightly.

The dissipation rate profiles computed by using the three models agreed well with DNS data, although the base model prediction was slightly higher than the other two (see Figure 3.8). In the near wall region, the computed profiles formed an "S" shape as for the higher Reynolds number flow. The profiles had sharp peaks at the wall and fell off rapidly as moving away from the wall. The second peak occurred at $y^+ \sim 12.5$. The peak wall dissipation rates computed by using the $v'l$ -I, $v'l$ -II, and base models were $\epsilon_w^+ \equiv 0.17, 0.17, \text{ and } 0.21$, respectively. A detailed analysis of such near wall characteristics of the dissipation rate was provided by Durbin[15].

2. Flat Plate Turbulent Boundary Layers

The proposed $v'l$ -I, $v'l$ -II, and base models were tested for a flat plate turbulent boundary layer. The boundary layer form of the mass and momentum conservation equations, Equations (2.1) and (2.6), were solved with the proposed turbulence models. The upstream starting profiles were generated by using the turbulent profile generation procedure described in Appendix A. The computation was performed from near the leading edge of a flat plate until Re_θ became approximately 15,000. The assumed upstream freestream turbulence intensity was 1%. The grid in the normal direction was stretched at the rate of $\Delta y_{j+1}/\Delta y_j = 1.05$, where Δy and j denote the grid spacing and index, respectively. The first grid point from the wall was located at approximately $y^+ \sim 0.05$. The grid was also stretched in the streamwise direction at the rate of $\Delta x_i/\Delta x_{i-1} = 1.03$ but not exceeding 0.2δ , where δ is the boundary layer thickness. The first streamwise grid spacing was only a fraction of the boundary layer thickness ($\sim 0.001\delta$) in order to keep the influence of the initial profile on the flow solution within a short distance near the leading edge.

Figure 3.9 presents the computed skin friction coefficients using the $v'l$ -I, $v'l$ -II, and base models along with the data measured by Wieghardt and Tillmann[25] and Purtell, et al.[26]. All the computed data agreed well with the measured data. In detail, the $v'l$ -I model provided the highest value among the computations at low Reynolds numbers resulting in a better correlation with the data than the other two. Table 3.1 compares the computed friction coefficient, C_f , and shape parameter, H , with measured data and DNS data at two streamwise locations. The momentum thickness Reynolds number Re_θ at these locations were 670 and 1410, respectively. The DNS data were obtained by Spalart[16]. At both locations, the $v'l$ -I and $v'l$ -II models as well as the base model gave a fair to good agreement with the data. The agreement between the computed and measured data was in general better at the higher Re_θ . At $Re_\theta = 670$, the friction coefficient was underpredicted by all three models by approximately 2-7%. The $v'l$ -II model gave the lowest C_f . While, at $Re_\theta = 1410$, the base model provided the least agreement with an approximately 3.5% underprediction compared with the measured

data. The DNS prediction of C_f at $Re_\theta = 1410$ was higher than the measured data by approximately 4%. Overall, the $v'l$ -I model gave the best agreement at the lower Re_θ ; while, at the high Re_θ , the $v'l$ -II model provided the best comparison with the measured data.

Table 3.1. Flat Plate Turbulent Boundary Layer Integral Parameters

	$Re_\theta = 670$		$Re_\theta = 1410$	
	$C_f \times 10^3$	H	$C_f \times 10^3$	H
Wieghardt- Tillmann Data	4.96	–	3.98	–
Purtell, et al Data	4.91	1.53	3.99	1.46
DNS Data	4.86	1.50	4.14	1.43
Base k- ϵ Model	4.72	1.53	3.85	1.45
$v'l$ - I Model	4.86	1.56	4.05	1.47
$v'l$ - II Model	4.63	1.50	3.97	1.43

Figure 3.10 shows the predicted mean velocity profiles at $Re_\theta = 1410$ compared with the DNS data of Spalart[16] and the predictions of the Durbin and Yang-Shih models. The proposed $v'l$ -I, $v'l$ -II, and base k- ϵ models gave a good agreement with the DNS data, which is natural since the model coefficients were set based on the DNS data. Figure 3.11 presents a comparison of the computed and measured mean velocity profiles at two additional streamwise locations where $Re_\theta = 6,228$ and 14,703. The predictions of both $v'l$ -I and $v'l$ -II models agreed excellently with measured data of Wieghardt and Tillmann[25] as well as the Clauser curve which can be written as

$$U^+ = \frac{1}{\kappa} \ln y^+ + A \quad (3.1)$$

where the constants κ and A are set equal to 0.41 and 5.0, respectively. The base k- ϵ model slightly underpredicted velocities in the logarithmic law region at both locations. This comparison indicates that the $v'l$ -I and $v'l$ -II models represent adequately the Reynolds number effects. Between these two models, the $v'l$ -I model gave slightly

stiffer velocity profiles in the neighborhood of $y^+ \sim 20$ as shown in Figures 3.10 and 3.11.

In Figures 3.12 - 3.14, the predicted kinetic energy, dissipation rate, and shear stress profiles at $Re_\theta = 1410$, using the $v'l$ -I, $v'l$ -II, and base $k-\epsilon$ models are compared to DNS data [16]. The predictions from the Durbin model and Yang and Shih model are also shown in comparison. Overall, the proposed models gave a good agreement with the data. The most significant difference between the model predictions and the data was observed in the near wall dissipation rates as shown in Figure 3.13. The $v'l$ -I and base $k-\epsilon$ models provided good agreement with the DNS data in that region, while the $v'l$ -II model underpredicted. However, the second peak of the dissipation rate occurring at around y^+ equal to 10 is well predicted by all three models as compared with the DNS data.

The normal component of turbulent velocities at $Re_\theta = 1410$ computed using the $v'l$ -I and $v'l$ -II models were compared with the DNS data in Figure 3.15. In the near wall region where $y^+ < 40$, both models gave good agreement with the data; while, in the outer region, the predictions deviated from the data. The $v'l$ -I model predicted an early decrease beyond $y^+ > 200$, while the $v'l$ -II model underpredicted between $y^+ = 40 - 200$. The present analysis indicates that v' in the outer region affects little on the prediction of mean flow and turbulence quantities. As discussed by Durbin[15], the correct prediction of the near wall behavior of v'^2 seems to be a key to predicting data.

3. Turbulent Boundary Layers Developing with Favorable Pressure Gradient

Turbulent boundary layers with favorable pressure gradient measured by Herring and Norbury (flow 2700 and 2800 as identified in the 1968 AFOSR-IFP-Stanford Conference) [27, 28] were analyzed using the proposed $v'l$ -I, $v'l$ -II, and the base $k-\epsilon$ models as well as the models developed by Launder and Sharma[29] and Durbin[8]. In these flows, no similarity solution exists and the initial profile strongly affects strongly the downstream solutions. Therefore, the analysis required accurate initial profiles of the mean velocity and turbulence quantities.

For the present analysis, the initial profiles were generated in the following manner. First, to reduce the effect of inaccurate initial profiles on the downstream flow solutions, the computation domain was extended upstream arbitrarily by 0.61 m (2 ft). The upstream boundary layer thickness δ_{in} at $x = -0.61$ m was calculated by matching the calculated Re_θ at the first profile measurement location ($x = 0$ m) with the data. The measured Re_θ at $x = 0$ m was 3,393 and 4,107 for flow 2700 and 2800, respectively.

During this process, the boundary layer equations were solved repeatedly for the upstream extended region with δ_{in} which was assumed initially and updated iteratively later. The initial profiles of U , k , and ϵ at $x = -0.61$ m were computed by using the turbulent profile generation procedure described in Appendix A. The freestream velocity boundary conditions in this extended region were prescribed by extrapolating measured velocities in the test section. Figures 3.16 and 3.17 show the comparison of the computed and measured profiles at $x = 0$ m for flow 2700 and 2800, respectively. All of the turbulence models considered gave a reasonable agreement with the data.

The present calculations were performed up to $x = 1.524$ m and 1.22 m for flow 2700 and 2800, respectively. The grid in the normal direction was stretched at the rate of $\Delta y_{j+1}/\Delta y_j = 1.05$, where Δy and j denote the grid spacing and index, respectively. The first grid point from the wall was located at approximately $y^+ \sim 0.05$. The grid was also stretched in the streamwise direction at the rate of $\Delta x_i/\Delta x_{i-1} = 1.03$ but not exceeding 5% of the boundary layer thickness. The first streamwise grid spacing at $x = -0.61$ m was only a fraction of the local boundary layer thickness ($\sim 0.001\delta_{in}$). The freestream turbulence was assumed to be 1% upstream ($x = -0.61$ m).

(1) Mild Favorable Pressure Gradient Flow: Flow 2700

Flow 2700 was an equilibrium turbulent boundary layer developing in a mild favorable pressure gradient. Herring and Norbury[27] measured boundary layer parameters and velocity profiles at every 0.3048 m (1 ft) from $x = 0$ m to 1.524 m of the test section. In this region the measured freestream velocity increased continuously such that its streamwise gradient increased initially from $dU_e/dx = 2.65 \text{ sec}^{-1}$ at $x = 0$ m to $dU_e/dx \cong 6.25 \text{ sec}^{-1}$ at $x = 0.686$ m and remained approximately constant downstream. Likewise, the measured equilibrium parameter β , which is defined by $\beta = (\delta^*/\tau_w) dp/dx$, of the boundary layer also increased from -0.229 at $x = 0$ m in the front test section to approximately -0.35 near the mid section. In the downstream, β remained almost constant.

Figure 3.18 shows the computed friction coefficients using the proposed turbulence models as well as Durbin and Launder-Sharma models and measured data of Herring and Norbury[27]. The measured friction coefficients remained approximately constant at $C_f \sim 0.00345$ in the entire measurement section. The $v'l$ -I, $v'l$ -II, and base k - ϵ models provided a good agreement with the data, while the Durbin[8] and Launder and Sharma models [29] underpredicted the wall friction. The mean velocity profiles at the last measurement location of $x = 1.524$ m obtained with the proposed models also compared well with measured data as depicted in Figures 3.19 and 3.20. At this location, the Launder and Sharma model substantially overpredicted the nondimensional velocity, U^+ , in the logarithmic profile (see Figure 3.19), which was caused by the underpredicted C_f .

(2) Strong Favorable Pressure Gradient Flow: Flow 2800

Flow 2800 was a turbulent boundary layer developing in a strongly favorable pressure gradient. Herring and Norbury[28], who measured this flow, suspected that "the flow might possibly be on the verge of relaminarization." The measured freestream velocity increased rapidly throughout the test section which covered from $x = 0$ m to $x = 1.22$ m. The streamwise velocity gradient increased from $dU_e/dx = 5 \text{ sec}^{-1}$ at $x = 0$ m to 17 sec^{-1} at $x = 1.22$ m; and the measured β also varied continuously from -0.525 to -0.620 .

Figure 3.21 presents computed friction coefficients compared to measured data of Herring and Norbury. The measured data showed a monotonic increase of the friction coefficient in the streamwise direction from $C_f = 0.00327$ at $x = 0$ m to $C_f = 0.00375$ at $x = 1.219$ m. The proposed $v'l$ -I, $v'l$ -II, and base k - ϵ models as well as the Durbin model gave also an increase of C_f in the streamwise direction, but the increase rate was small compared to the measurements of Herring and Norbury[28]. The computed friction coefficients using the Launder and Sharma model, however, were almost constant at $C_f \sim 0.0031$. Figures 3.22 and 3.23 show the computed and measured mean velocities at $x = 1.219$ m. The proposed models gave a good agreement with the data. The computed and measured velocity profiles in the Cartesian coordinates generally agreed better than in the semilogarithmic scale coordinates.

4. Turbulent Boundary Layers Developing in Adverse Pressure Gradient

The validation of the proposed $v'l$ -I and $v'l$ -II models along with the base k - ϵ model were also performed for turbulent boundary layers developing in adverse pressure gradients. Four different flows were predicted by using these models. The first three flows were measured by Bradshaw [30, 31, 32] and identified as flow 2500, flow 2600, and flow 3300 in the 1968 AFOSR-IFP-Stanford conference. Among them, flow 2500 and flow 2600 were equilibrium turbulent boundary layers which were developing in 'mild' and 'moderate' adverse pressure gradients, respectively. The measured freestream velocity varied in a power-law as $U_e \propto x^\alpha$. The exponent α was -0.15 for flow 2500 and -0.255 for flow 2600. While, Flow 3300 was a turbulent boundary layer which was subjected to constant pressure initially but later to a sudden moderate adverse pressure gradient. The freestream velocity of this flow in the adverse pressure gradient region decreased also as $U_e \propto x^\alpha$ with $\alpha = -0.255$. Measured freestream velocities of these three flows are depicted in Figure 3.24 along with their approximations used in the calculations as the freestream boundary condition. Note that the kinks of these curves are not real but are induced by the piecewise linear plotting scheme. Upstream of the first

velocity measurement location, the approximations were arbitrarily extrapolated forward to $x = 0$ m.

The last flow considered in this section was the turbulent boundary layer with adverse pressure gradient measured by Samuel and Joubert[33]. The pressure gradient was increasingly adverse over most of the test section. In a small region far downstream near the last profile measurement location, it was decreasingly adverse. Measured freestream velocities and their approximation are shown in Figure 3.25. The approximated velocity distribution was generated by using measured data of the streamwise pressure gradient, dC_p/dx .

All of the computations were performed from $x = 0$ m with an initial boundary layer thickness. The computed Re_θ at the first profile measurement location was matched to the measured data within 0.1%. The grid in the normal direction was stretched at the rate of $\Delta y_{j+1}/\Delta y_j = 1.05$, where Δy and j denote the grid spacing and index, respectively. The first grid point from the wall was located at approximately $y^+ \sim 0.075$ in most of the analyses. The grid was also stretched in the streamwise direction at the rate of $\Delta x_i/\Delta x_{i-1} = 1.03$ but not exceeding 5% of the boundary layer thickness. The first streamwise grid spacing near $x = 0$ m was only a fraction of the local boundary layer thickness ($\sim 0.001\delta$). The upstream freestream turbulence was assumed to be 1%.

(1) Mild Adverse Pressure Gradient Flow: Flow 2500

Bradshaw[30] measured the equilibrium turbulent boundary layer in a mild adverse pressure gradient. The turbulent boundary layer grew relatively fast. The measured Reynolds number based on the momentum thickness increased from 10,061 at the first profile measurement location ($x = 0.610$ m) to 22,579 at the last location ($x = 2.134$ m). While the measured friction coefficient decreased from 0.0023 at $x = 0.610$ m to 0.00195 at $x = 2.134$ m. Table 3.2 shows measured and computed boundary layer parameters at these first and last profile measurement locations. At both locations, the computed Re_θ and shape parameter H using the $v'l$ -I, $v'l$ -II, and base k - ϵ models matched the data within 6%. For the friction coefficient, the $v'l$ -I and $v'l$ -II models provided good agreement with the measured data; but the base k - ϵ model overpredicted the data by approximately 8-12 %. Figure 3.26 shows that the proposed $v'l$ -I and $v'l$ -II models provided much better comparison of the wall friction with the data than other k - ϵ base models.

Computed mean velocity profiles at three different locations of $x = 0.610$ m, 1.220 m, and 2.134 m are compared with measured data in Figures 3.27 and 3.28. Both $v'l$ -I and $v'l$ -II models provided better correlation with the measured velocities than other models. In $10 < y^+ < 100$, all of the models except the Launder and Sharma model underpredicted the nondimensional velocity, U^+ , compared to the data. Figure 3.28

shows that the mean velocity profiles compared better in the Cartesian coordinates than in the previous semilogarithmic scale coordinates.

**Table 3.2. Boundary Layer Integral Parameters for Bradshaw
Equilibrium Boundary Layer developing in Mild Adverse
Pressure Gradient**

	X = 0.610 m			X = 2.134 m		
	Re_θ	$C_f \times 10^3$	H	Re_θ	$C_f \times 10^3$	H
Bradshaw Data	10,062	2.30	1.426	22,578	1.95	1.399
Launder-Sharma Model	10,058	2.47	1.386	21,504	2.23	1.341
Durbin Model	10,059	2.42	1.472	21,592	2.12	1.444
Base k- ϵ Model	10,062	2.49	1.464	21,740	2.19	1.429
$v'l$ - I Model	10,063	2.23	1.449	21,133	2.02	1.415
$v'l$ - II Model	10,061	2.30	1.420	21,196	2.04	1.387

(2) Moderate Adverse Pressure Gradient Flow: Flow 2600

As measured by Bradshaw[31], the freestream velocity of flow 2600 decreased much faster than that of the previous case (see Figure 3.24). The boundary layer thickness, therefore, grew faster than that of flow 2500 such that δ at $x = 2.108$ m was approximately 3.33 times that measured at $x = 0.584$ m; while in the previous mild pressure gradient it grew approximately 2.65 times in the same distance. Although the boundary layer thickened rapidly, measured friction coefficients decreased a little (approximately 7%) between the two locations, as shown in Figure 3.28.

The turbulent boundary layer was analyzed by using the $v'l$ -I, $v'l$ -II, and base k- ϵ models as well as the models developed by Launder and Sharma[29] and Durbin[8] with the approximated freestream velocities shown in Figure 3.24. Figure 3.29 shows that the proposed $v'l$ -I and $v'l$ -II models underpredicted the friction coefficient compared with

the data, while the base k- ϵ model and the Launder and Sharma model overpredicted. The prediction of the Durbin model[8] correlates best with the data.

Figure 3.30 presents the predicted and measured logarithmic velocity profiles at $x = 0.584$ m and 2.108 m. The $v'l$ -I and $v'l$ -II models gave significantly better correlations with the data than other k- ϵ models. Between $y^+ = 10$ and 100, both $v'l$ models underpredicted the non-dimensional velocity, U^+ . The mean velocity profiles were replotted in Cartesian coordinates in Figure 3.31. The $v'l$ -II model provided a good agreement with the data, while other models mostly underpredicted the mean velocities. Note that the Durbin relaxation model suffered from numerical instability when the first grid point from the wall was located closely such that y^+ at the first grid was equal to or less than approximately 0.1. A relatively coarse grid arrangement in the normal direction, therefore, was used for the Durbin model prediction for this flow.

(3) Flow Under the Sudden Application of an Adverse Pressure Gradient: Flow 3300

Flow 3300 was a turbulent boundary layer measured by Bradshaw [32]. The freestream pressure was initially constant in the front 0.610 m long test section. In the downstream, a sudden adverse pressure gradient was applied such that the freestream velocity decreased as $U_e \propto x^{-0.255}$. The measured boundary layer was developing into an equilibrium flow under the adverse pressure gradient.

The flow calculations were performed using the $v'l$ -I, $v'l$ -II, base k- ϵ , Durbin, and Launder and Sharma k- ϵ models with the velocity approximation shown in Figure 3.24 as the freestream boundary condition. The computed Reynolds numbers based on the momentum thickness at the first measurement location ($x = 0.610$ m) was matched to the measured data of $Re_\theta = 8,593$ within a 0.1% error. The calculated and measured boundary layer parameters at the first and last profile measurement locations are shown in Table 3.3. The friction coefficient comparison between predictions and measurements at the first profile location ($x = 0.610$ m) was fair to good. All of the computed friction coefficients except for that obtained from the base k- ϵ model agreed with the measured data within 2.5%. At the last profile measurement location ($x = 2.134$ m), the computed boundary layer parameters were generally deviated more from the data than at the first profile location. The $v'l$ -I model provided the best agreement in Re_θ , $H(=\delta^*/\theta)$, and C_f with the data at the location (see Table 3.3).

Figure 3.32 presents the comparison of computed and measured friction coefficients. The $v'l$ -I and $v'l$ -II models gave good comparison with the measured data. Other k- ϵ based models overpredicted significantly the wall friction in the entire adverse pressure gradient region. In Figures 3.33 and 3.34, the predicted mean velocities at three locations of $x = 0.610$ m, 1.219 m and 2.134 m are compared with measured data. Overall, the $v'l$ -I and $v'l$ -II models provided better agreement with the data at these

locations than other models. In Cartesian coordinates, the base model and the Durbin model also gave good comparison with the data (see Figure 3.34). Between the $v'l$ -I and $v'l$ -II models, the former gave slightly better predictions.

Table 3.3. Boundary Layer Integral Parameters for Bradshaw Turbulent Boundary Layer Subjected to a Sudden Mild Adverse Pressure Gradient

	X = 0.610 m			X = 2.134 m		
	Re_θ	$C_f \times 10^3$	H	Re_θ	$C_f \times 10^3$	H
Bradshaw Data	8,593	2.65	1.376	22,582	1.56	1.530
Launder-Sharma Model	8,589	2.68	1.295	23,102	2.08	1.430
Durbin Model	8,590	2.71	1.349	23,410	1.86	1.575
Base k- ϵ Model	8,593	2.81	1.337	23,496	1.93	1.551
$v'l$ - I Model	8,591	2.70	1.336	22,740	1.58	1.525
$v'l$ - II Model	8,592	2.70	1.323	22,693	1.66	1.481

(4) Samuel-Joubert Flow

The Samuel-Joubert flow[33] was the non-equilibrium turbulent boundary layer developed under an increasingly adverse pressure gradient and later under a brief decreasingly adverse pressure gradient near the end of the test section. The measured freestream velocity distribution was shown in Figure 3.25 along with the velocity approximation derived from the measured streamwise gradient of the pressure coefficient. The approximated velocity distribution was used in the calculations as the freestream boundary condition. Under the adverse pressure gradient, the boundary layer was developing into a non-equilibrium flow. Such a non-equilibrium flow is difficult to predict with conventional k- ϵ models and, therefore, has been often used as a test case for turbulence models.

The proposed $v'l$ -I, $v'l$ -II and base k - ϵ models were tested to verify their prediction capabilities for this non-equilibrium flow. For the comparison purpose, the flow was also analyzed by using the models developed by Launder and Sharma [29] and Durbin [8]. The calculation started with a zero pressure gradient boundary layer at $x = 0$ m. The computed momentum thickness Reynolds numbers at the first measurement location where $x_1 = 0.855$ m were matched iteratively to the measured data of $Re_\theta \equiv 4,830$ based on the inlet reference velocity. The measured Reynolds number based on the inlet reference velocity per unit length was approximately $1.7 \times 10^6 \text{ m}^{-1}$.

In Figure 3.35, the computed friction coefficients normalized based on the upstream reference velocity are compared with measured data. The friction coefficient, C_{f0} , at the first measurement location ($x - x_1 = 0$ m) was overpredicted by all of the models. Downstream, the $v'l$ -I and $v'l$ -II models as well as the Durbin models provided good comparisons with the data, although the $v'l$ models and the Durbin model gave slight underprediction and overprediction, respectively. The base k - ϵ model prediction also agreed well with the data except far downstream where the adverse pressure gradient was relatively strong. Meanwhile, the prediction of the Launder and Sharma model deviated gradually from the data as the pressure gradient built up. In Figure 3.36, calculated boundary layer shape parameters are depicted along with measured data. The shape parameters obtained from the $v'l$ -I, base and Durbin models correlated well with the data initially, but they gradually deviated from the data as the pressure gradient became stronger. Meanwhile, the $v'l$ -II model underpredicted the shape parameter except for the near exit region where the pressure gradient was relatively strong. The Launder and Sharma model gave a significant underprediction throughout the computation domain.

Figures 3.37 and 3.38 present the computed mean velocity profiles at $x - x_1 = 0.935$ m and 2.535 m, along with measured data. At $x - x_1 = 0.935$ m, the pressure gradient was relatively mild and increasingly adverse; while, at $x - x_1 = 2.535$ m, it was relatively strong and decreasingly adverse. At the first location, all predicted profiles compared well with the data. However, at the second location, the k - ϵ based models except the $v'l$ -I and $v'l$ -II models gave poor comparison with the data. The $v'l$ -I and $v'l$ -II models also reproduced qualitatively the evolution of turbulence quantities of the kinetic energy, shear stress, and variance of the normal component turbulence velocities as shown in Figures 3.39-3.42. In relatively strong adverse pressure gradient these two models failed to match measured data quantitatively: at $x - x_1 = 2.535$ m, the kinetic energy was underpredicted; while the shear stress and normal component turbulence velocity were overpredicted.

5. Turbulent Boundary Layer Heat Transfer

The proposed v'/l -I and v'/l -II models as well as the base k - ϵ model were evaluated for their heat transfer prediction capabilities. For a relatively clean flow with low freestream turbulence intensity ($Tu_\infty < 0.5\%$), these three models predicted surface heat transfer in good agreement with measured data as shown in Figure 3.43. The data shown in Figure 3.43 were measured by Ames and Moffat[21] for a zero pressure gradient boundary layer which developed on a uniformly heated flat plate with an upstream unheated length of 0.19 m. The measured upstream Reynolds numbers per unit length were approximately $1 \times 10^6 \text{ m}^{-1}$ and $2 \times 10^6 \text{ m}^{-1}$. The computed velocity and temperature profiles at $Re_\theta = 3,350$ and $Re_h = 3540$, respectively, using the v'/l -I and v'/l -II models correlated also very well with measured data of Ames and Moffat as shown in Figure 3.44. Here, Re_h denotes the Reynolds number based on the enthalpy thickness. The base k - ϵ model gave an underprediction of the logarithmic velocity profile in the logarithmic law region. For these calculations, the energy equation was solved with the measured heat flux wall boundary condition. The turbulent Prandtl number was obtained from the Kays' correlation[12] given in Equation (2.5).

The v'/l -I, v'/l -II, and base k - ϵ models were also assessed for predicting heat transfer from flat plate boundary layers with high intensity, large scale turbulence. Ames and Moffat[21] generated high intensity, large scale turbulence in a simulated combustor which produced turbulence level up to 19% with length scale ranging 11 ~ 14 cm. Such high intensity, large scale freestream turbulence can cause high anisotropies in the wall boundary layer. Ames and Moffat observed from their experiment that the normal component turbulence was strongly attenuated by the wall, which resulted in a significant reduction of the influence of freestream turbulence on boundary layer development. Such phenomena can't be predicted by conventional k - ϵ models since the models have no mechanism to deal with the anisotropic behavior of external turbulence.

Heat transfer analyses were performed for three turbulent boundary layers measured by Ames and Moffat[21] with their turbulence generator #5. The measured upstream Reynolds numbers per unit length of these flows were approximately $0.38 \times 10^6 \text{ m}^{-1}$, $0.75 \times 10^6 \text{ m}^{-1}$, and $1.4 \times 10^6 \text{ m}^{-1}$. The upstream turbulence was $Tu_\infty \approx 19\%$ and $Lu_\infty \approx 12 \text{ cm}$. At the end of the test section, the turbulence intensity level decreased to approximately 7%. The calculations started near the leading edge of the uniformly heated test plate with turbulent flow profiles generated by using the procedure described in Appendix A. The computed Re_θ at the first profiles measurement location ($x = 0.2032 \text{ m}$) was matched to the data iteratively. However, for other k - ϵ models such as the Launder and Sharma, Durbin, and Yang and Shih models which were used for comparison purposes, some difficulties were experienced in the trial-and-error matching of Re_θ . Such problems were caused by the prediction of unrealistically high mixing which resulted in a rapid boundary layer growth. For these models, an arbitrarily thin boundary layer thickness was specified upstream such that it provided the closest Re_θ at

the first measurement location compared to the data. The energy equation was solved with measured surface heat flux as the wall boundary condition. The turbulent Prandtl number was calculated from Equation (2.5).

In Figures 3.45-3.47, the computed wall Stanton numbers are compared with measured data for the Reynolds numbers per unit length of $0.38 \times 10^6 \text{ m}^{-1}$, $0.75 \times 10^6 \text{ m}^{-1}$, and $1.4 \times 10^6 \text{ m}^{-1}$, respectively. The agreement between the computed heat transfer using the $v'l$ -I and $v'l$ -II models and the data was excellent; while other models overpredicted significantly. The Durbin relaxation model which provided reasonable predictions for the non-equilibrium flow under increasingly adverse pressure gradient performed equally poorly as the conventional k - ϵ model. As the Reynolds number increased, the deviation of these predictions from the data became larger. Figure 3.48 shows calculated velocity and temperature profiles at the near exit plane ($x = 2.13 \text{ m}$) for these three flows using the $v'l$ -I and $v'l$ -II models. Both models gave good agreement with measured data.

The relatively good performance of the $v'l$ -I and $v'l$ -II models for non-equilibrium flows such as the Samuel-Joubert flow[33] and flat plate boundary layers with high intensity, large scale turbulence measured by Ames and Moffat[21] might be attributed to the formulation of the eddy diffusivity in terms of the velocity and length scales which were modeled based on the dissipation rate, the local coordinate and/or the characteristic time scales. With such formulations, the proposed $v'l$ -I and $v'l$ -II models were able to account for the anisotropy of the dissipation and the reduced length of mixing in the near wall region more adequately. Interestingly, the $v'l$ models have largely performed better in correlating the data than the more sophisticated Durbin relaxation model, in which two additional transport equations were employed for more accurate v'^2 evaluations. The second important factor was thought to be the use of the more adequate non-singular ϵ equation augmented with the local anisotropy term. This argument was based on the observation that the base k - ϵ model, which employed the conventional eddy viscosity formulation with a damping function, provided often comparable solutions to the Durbin relaxation model and significantly better than conventional k - ϵ models.

6. Turbine Airfoil Heat Transfer

An important objective of the present study is to providing a more reliable prediction of gas side heat transfer rates on a turbine airfoil. The flow field inside the turbine passage is generally three-dimensional although, in the mid-span region, the three dimensional effect becomes of secondary importance. In addition the flow is very complex due to high turbulence intensity, strong pressure gradient, laminar-turbulent transition, surface curvature, surface roughness, cooling air injections, etc. A two-dimensional analysis using the time-averaged governing equations with a closure model, however, is still a common practice among airfoil cooling designers.

Accurate airfoil heat transfer predictions require implementing the aforementioned various flow factors into the closure model, which is almost impracticable. Among the flow factors, laminar-turbulent transition and laminar heat transfer augmentation due to the presence of freestream turbulence are known to affect the accuracy of non-film cooled airfoil heat transfer predictions significantly. However, these factors can't be easily implemented because of their complex natures and lack of detailed information about them. Despite the recent significant developments in turbulence modeling, no two-equation model has been proved to be capable of predicting these phenomena correctly. Empirical correlations are often used among design engineers. The proposed $v'l$ -I and $v'l$ -II closure models, like other two-equation models, do not have the capability of predicting these phenomena accurately. Therefore, a set of empirical correlations were developed and accommodated into the analysis by means of the effective viscosity/Prandtl number concept suggested by Hylton, et al.[34]

Generalized forms of the effective viscosity/Prandtl number can be written as

$$\mu_{\text{eff}} = \mu + (\gamma_t \mu_t + \gamma_{\text{TU}} \mu_{\text{TU}}) \quad (3.2)$$

$$\text{Pr}_{\text{eff}} = \frac{\mu + (\gamma_t \mu_t + \gamma_{\text{TU}} \mu_{\text{TU}})}{\frac{\mu}{\text{Pr}} + \frac{(\gamma_t \mu_t + \gamma_{\text{TU}} \mu_{\text{TU}})}{\text{Pr}_t}} \quad (3.3)$$

where

$$\text{Pr}_t = \frac{(\gamma_t \mu_t + \gamma_{\text{TU}} \mu_{\text{TU}})}{(k_m / c_p)_t} \quad (3.4)$$

Here, μ denotes the viscosity; Pr , the Prandtl number; γ , the intermittency factor varying from 0 to 1; k_m , the thermal conductivity; and c_p , the specific heat. The subscript 'eff' indicates the effective quantity; and the subscripts 't' and 'TU' for evaluating under the turbulent and freestream turbulence conditions, respectively. Note that the term in parenthesis above replaces the single term representation of turbulent eddy viscosity, μ_t , in Equations (2.8) and (2.9). Use of the same variable, μ_t , in both Equations (2.8) and (3.2) is intentional. In simple approaches, which explicitly include the effects of freestream turbulence, modeling of the turbulent viscosity, μ_t , is not changed. The freestream turbulence is accounted for by introducing an additional term ' μ_{TU} ' referred as the 'turbulence' viscosity[34]. With this approach, Equations (3.2) and (3.3) are equivalent to Equations (2.8) and (2.9) only if γ_t is unity and γ_{TU} and or μ_{TU} equals zero.

The intermittency factor, γ_t , in Equations (3.2) - (3.4) was introduced to model the transition process from laminar to turbulent by following the suggestion of Emmons[35].

It has generally a functional form that varies from 0 for laminar flow to 1 for fully turbulent flow. Specification of the actual functional form is the result of transition origin, path, and length modeling. For turbine airfoil flow, the transition onset was reasonably well predicted by the Mayle criterion[36] when the freestream turbulence intensity was high such as $Tu \geq 3\%$ but its augmentation effect was not significant. The Mayle criterion correlates the critical momentum thickness Reynolds number in terms of the freestream turbulence intensity as,

$$Re_{\theta t} = 400 Tu^{-5/8} \quad (3.5)$$

where $Re_{\theta t}$ denotes the momentum thickness Reynolds number at the transition onset; and Tu , the freestream turbulence intensity in per cent. When the augmentation becomes significant or when the turbulence intensity is low such as $Tu < 3\%$, this criterion tends to predict early transition. For low turbulence intensities, measured transition data of the flat plate flow can be represented reasonably well by the Abu-Ghannam and Shaw correlation (refer to Figure 11 in the reference [36]). The correlation is given by

$$Re_{\theta t} = 163 + \exp [6.91 - Tu] \quad (3.6)$$

An adjustment, therefore, was necessary to the Mayle criterion in order to take account of these observations. The correlation used in this analysis is written as

$$Re_{\theta t} = 500 Tu^{-0.68} \quad (3.7)$$

As shown in Figure 3.49, Equation (3.7) agrees well with the Abu-Ghannam and Shaw correlation in low turbulence intensities ($Tu < 2\%$); while it approaches asymptotically to the Mayle correlation in high turbulence intensities.

The transition intermittency factor, γ_t , is often modeled by an exponential function of the Reynolds number based on either the momentum thickness or the streamwise distance. Numerous correlations are currently available in the open literature. They were mostly developed based on a curve fit of data measured under limited flow conditions. Therefore, no universally applicable correlation has been found yet. Since the present study is not focused on developing transition models, a serious investigation was avoided and a rather simple form of expression was sought. A brief review on measured airfoil heat transfer data available for mid to high Reynolds numbers led to the following correlation:

$$\gamma_t = 1.0 - \exp \left[- \frac{Re_{\theta} - Re_{\theta t}}{Re_{\theta t}} \right] \quad (3.8)$$

where Re_θ is the local momentum thickness Reynolds number; and Re_{θ_t} is the momentum thickness Reynolds number at the transition onset given by Equation (3.7).

Figure 3.50 shows an example prediction of the airfoil surface heat transfer using this correlation, Equation (3.8). The data shown in this figure were measured by Turner, et al.[37] from a C3X airfoil. The measured Reynolds number was approximately 2×10^6 at the turbine exit. The Mach numbers at the inlet and exit plane were 0.16 and 0.9, respectively. The upstream turbulence intensity was approximately 6.55%. The measured laminar-turbulent transition on both suction and pressure surface started at around 30% and 25%, respectively, of the surface distance measured from the leading edge stagnation point. The transition process continued up to approximately 60% on the suction surface and near the trailing edge on the pressure surface. The computed transition process with the ν/l -II model matched the data on both suction and pressure surfaces.

The laminar heat transfer augmentation due to the presence of freestream turbulence is most prominent on the airfoil stagnation point and diminishes gradually downstream along the surface as the flow transition takes place. The phenomenon is generally more persistent on the pressure surface than the suction surface as shown in Figures 3.50 and 3.51. Recent studies[10] indicate that the airfoil leading edge augmentation might be caused by the straining of the flow around the cylinder stagnation region. The straining of the freestream flow leads to amplifying the energy in the small eddies with an axis parallel to the flow along the surface. According to Ames[10], the turbulence produced within the boundary layer, due to the influence of the flow field turbulence, is most likely responsible for the enhanced mixing and the high level of heat transfer augmentation on the pressure surface.

From dimensional reasoning as for the turbulent viscosity formulation, the 'turbulence' viscosity induced by freestream turbulence can also be written in terms of the velocity and length scales as,

$$\mu_{TU} \sim (\text{velocity scale}) \cdot (\text{length scale}) \quad (3.9)$$

In early studies reviewed by Hylton, et al.[33], the freestream turbulence fluctuation of TuU_e and the mixing length, which was defined in the same means as in the mixing length hypothesis definition of turbulent viscosity, were often used for the velocity and length scales, respectively. However, the recent study of Ames[10] indicates that the energy scale, Lu , of the freestream turbulence is a logical length scale to use in correlating the effects of turbulence on heat transfer rather than the turbulent mixing length. The study also indicates that the freestream turbulent eddies, which are large compared to the distance from the wall, are blocked by the presence of the wall. This blocking action causes a strong attenuation of the normal component turbulence and the lateral scale of turbulence normal to the wall, which influences significantly the surface heat transfer. Hunt and Graham rapid distortion theory[18] as well as Thomas and Hancock measurements[20] showed that the normal variance, v'^2 , of turbulence attenuated as a function

of $(y/L_x)^{2/3}$ as the wall was approached and the lateral integral scale, Ly , varied with the distance to the wall. Based on these studies, the turbulence viscosity can be formulated as

$$\mu_{TU} = C_{TU} Tu U_e Lu \left(\frac{y}{Lu} \right)^{4/3} \quad (3.10)$$

where C_{TU} denotes a constant; Tu , the freestream turbulence intensity in decimal; U_e , the freestream velocity; Lu , the energy scale of the freestream turbulence; and y , the local normal coordinate. Equation (3.10) was first derived by Ames and Moffat[21]. The intermittency factor, γ_{TU} , for the freestream turbulence effect was specified by following the suggestion of Hylton, et al.[34] as

$$\gamma_{TU} = 1 - \gamma_t \quad (3.11)$$

where γ_t denotes the intermittency factor of the laminar-turbulent transition defined in Equation (3.8). Equation (3.11) forces the freestream turbulence effect on the skin friction and heat transfer to be diminished gradually as the flow transition takes place so that, in fully turbulent flows, the 'turbulence' viscosity is completely eliminated in determining the effective viscosity. Such a process agrees qualitatively with the aforementioned experimental observations that the augmentation mainly occurred in the laminar flow zone.

Figure 3.51 shows an example calculation of Equation (3.10). The data shown in this figure are the heat transfer augmentation in the near leading edge region of a C3X airfoil under three different freestream turbulence conditions. These data were measured by Ames[10] for the airfoil exit Reynolds number based on the airfoil chord of 0.8×10^6 and the inlet and exit Mach numbers of 0.08 and 0.27, respectively. The three measured upstream freestream turbulence conditions were $Tu = 1.1\%/Lu = 66.0$ mm, $Tu = 7.75\%/Lu = 13.6\%$, and $Tu = 8.3\%/Lu = 43.4$ mm. The data showed a significant augmentation in heat transfer as the turbulence level increased from 1% to 8%. On the suction side of the airfoil, the augmentation diminished faster than on the pressure side. The data also showed that the smaller length scale provided higher augmentation than the larger one. The computed results reproduced all of these phenomena excellently. The calculations were performed with the modeling constant of $C_{TU} = 0.6$, which was used throughout the rest of the airfoil heat transfer calculations. The $v'l$ -I turbulence closure was used for these calculations. Figure 3.50 also presents an excellent correlation of computed heat transfer with measured data on an entire surface of a C3X airfoil measured by Turner, et al[37]. The measured Reynolds number of this case was much higher than the previous one shown in Figure 3.51.

Three different airfoil heat transfer data sets were analyzed using the proposed $v'l$ -I and $v'l$ -II models coupled with these additional features of laminar-turbulent transition and the laminar heat transfer augmentation induced by the freestream turbulence. They included the C3X airfoil heat transfer data measured by Ames[10] and

Turner, et al.[37], and the airfoil data measured by Arts, et al.[38]. Ames[10] measured airfoil surface heat transfer on a heated C3X airfoil with a constant heat flux; Turner, et al.[37] on internally cooled vane cascades by an array of radial cooling holes; and Arts, et al.[38] on uncooled airfoils placed in a compression tube tunnel. For both Turner, et al. and Arts, et al. measurements, the freestream was heated by a burner and an isentropic compression piston, respectively. The first data measured by Ames was for a relatively low Mach number ($M_1 = 0.08$ and $M_2 = 0.27$) flow; while the other two for high Mach number flows such as $M_2 = 0.78 - 1.06$. The Reynolds numbers at the airfoil exit plane of these flows ranged from 0.5×10^6 to 2.5×10^6 . The upstream turbulence intensity varied from 1% to 12%. The reason behind selecting these flows for evaluating the proposed $v'l$ models as well as the transition and augmentation correlations was that these data sets provided detailed turbulence information so that the turbulence levels and scales were easily estimated. Most of the early airfoil heat transfer data sets documented the turbulence data insufficiently.

The predictions were made by using the two dimensional steady compressible boundary layer equations, Equations (2.1), (2.6) and (2.7). The freestream velocities were obtained from a stream function analysis for the low Mach number C3X airfoil measured by Ames[10] and a two-dimensional Euler analysis for the high Mach number flow measured by Turner, et al.[37] and Arts, et al.[38]. The computed velocities for these airfoils are given in Appendix B. For the energy equation solution, either measured airfoil surface temperature or heat flux was specified on the surface; as was the measured total enthalpy or total temperature in the freestream. The starting profiles were obtained from the similarity solutions of the stagnation point developed by Kwon, et al.[13].

(1) C3X Airfoil Heat Transfer Measured by Ames

Ames[10] measured the surface heat transfer on a C3X airfoil, of which the profile is shown in Figure 3.52. The freestream turbulence level varied from $Tu = 1\%$ to 13% for two different flow conditions of $Re_{C2} = 0.5 \times 10^6$, $M_1 = 0.05$, $M_2 = 0.17$; and $Re_{C2} = 0.8 \times 10^6$, $M_1 = 0.08$, $M_2 = 0.27$. The present predictions were performed for the flow condition of $Re_{C2} = 0.8 \times 10^6$, $M_1 = 0.08$, $M_2 = 0.27$ with the freestream turbulence intensity ranging from 1% to 12% and the energy scale from 1.4 cm to 6.6 cm. The upstream total condition and turbulence data of the computed flows are shown in Table 3.4. The surface pressures obtained from a stream function analysis were compared with measured data in Figure 3.53. Both computed and measured surface pressure showed a strong adverse pressure gradient about 5 cm downstream of the stagnation point on the suction surface of the airfoil. The adverse pressure gradient at the location was so strong that the computed flow at $Tu = 1\%$ separated as shown in Figures 3.54 and 3.55. The airfoil surface heat transfer was calculated for the measured surface heat flux.

Figures 3.54 and 3.55 show the computed surface heat transfer for $Tu = 1\%$, 8% , and 12% by using the $v'l$ -I and $v'l$ -II models, respectively, along with measured data. The measured data indicated that a 'more-or-less' instantaneous transition took place on the suction surface for all three turbulence conditions considered. The sudden transition might have been triggered by the strong adverse pressure gradient that occurred in the

region. At the 1% freestream turbulence, both models predicted a laminar separation on the suction surface as described above. With the high freestream turbulence levels, both models, coupled with the transition and augmentation correlations, Equations (3.7), (3.8), (3.10) and (3.11), predicted gradual transitions on the suction surface and, therefore, they underpredicted the heat transfer level in the mid-chord region of the suction surface. An instantaneous transition approximation provided better agreement in the region for these cases.

On the pressure surface, the computed results showed a suppressed laminar-turbulent transition at high freestream turbulence levels. The v'/l -I model predicted faster development of flow transition than the v'/l -II on the surface. As shown in Figure 3.51, the turbulence scale effect on the augmentation was also well captured by the augmentation model, as previously discussed. Both computed and measured heat transfer coefficients for the smaller length scale were higher than for the larger scale.

Table 3.4. Upstream Flow Conditions for C3X Cascade Heat Transfer Measurements of Ames

Test Case	HTB100	HTG100	HTCS100	HTG200
Total Pressure (K Pa)	95.745	94.263	95.220	95.373
Total Temp. (°K)	300.44	300.22	298.72	297.84
Tu_{∞} (%)	1.1	7.75	8.3	12.0
Lu_{∞} (cm)	6.60	1.36	4.34	3.36

(2) C3X Airfoil Heat Transfer Measured by Turner, et al.

Turner, et al.[37] measured the surface heat transfer on a C3X airfoil with and without the leading edge blowing at various flow conditions. Among them, the calculations were performed for the non-blown condition at three different exit Reynolds numbers of $Re_{C2} = 1.5 \times 10^6$, 2.0×10^6 , and 2.5×10^6 . The Mach numbers and the upstream turbulence condition of all three cases were the same such that $M_1 = 0.16$, $M_2 = 0.9$, $Tu = 6.6\%$ and $Lu = 4.22$ cm. The upstream total condition and turbulence data of

the computed flows are shown in Table 3.5. The airfoil profile and surface velocities obtained from an Euler analysis are shown in Figures 3.56 and 3.57, respectively. The airfoil surface heat transfer was calculated for the measured surface temperature.

During this analysis, the wall boundary condition of the energy equation was found to affect rather significantly the accuracy of the surface heat transfer prediction. As commonly practiced among design engineers, specifying a uniform wall temperature resulted in a poor correlation with measured data in the region where the streamwise surface temperature gradient was relatively significant. Figure 3.58 shows a comparison of the calculated surface heat transfer coefficients using measured surface temperatures and a uniform surface temperature of $T_w/T_o = 0.764$. The measured surface temperature provided a good correlation with the data; while the uniform surface temperature underpredicted significantly near the leading edge region.

Table 3.5. Upstream Flow Conditions for C3X Cascade Heat Transfer Measurements of Turner, et al.

Test Case	4300	4400	4500
Total Pressure (K Pa)	208.65	273.44	345.67
Total Temp. (°K)	692.0	687.0	692.0
Tu_{∞} (%)	6.55	6.55	6.55
Lu_{∞} (cm)	4.22	4.22	4.22

Figure 3.59 shows the calculated airfoil surface heat transfer for three exit Reynolds numbers along with measured data of Turner, et al.[37]. The computed heat transfer coefficients using both $v'l$ -I and $v'l$ -II models agreed with measured data, although a little overprediction was found in the transition completion region of the suction surface at the highest Reynolds number of $Re_{C2} = 2.5 \times 10^6$. The flow transition on the suction surface took place between 30-60% of the surface arc length; and, on the pressure surface, it covered almost the entire surface for all three conditions. Between the $v'l$ -I and $v'l$ -II models, the former provided a little delayed transition on the suction surface while, on the pressure surface, the reverse was true.

In the leading edge region where $-10\% < x/s < 25\%$, the heat transfer augmentation of these three flows was significant as compared with the data shown in Figure 3.50. The data presented in Figure 3.50 are the calculated surface heat transfer for $Re_{C2} = 2.0 \times 10^6$ with and without including the augmentation effect and measured data. In the fully turbulent region where $x/s > 60\%$ on the suction surface and $x/s < -75\%$ on the pressure surface, the augmentation model provided no effect on the calculated heat transfer, which resulted in good agreement with measurements. The large difference between the two predictions in $-50\% < x/s < -10\%$ on the pressure surface (see Figure 3.50) was largely caused by the delayed flow transition prediction by the analysis without the augmentation.

(3) VKI Airfoil Heat Transfer Measured by Arts, et al.

Arts, et al.[38] measured airfoil surface heat transfer for a highly loaded transonic turbine vane at the von Karman Institute. The airfoil profile is shown in Figure 3.60 and Euler predictions of the surface velocity distribution for transonic and supersonic exit conditions are shown in Figures 3.61 and 3.62. The surface velocity distribution showed a continuous acceleration on both suction and pressure surfaces except for the near trailing edge region of the suction surface where a moderate-to-strong deceleration occurred. For this turbine airfoil, the effects of varying Reynolds number, turbulence level, and exit Mach number on the heat transfer were investigated.

The calculations were performed for the freestream turbulence level of 1%, 4%, and 6%; the exit Mach numbers of $M_2 = 0.8, 0.9$, and 1.06 ; and the exit Reynolds numbers of $Re_{C2} = 0.5 \times 10^6, 1.0 \times 10^6$, and 2.0×10^6 . Since the turbulence length scales were not documented in [38], they were estimated based on the description of the test facility set up as $Lu = 0.508$ cm, 1.397 cm, and 1.194 cm for $Tu = 1\%, 4\%$, and 6% , respectively. Table 3.6 shows the upstream total condition and turbulence data of the computed flows.

The surface heat transfer was calculated for a uniform wall temperature condition since no airfoil surface temperature distribution was documented in [38]. The effect of varying turbulence levels at three different exit Reynolds numbers is presented in Figures 3.63 - 3.65. The predictions for both surfaces agreed reasonably well with the data, except in the flow transition zone on the suction surface. For the low turbulence level ($Tu = 1\%$), both $v'l$ -I and $v'l$ -II models predicted a flow separation near the trailing edge of the suction surface where a moderate-to-strong adverse pressure gradient occurred. The measured data showed that, when the flow transition initiated upstream or inside the adverse pressure gradient region on the suction surface, a rapid transition took place as might have been triggered by the adverse pressure gradient. The computed results, however, showed rather a gradual transition. On the pressure surface, both models reproduced the measured data qualitatively. They tend to predict fast development of the transition for high Reynolds numbers and high freestream turbulence levels.

The heat transfer augmentation induced by the freestream turbulence was well predicted by both models. The underprediction in the leading edge region might have been caused by the use of the uniform wall temperature condition for the heat transfer analysis. It is noted that the surface temperature in the turbine airfoil leading edge region varies often significantly in the streamwise direction. The effect of varying exit Mach number is shown in Figure 3.66. The predictions of both $v'l$ -I and $v'l$ -II models agreed well with the data except in the downstream section of the pressure surface. In the region, the prediction showed a rapid development of the transition process while the data indicated a strongly suppressed transition. The calculated transition process on the suction surface compared well with the data.

Table 3.6. Upstream Flow Conditions for VKI Cascade Heat Transfer Measurements of Arts, et al.

Test Case	Total Pressure (K Pa)	Total Temp. (°K)	Tu_{∞} (%)	Lu_{∞} (cm)
MUR129	184.9	409.20	1.0	0.508
MUR217	183.5	412.70	4.0	1.397
MUR224	90.9	402.60	6.0	1.194
MUR226	90.4	404.10	4.0	1.397
MUR228	91.5	403.30	1.0	0.508
MUR232	167.3	413.20	6.0	1.194
MUR235	182.8	413.30	6.0	1.194
MUR237	175.3	417.30	6.0	1.194
MUR239	338.7	411.90	6.0	1.194
MUR245	338.4	412.60	4.0	1.397
MUR247	339.5	416.20	1.0	0.508

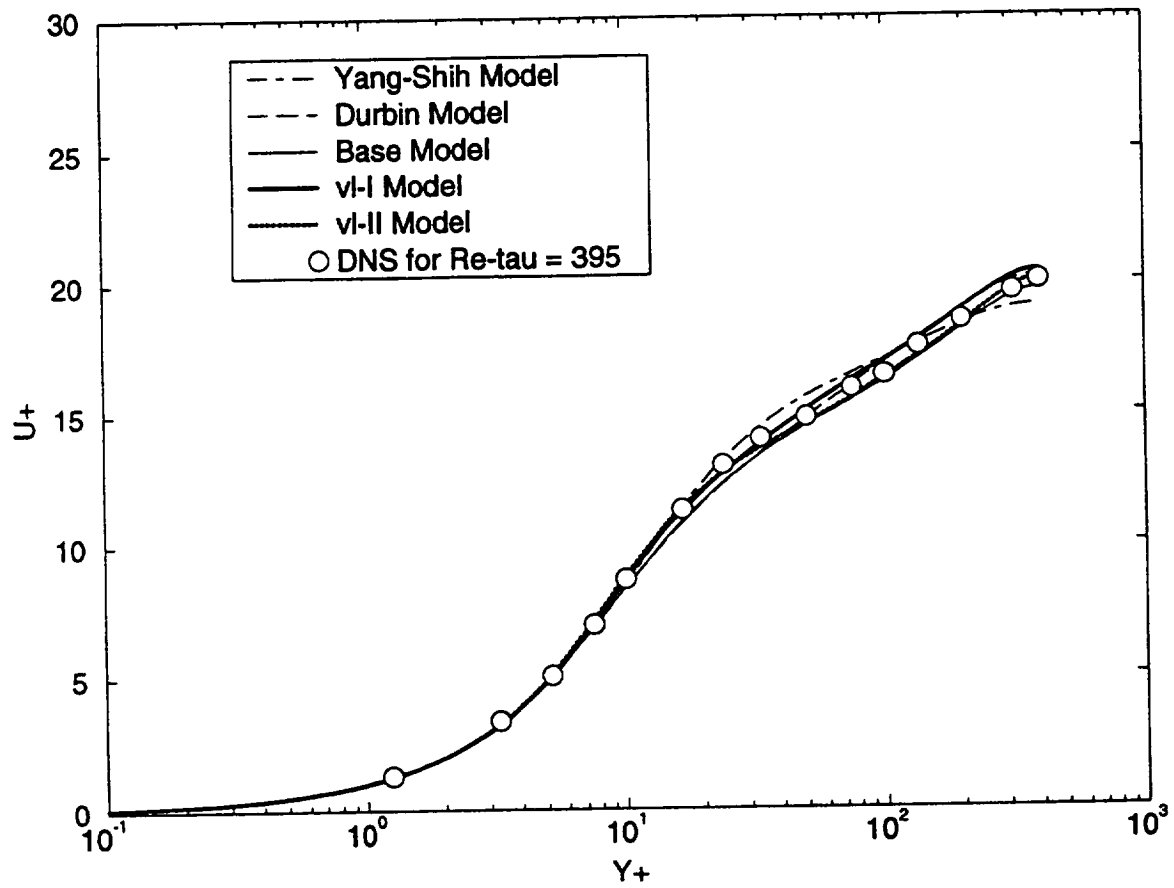


Figure 3.1 Comparison of mean velocity profiles predicted by using various k - ϵ based turbulence models with DNS data for a two-dimensional fully developed turbulent channel flow at $Re_\tau = 395$.

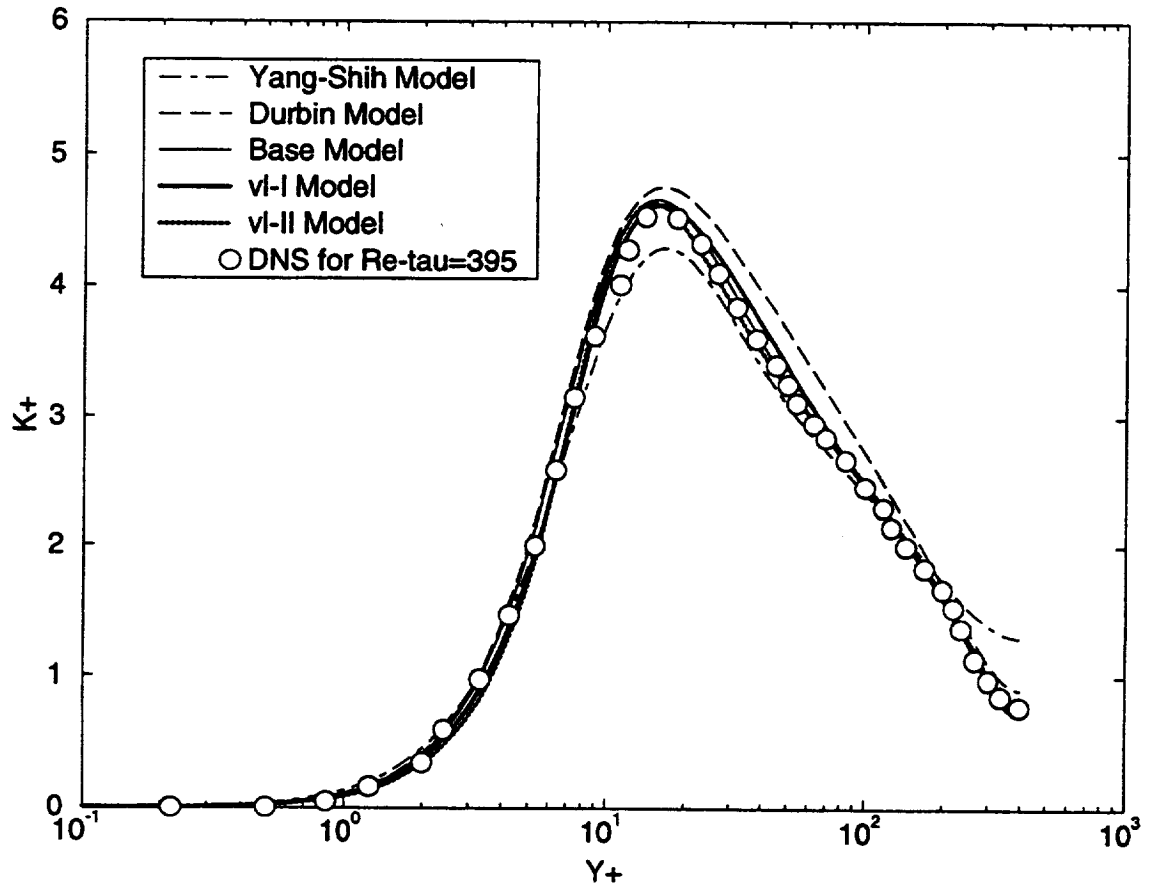


Figure 3.2 Comparison of turbulent kinetic energy profiles predicted by using various $k\text{-}\epsilon$ based turbulence models with DNS data for a two- dimensional fully developed turbulent channel flow at $Re_\tau = 395$.

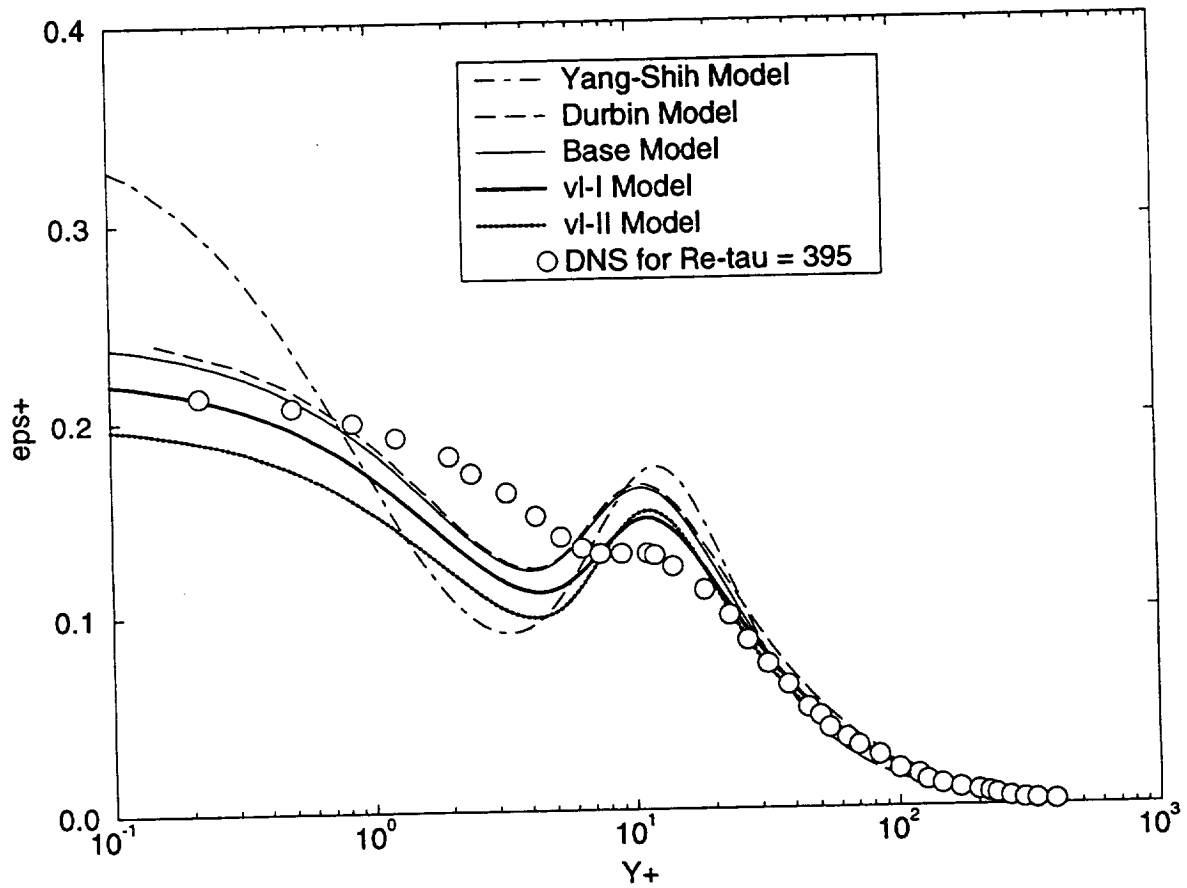


Figure 3.3 Comparison of dissipation rate profiles predicted by using various $k-\epsilon$ based turbulence models with DNS data for a two-dimensional fully developed turbulent channel flow at $Re_{\tau} = 395$.

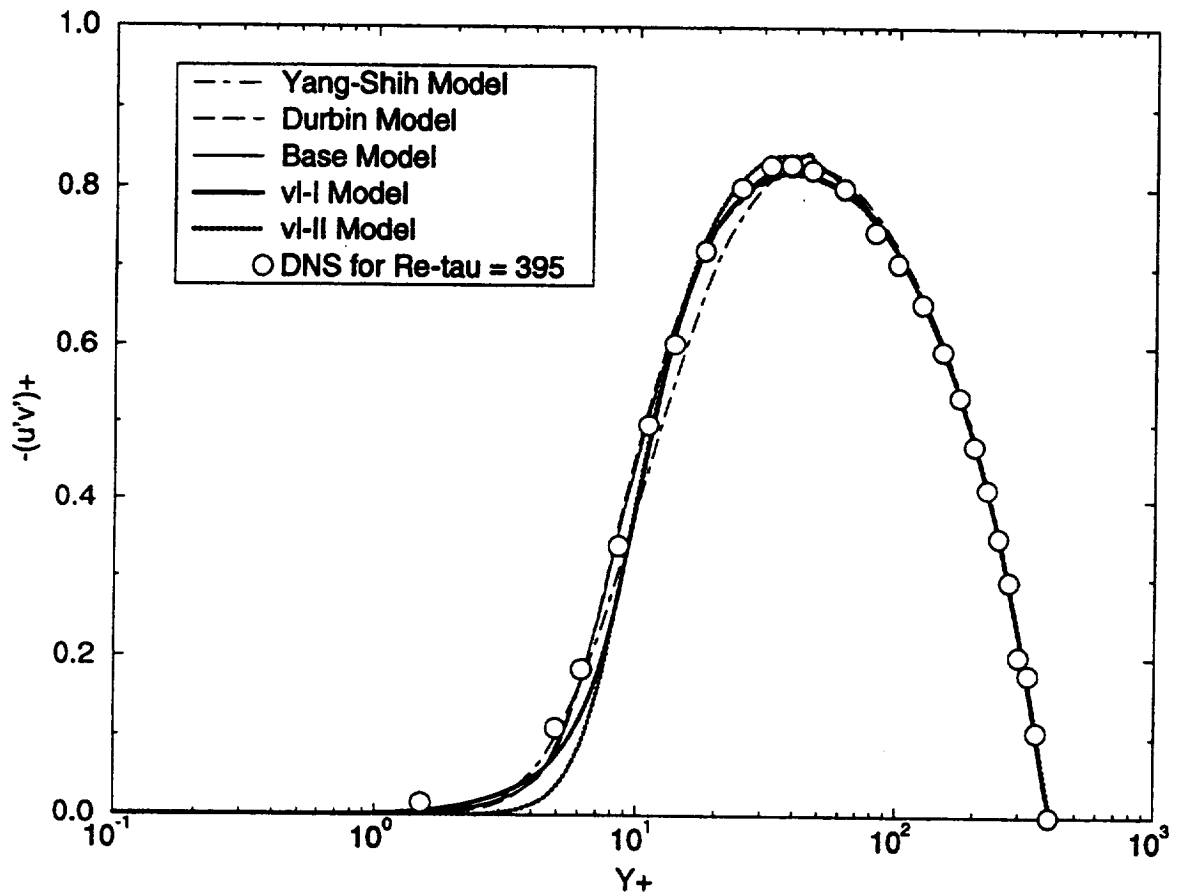


Figure 3.4 Comparison of turbulent shear stress profiles predicted by using various $k\text{-}\epsilon$ based turbulence models with DNS data for a two-dimensional fully developed turbulent channel flow at $Re_\tau = 395$.

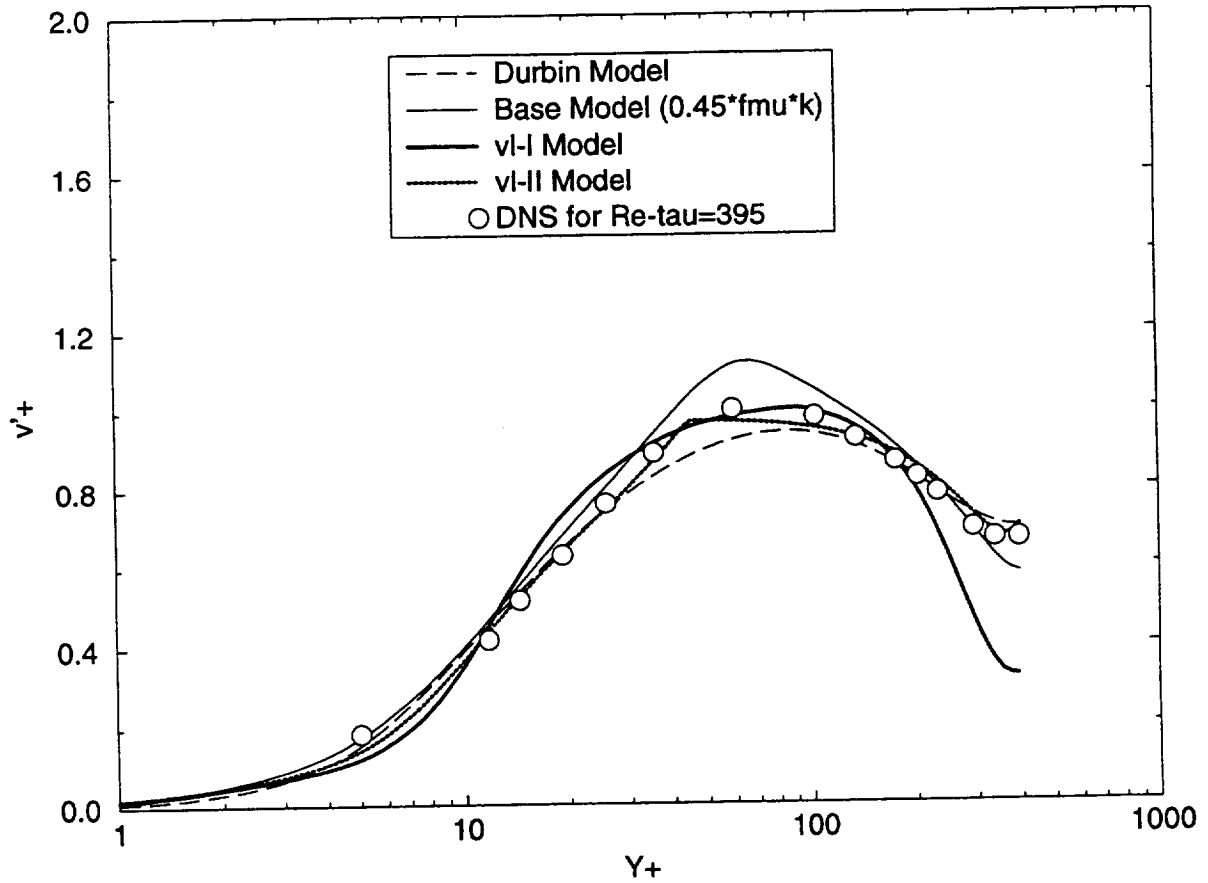


Figure 3.5 Comparison of normal component velocity profiles predicted by using various k - ϵ based turbulence models with DNS data for a two-dimensional fully developed turbulent channel flow at $Re_{\tau} = 395$.

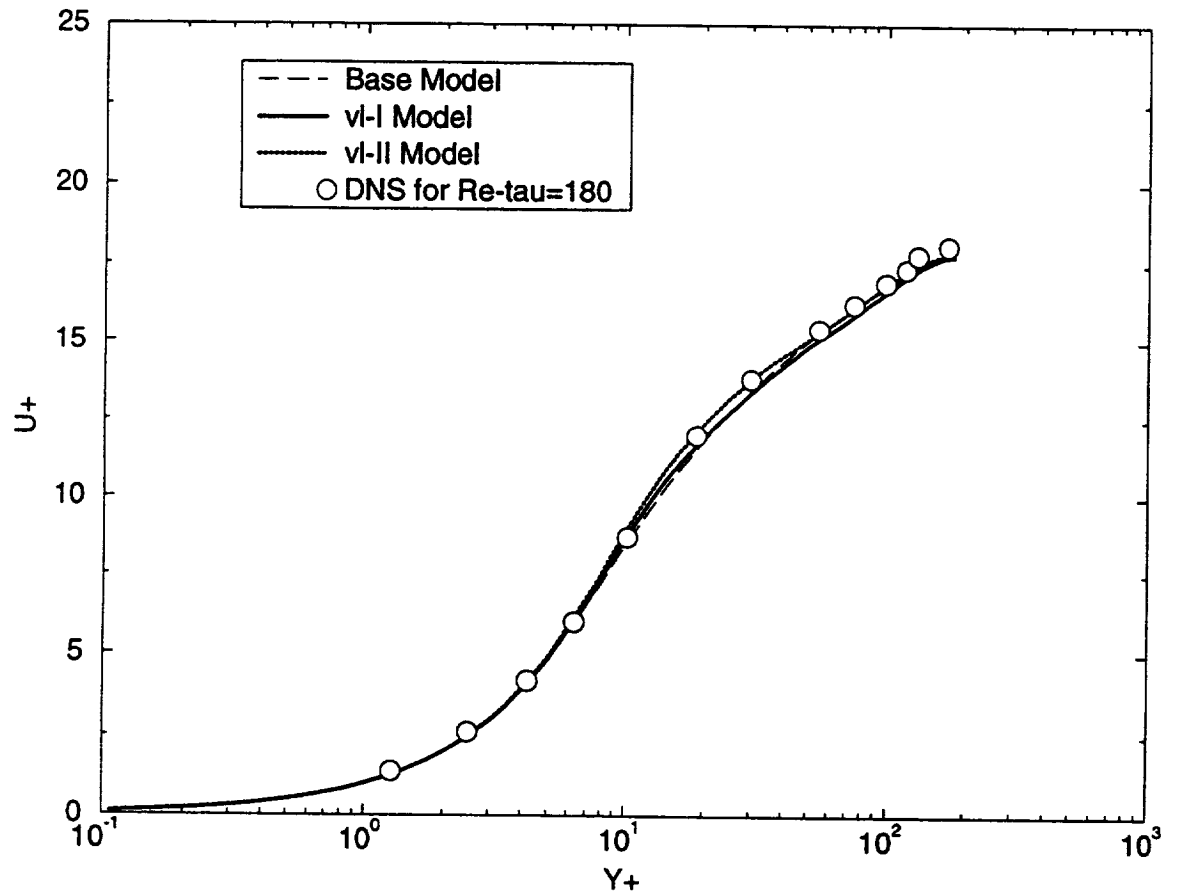


Figure 3.6 Comparison of mean velocity profiles predicted by using the $v'l$ -I, $v'l$ -II, and base k - ϵ turbulence models with DNS data for a two-dimensional fully developed turbulent channel flow at $Re_\tau = 180$.

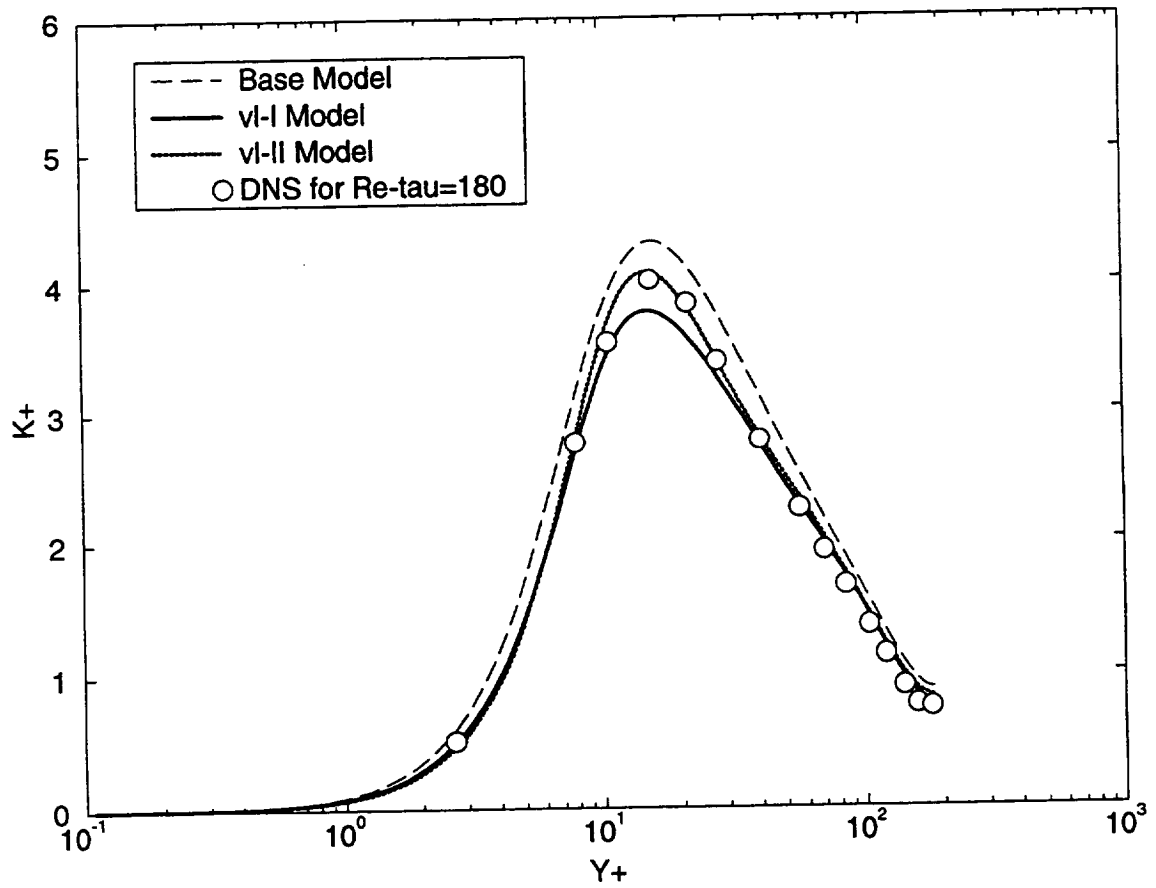


Figure 3.7 Comparison of turbulent kinetic energy profiles predicted by using the $v'l$ -I, $v'l$ -II, and base k - ϵ turbulence models with DNS data for a two-dimensional fully developed turbulent channel flow at $Re_\tau = 180$.

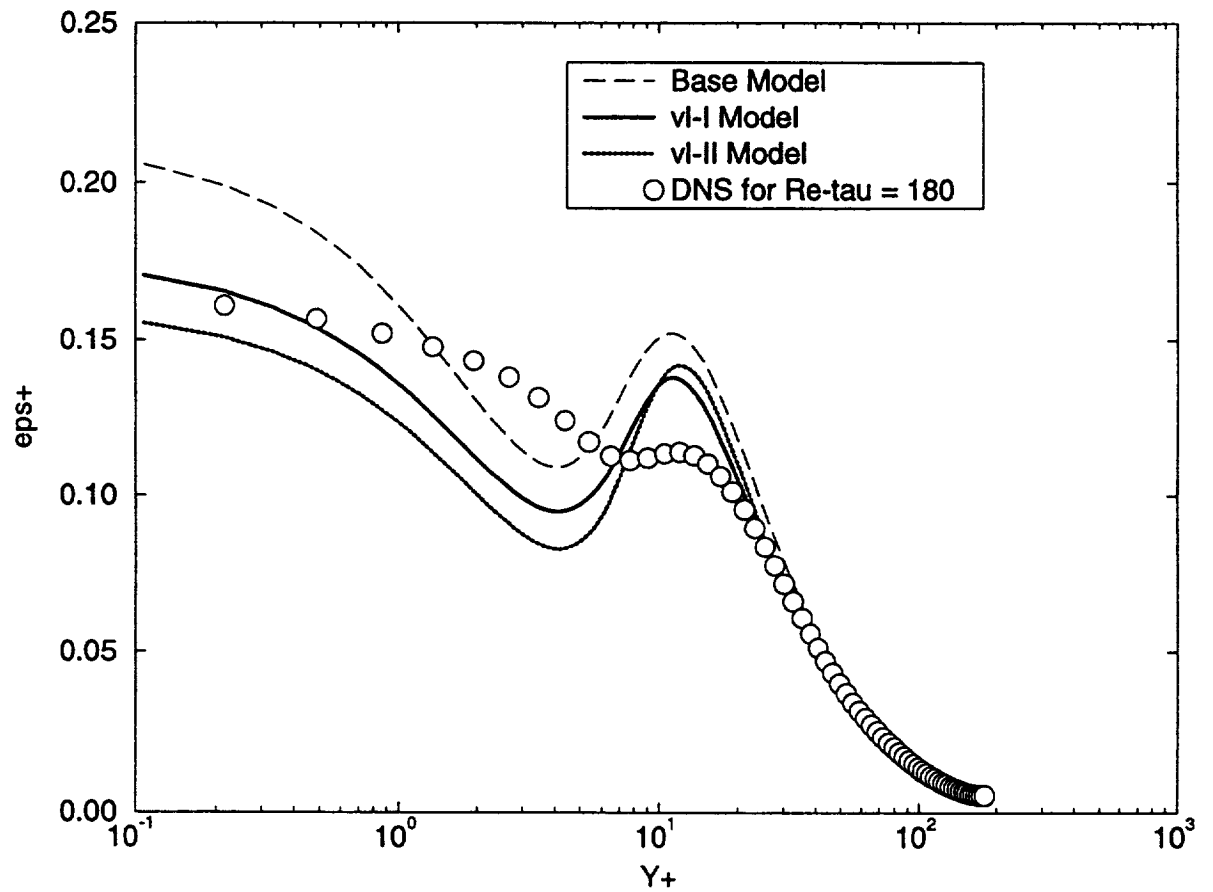


Figure 3.8 Comparison of dissipation rate profiles predicted by using the $v'l$ -I, $v'l$ -II, and base k - ϵ turbulence models with DNS data for a two-dimensional fully developed turbulent channel flow at $Re_\tau = 180$.

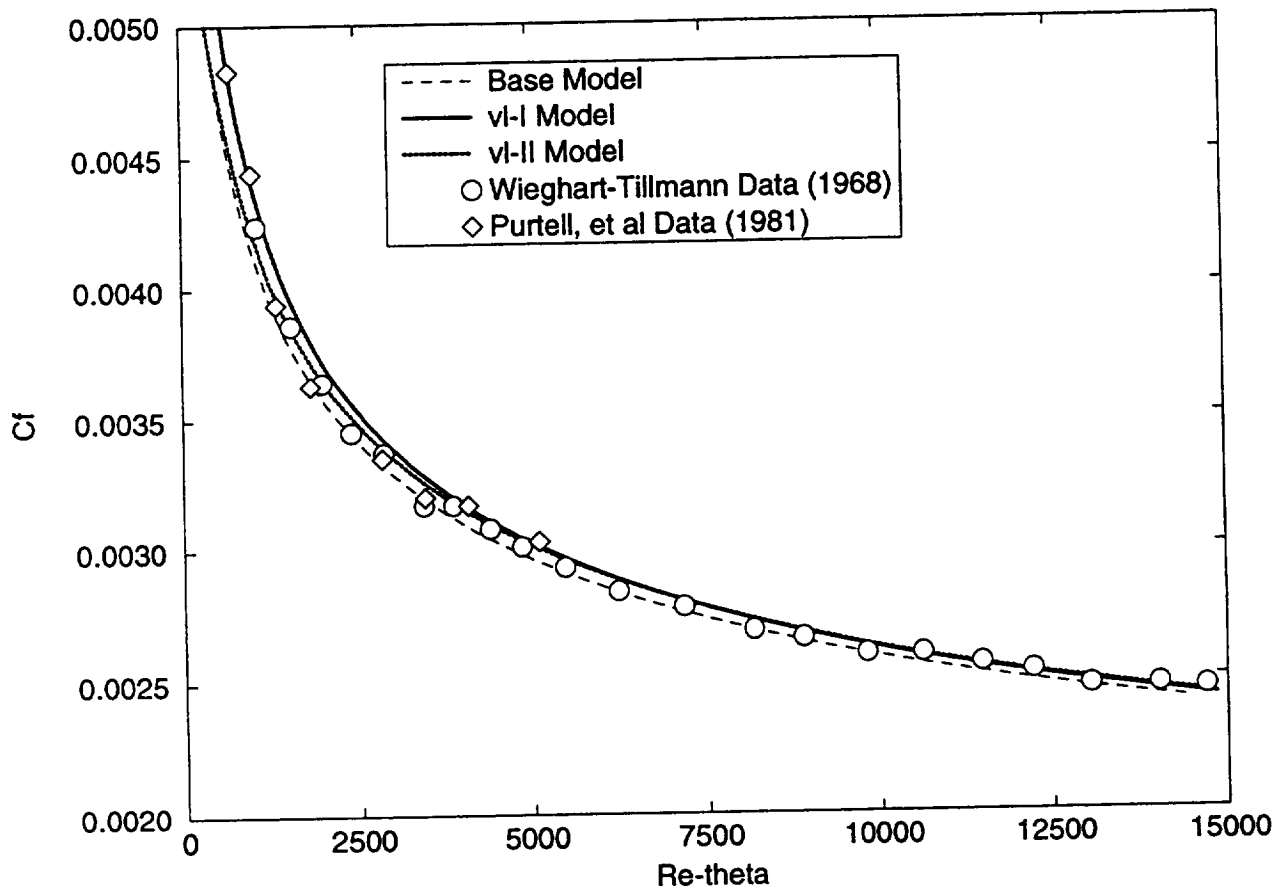


Figure 3.9 Comparison of wall skin friction coefficients predicted by using the $v'l$ -I, $v'l$ -II, and base $k-\epsilon$ turbulence models with measured data for a two-dimensional zero pressure gradient turbulent boundary layer.

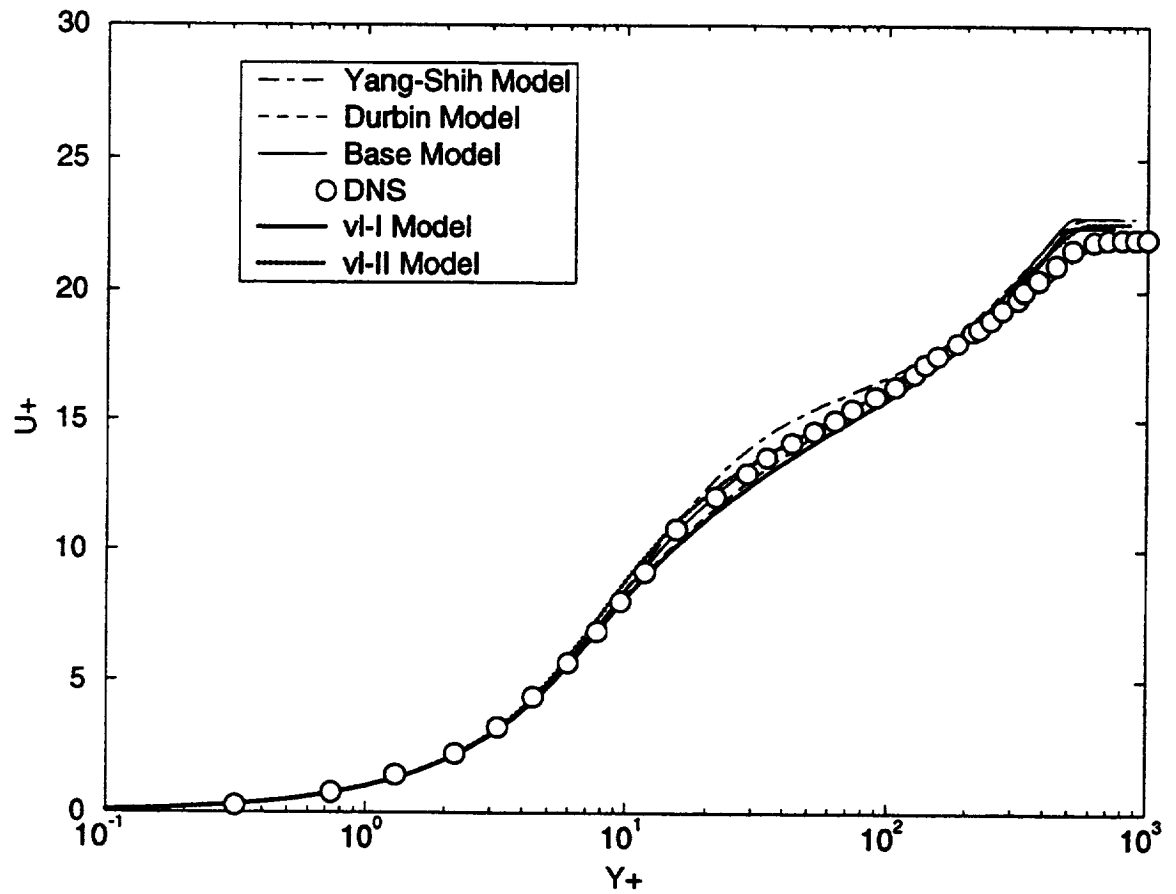


Figure 3.10 Comparison of mean velocity profiles predicted by using various $k-\epsilon$ based turbulence models with Spalart's DNS data for a two-dimensional zero pressure gradient turbulent boundary layer at $Re_\theta = 1410$.

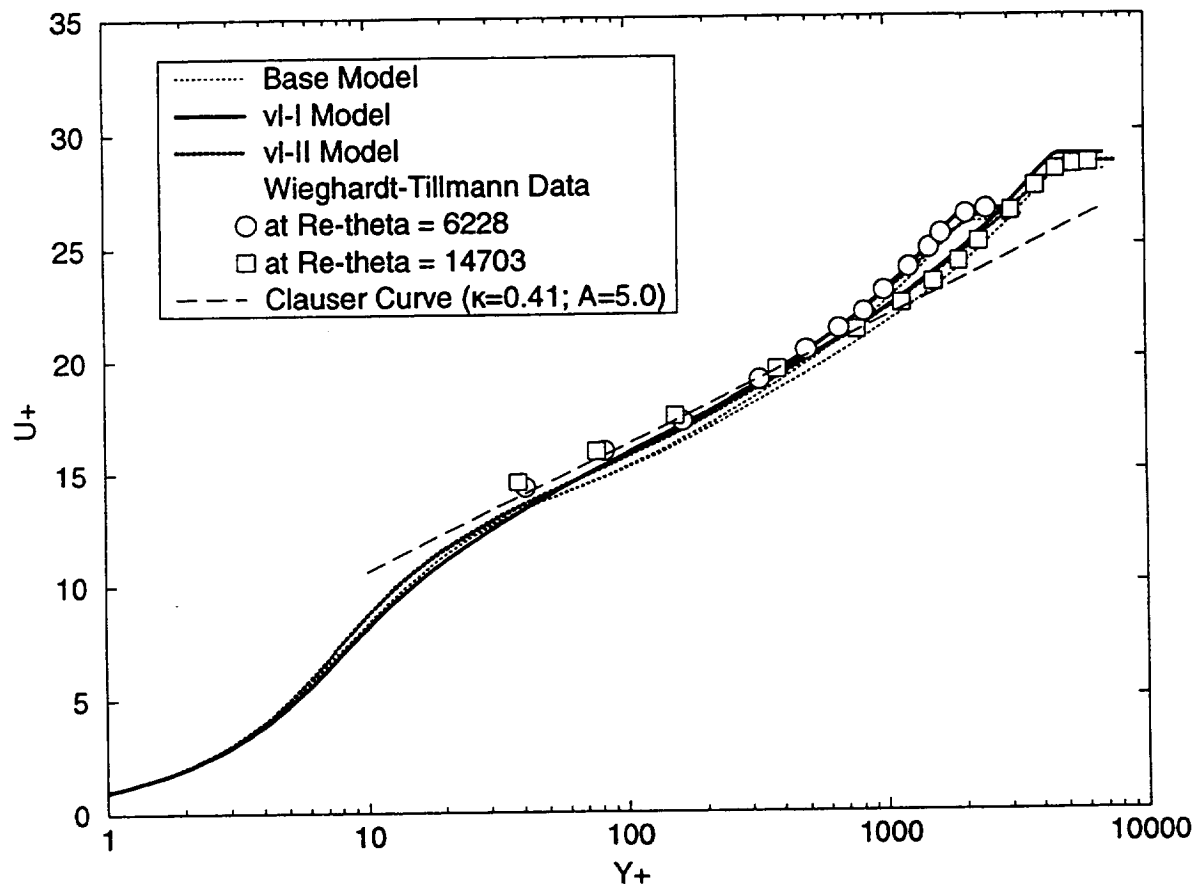


Figure 3.11 Comparison of mean velocity profiles predicted by using the $v'l$ -I, $v'l$ -II, and base k - ϵ turbulence models with measured data and the Clauser curve ($\kappa = 0.41$, $A = 5.0$) for a two-dimensional zero pressure gradient turbulent boundary layer at $Re_\theta = 6,228$ and $14,703$.

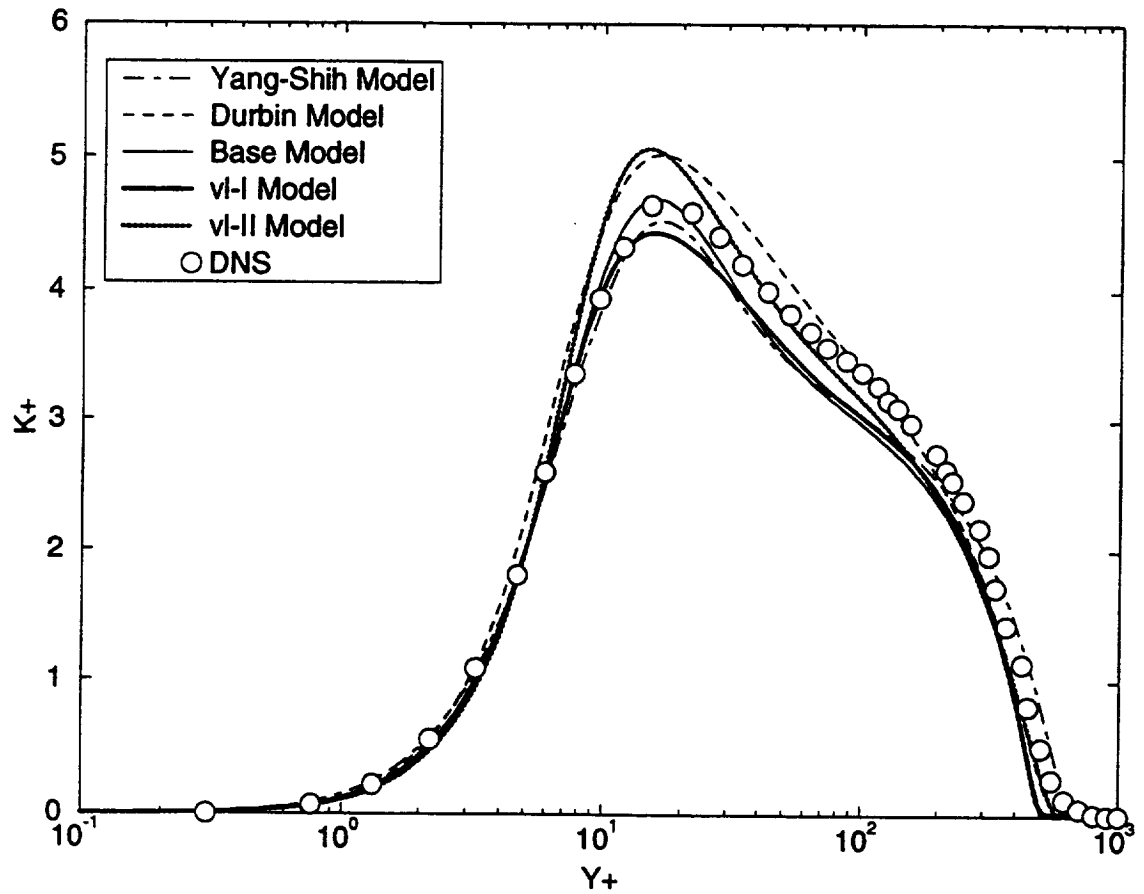


Figure 3.12 Comparison of turbulent kinetic energy profiles predicted by using various k - ϵ based turbulence models with Spalart's DNS data for a two-dimensional zero pressure gradient turbulent boundary layer at $Re_\theta = 1410$.

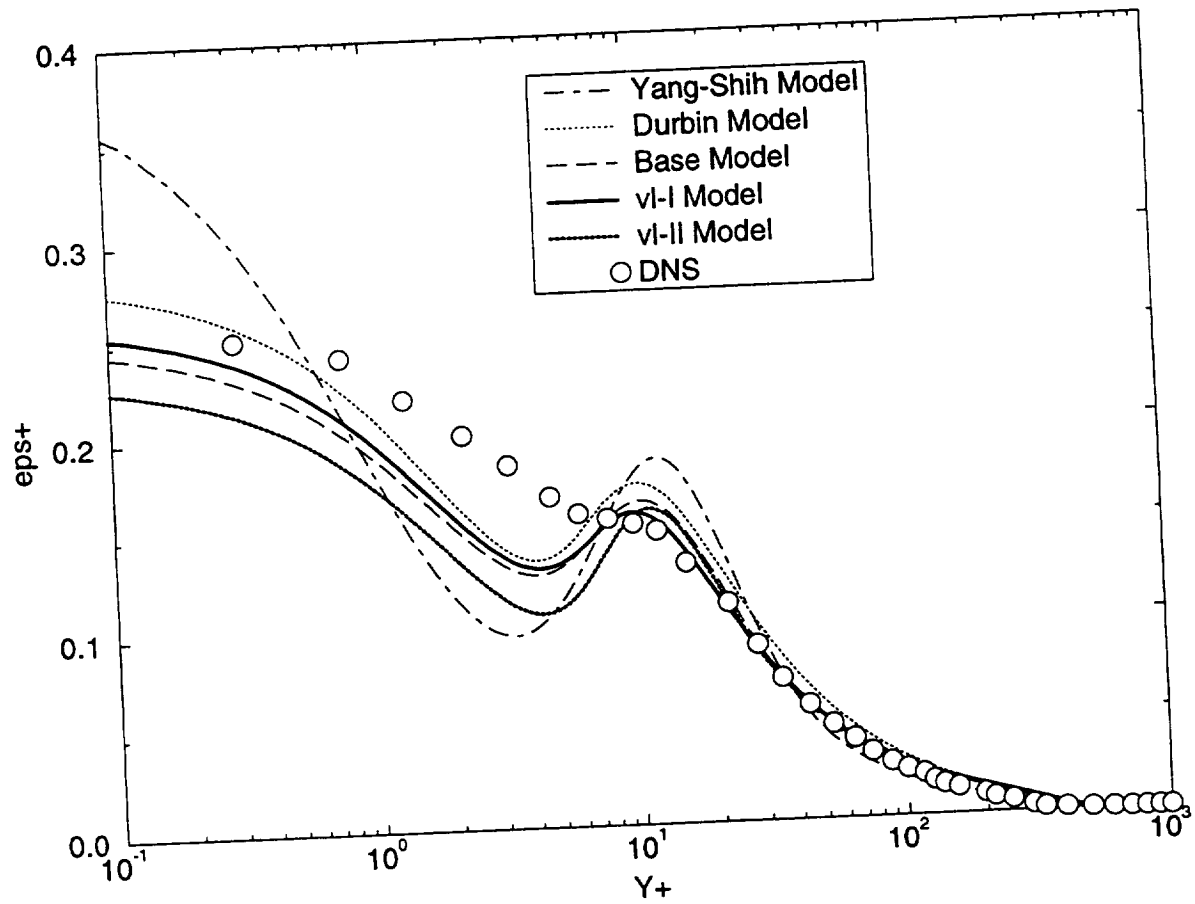


Figure 3.13 Comparison of dissipation rate profiles predicted by using various $k-\epsilon$ based turbulence models with Spalart's DNS data for a two-dimensional zero pressure gradient turbulent boundary layer at $Re_\theta = 1410$.

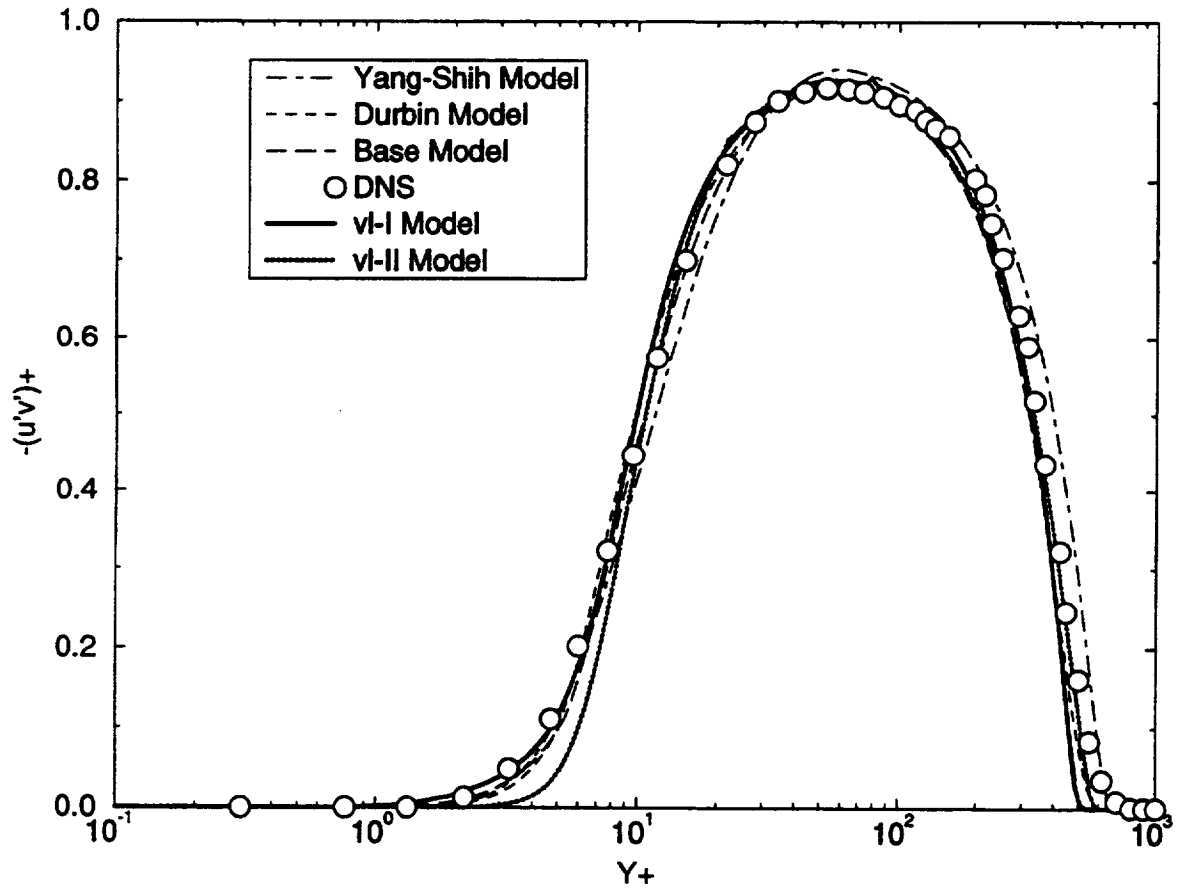


Figure 3.14 Comparison of shear stress profiles predicted by using various $k-\epsilon$ based turbulence models with Spalart's DNS data for a two-dimensional zero pressure gradient turbulent boundary layer at $Re_\theta = 1410$.

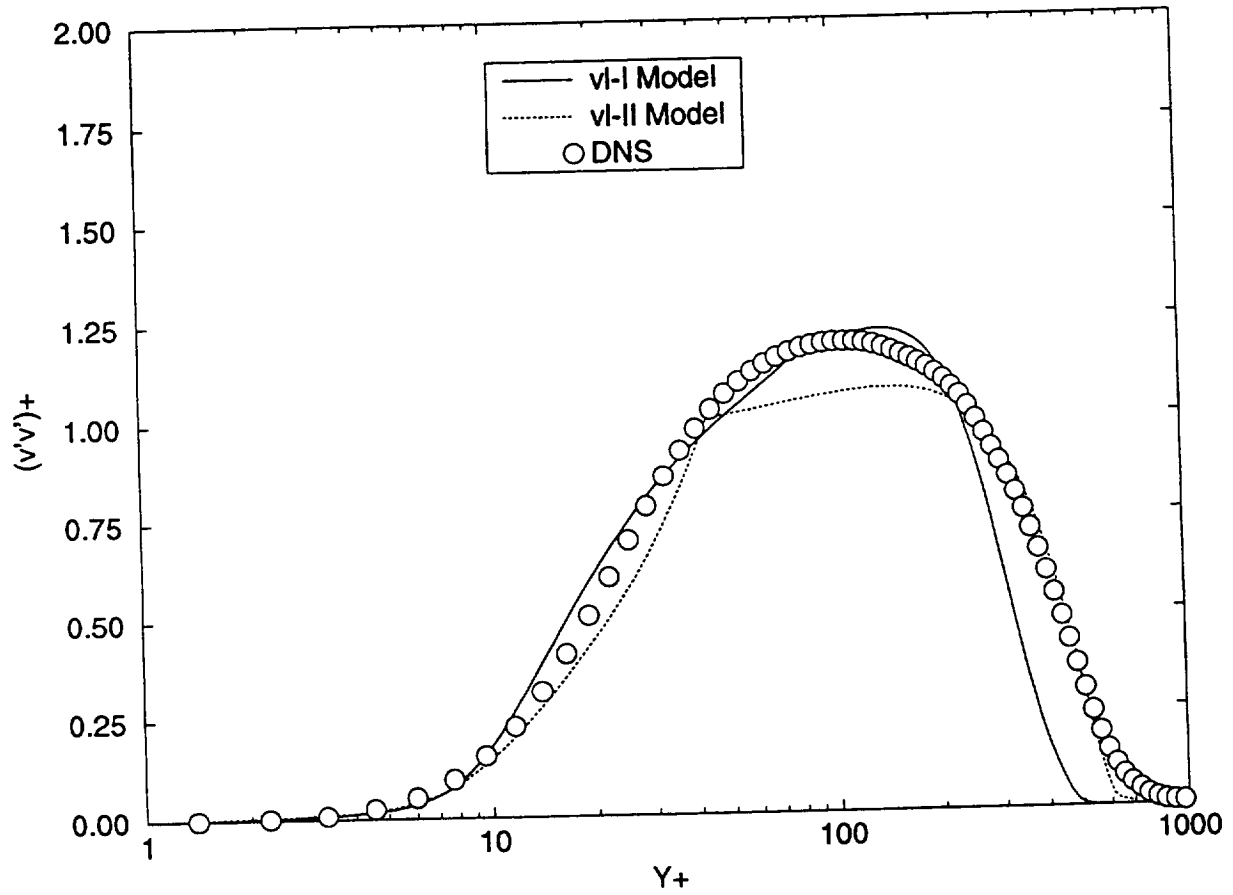


Figure 3.15 Comparison of normal component turbulent velocity profiles predicted by using the $v'l$ -I and $v'l$ -II models with Spalart's DNS data for a two-dimensional zero pressure gradient turbulent boundary layer at $Re_\theta = 1410$.

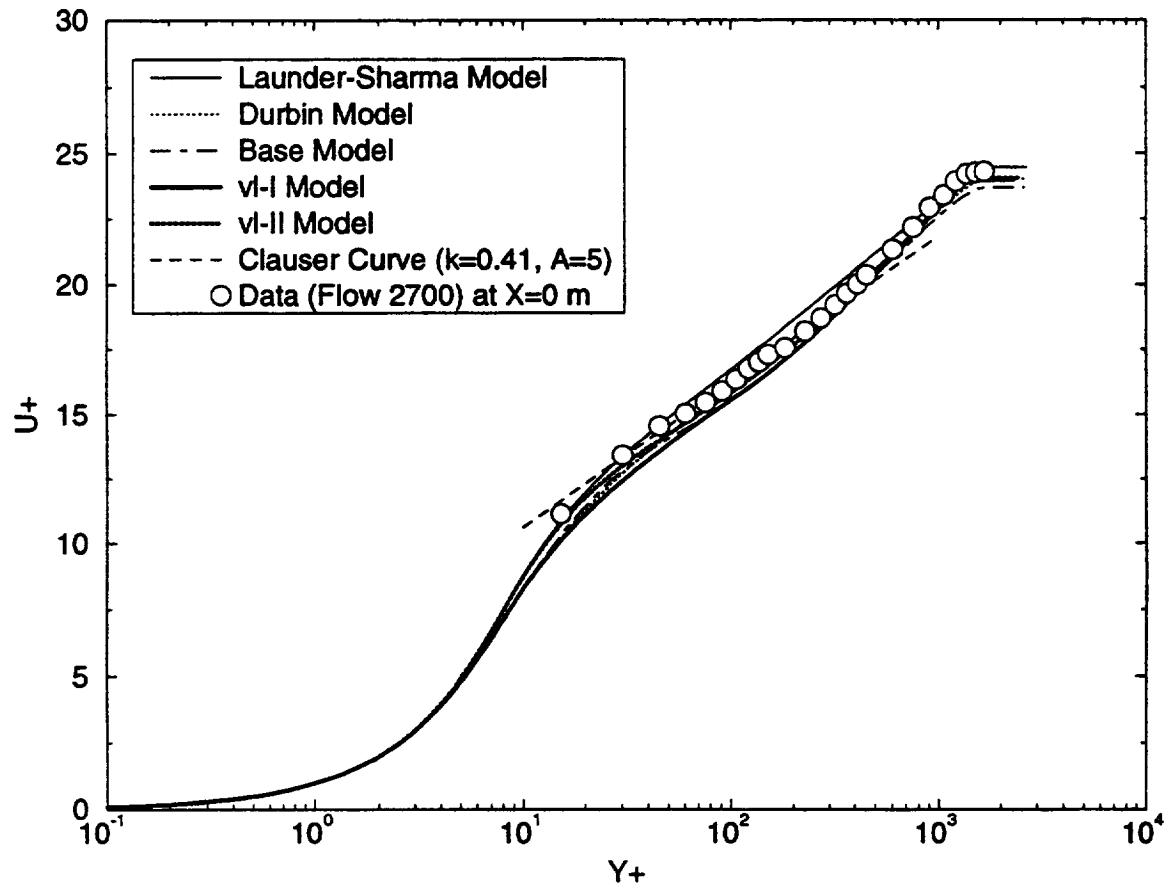


Figure 3.16 Comparison of mean velocity profiles predicted by using various k - ϵ based turbulence models with measured data and the Clauser curve ($\kappa = 0.41$, $A = 5.0$) for an equilibrium boundary layer with favorable pressure gradient (Herring and Norbury measurements: Flow 2700) at $x = 0.0$ m.

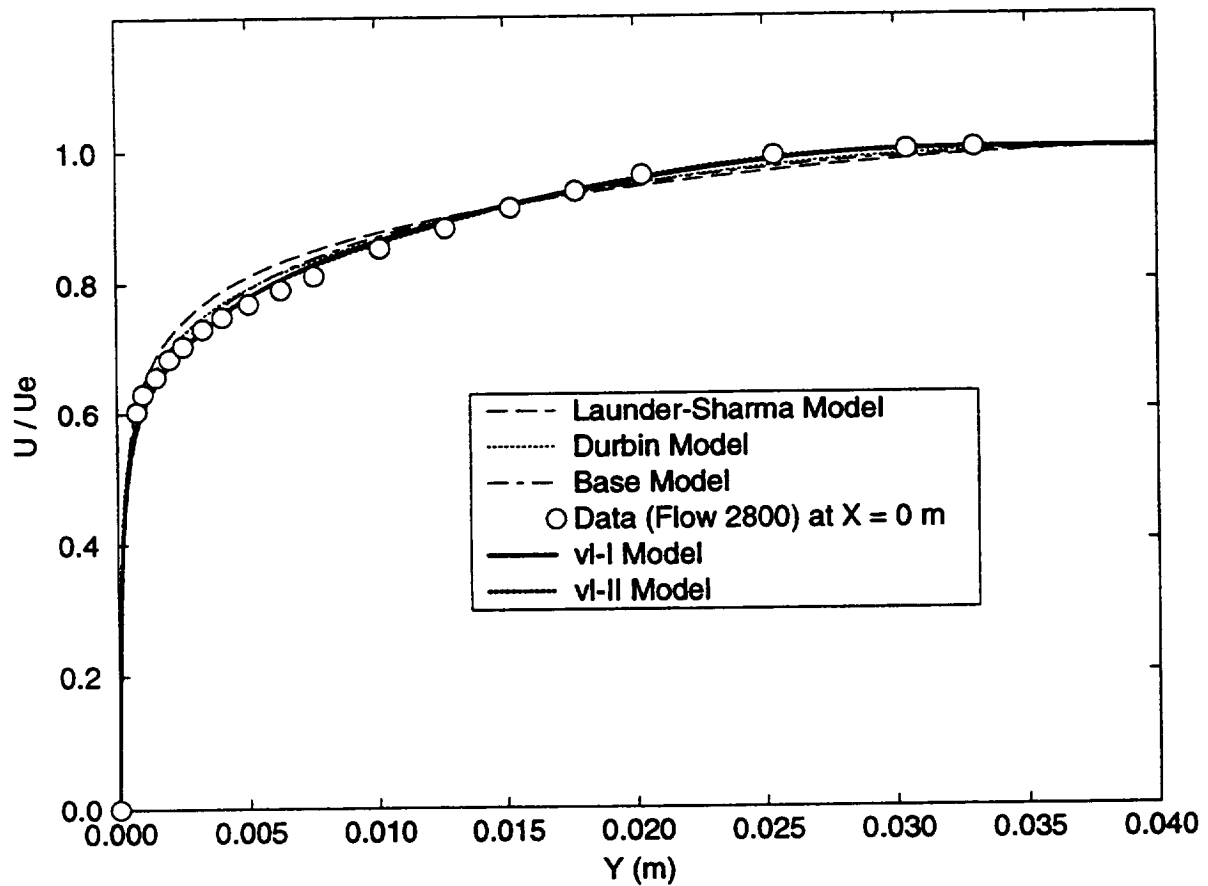


Figure 3.17 Comparison of mean velocity profiles predicted by using various $k-\epsilon$ based turbulence models with measured data for an accelerating flow (Herring and Norbury measurements: Flow 2800) at $x = 0.0$ m.

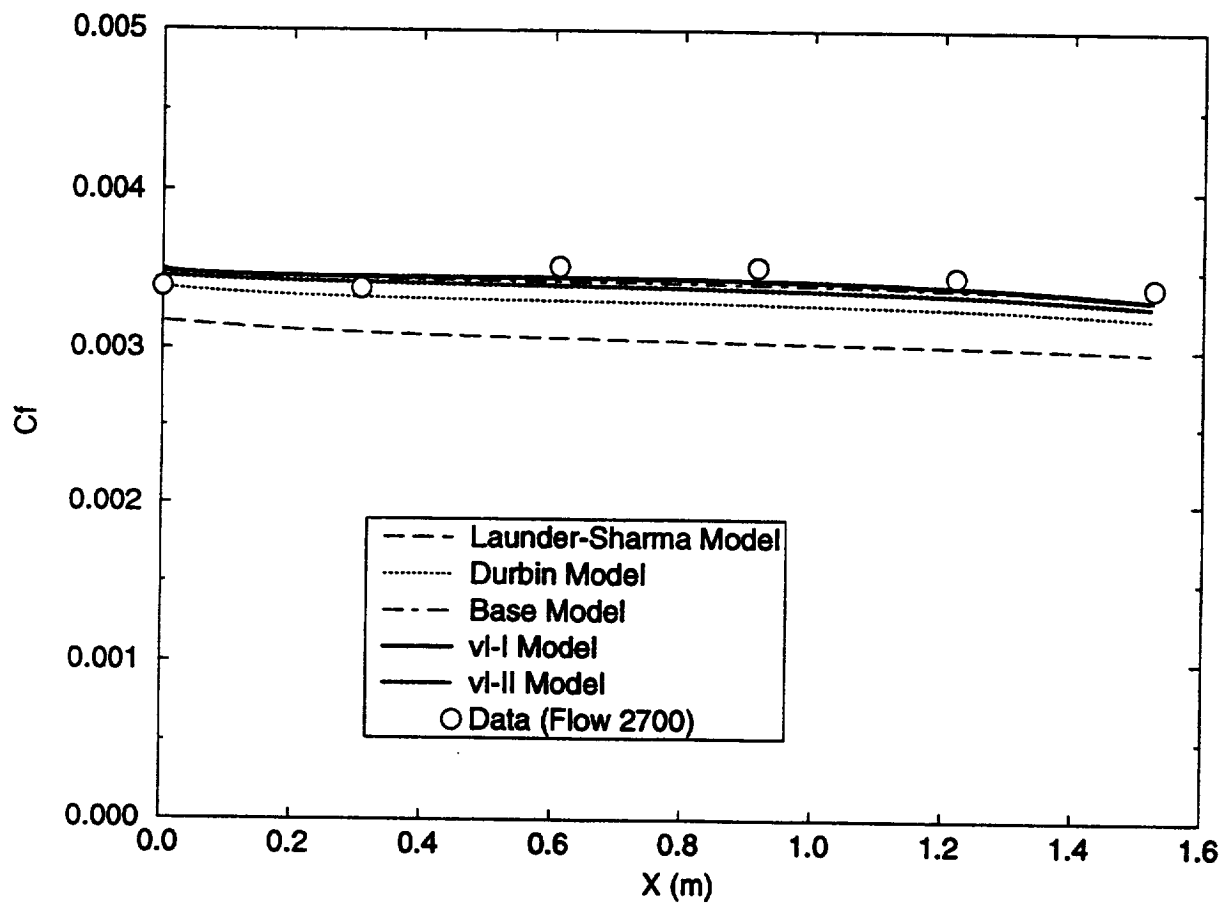


Figure 3.18 Comparison of wall skin friction coefficients predicted by using various k - ϵ based turbulence models with measured data for an equilibrium boundary layer with favorable pressure gradient (Herring and Norbury measurements: Flow 2700).

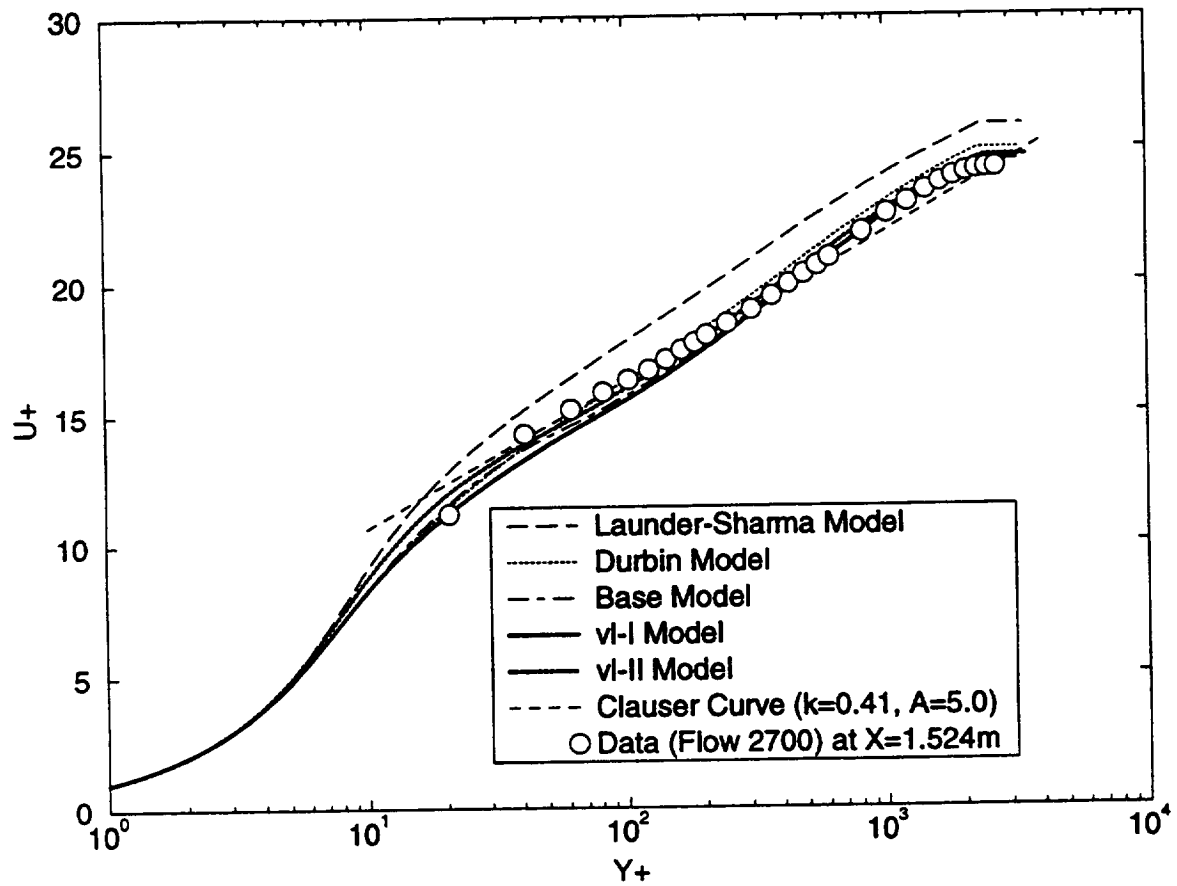


Figure 3.19 Comparison of mean velocity profiles predicted by using various k - ϵ based turbulence models with measured data and the Clauser curve ($\kappa = 0.41$, $A = 5.0$) for an equilibrium boundary layer with favorable pressure gradient (Herring and Norbury measurements: Flow 2700) at $x = 1.524$ m.

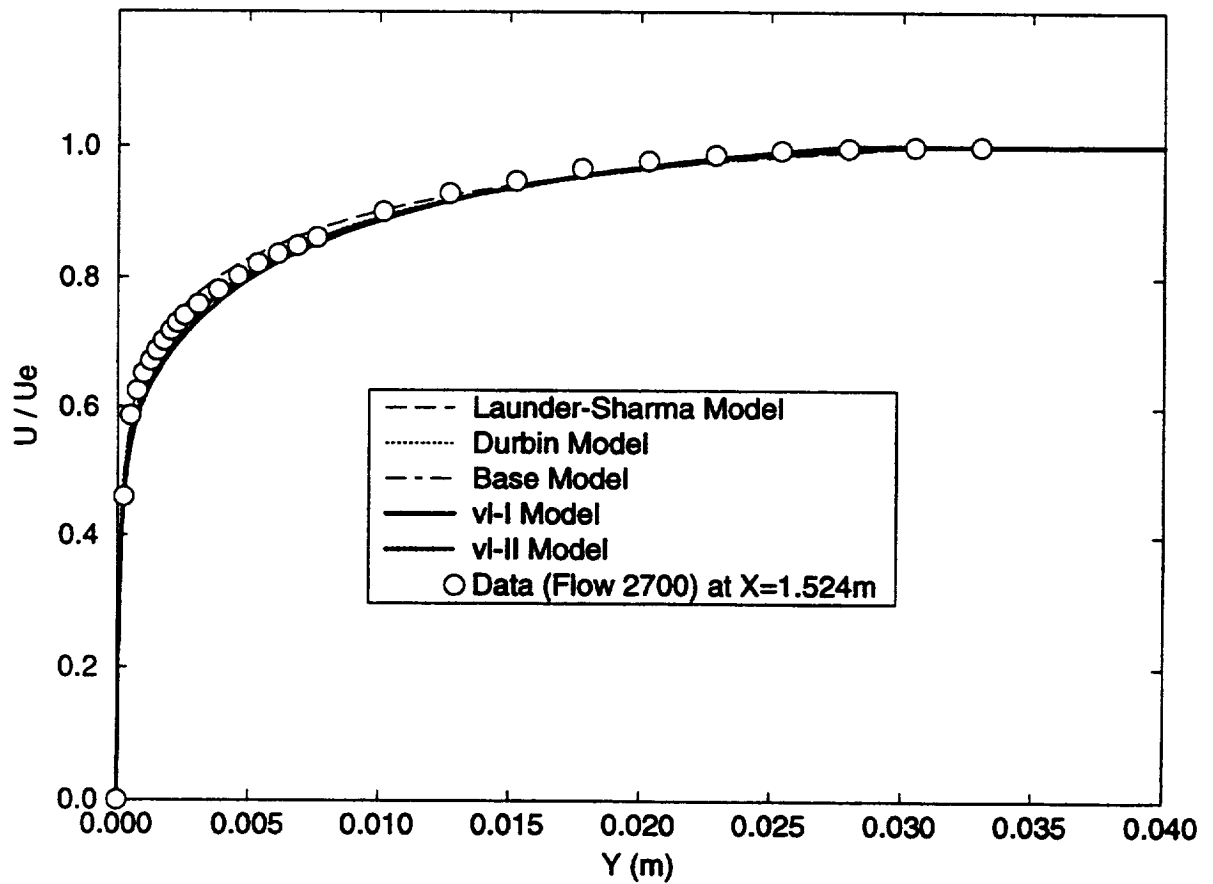


Figure 3.20 Comparison of mean velocity profiles predicted by using various k - ϵ based turbulence models with measured data for an equilibrium boundary layer with favorable pressure gradient (Herring and Norbury measurements: Flow 2700) at $x = 1.524$ m.

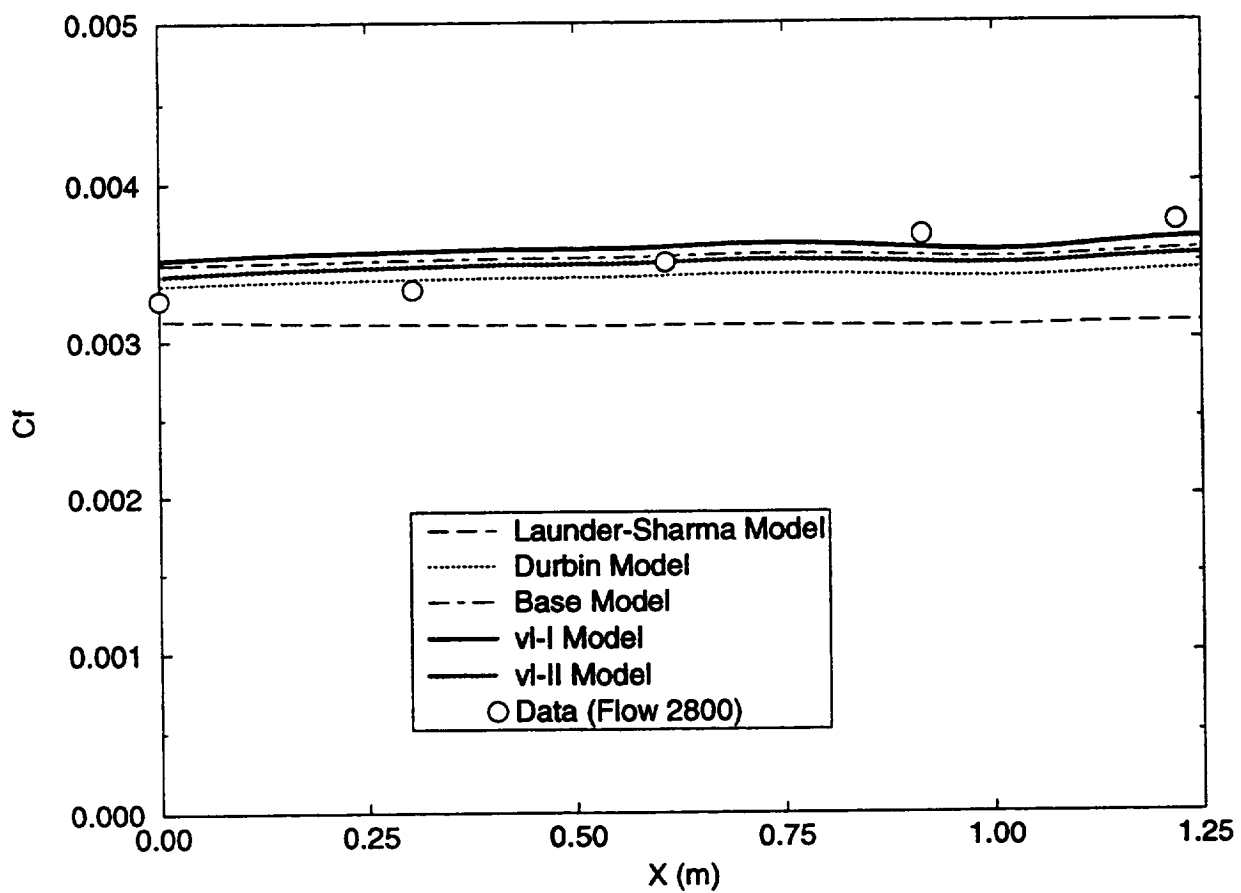


Figure 3.21 Comparison of wall skin friction coefficients predicted by using various k - ϵ based turbulence models with measured data for an accelerating flow (Herring and Norbury measurements: Flow 2800).

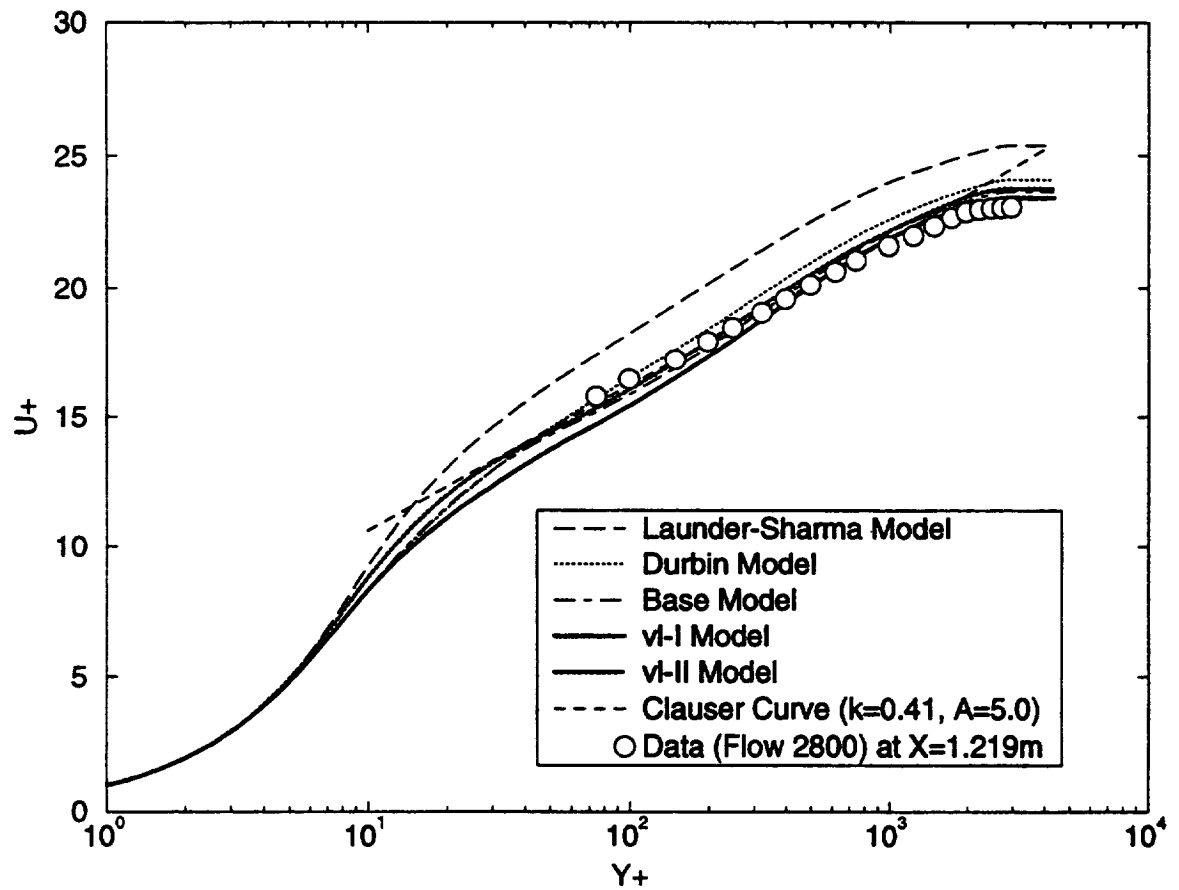


Figure 3.22 Comparison of mean velocity profiles predicted by using various k - ϵ based turbulence models with measured data and the Clauser curve ($\kappa = 0.41$, $A = 5.0$) for an accelerating flow (Herring and Norbury measurements: Flow 2800) at $x = 1.219$ m.

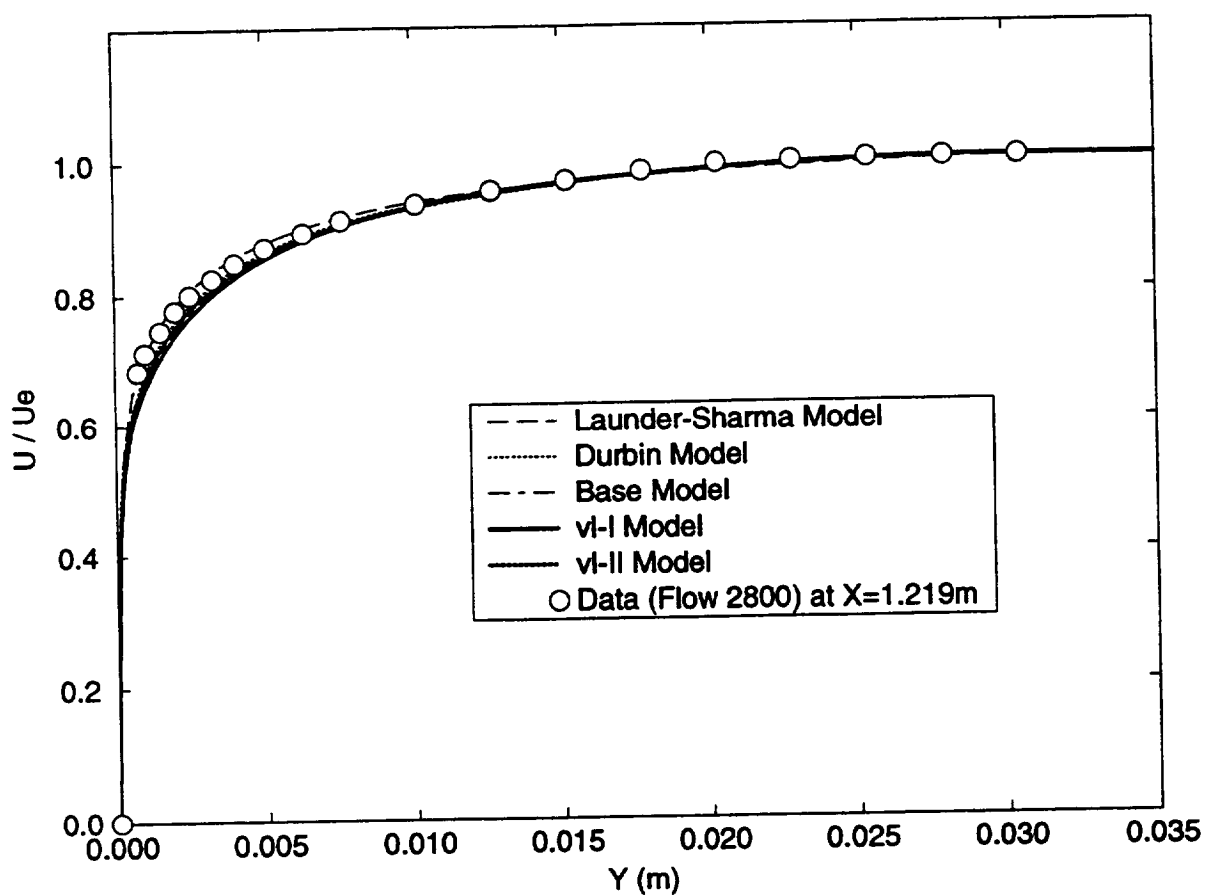


Figure 3.23 Comparison of mean velocity profiles predicted by using various $k-\epsilon$ based turbulence models with measured data for an accelerating flow (Herring and Norbury measurements: Flow 2800) at $x = 1.219$ m.

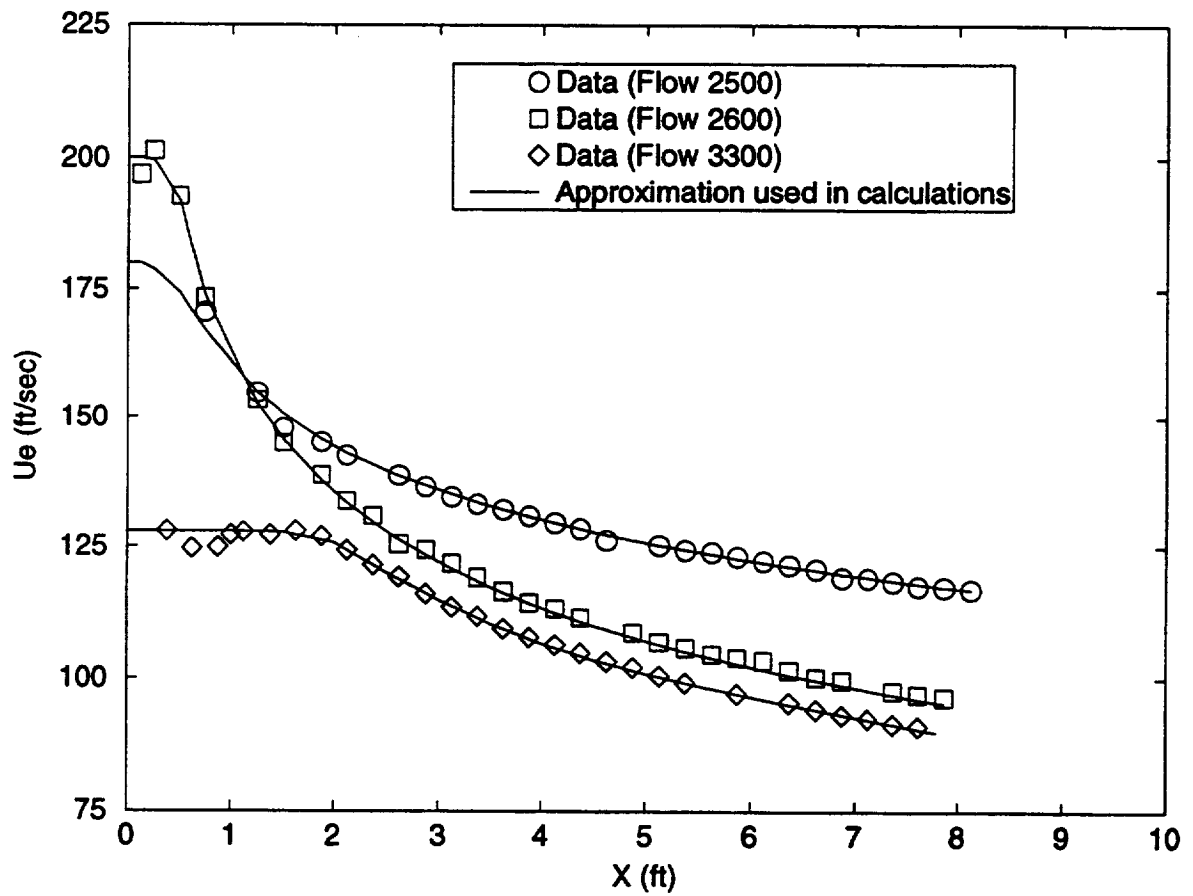


Figure 3.24 Freestream velocity distributions for Bradshaw's experiments of flow 2500, 2600, and 3300. The solid lines represent the approximated distributions used in the calculations.

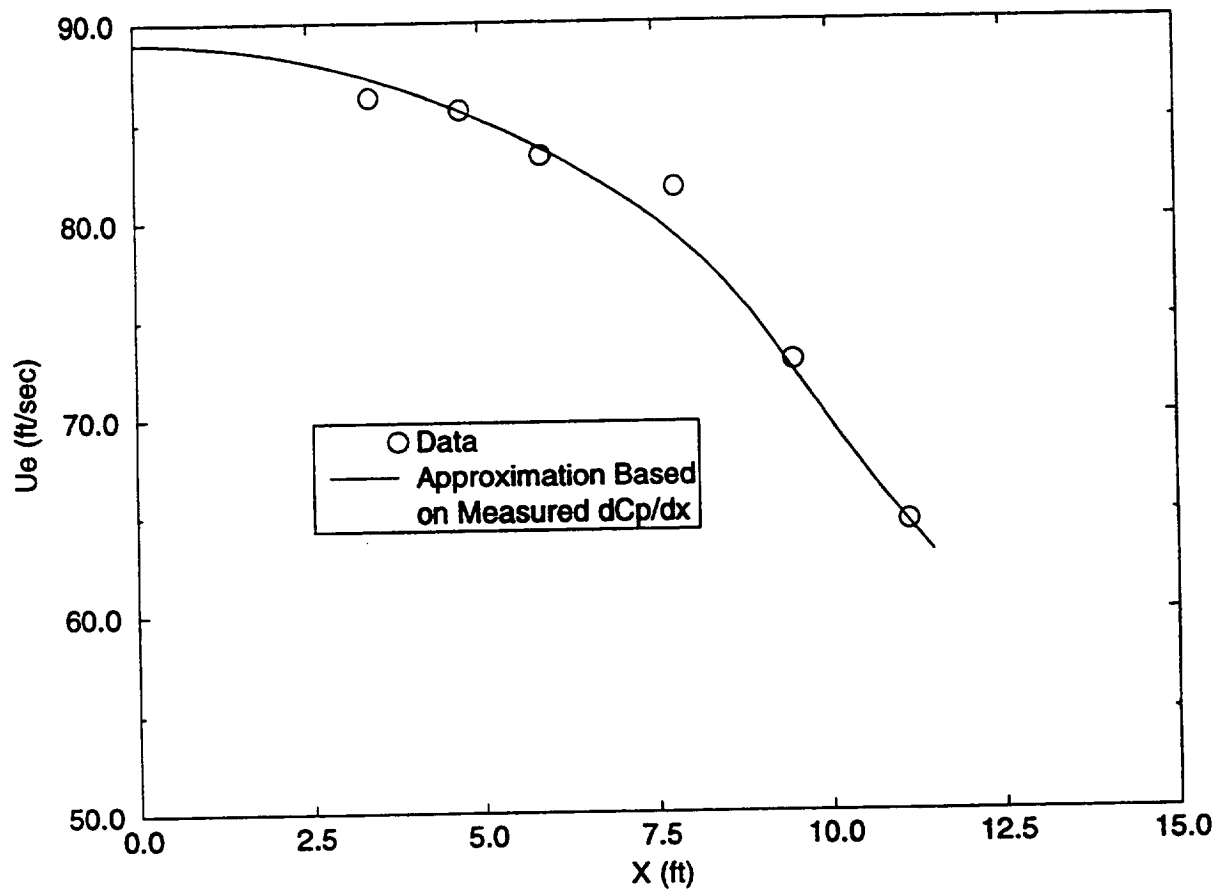


Figure 3.25 Freestream velocity distributions for the experimental data set of Samuel and Joubert. The solid line represents the approximated distribution used in the calculations.

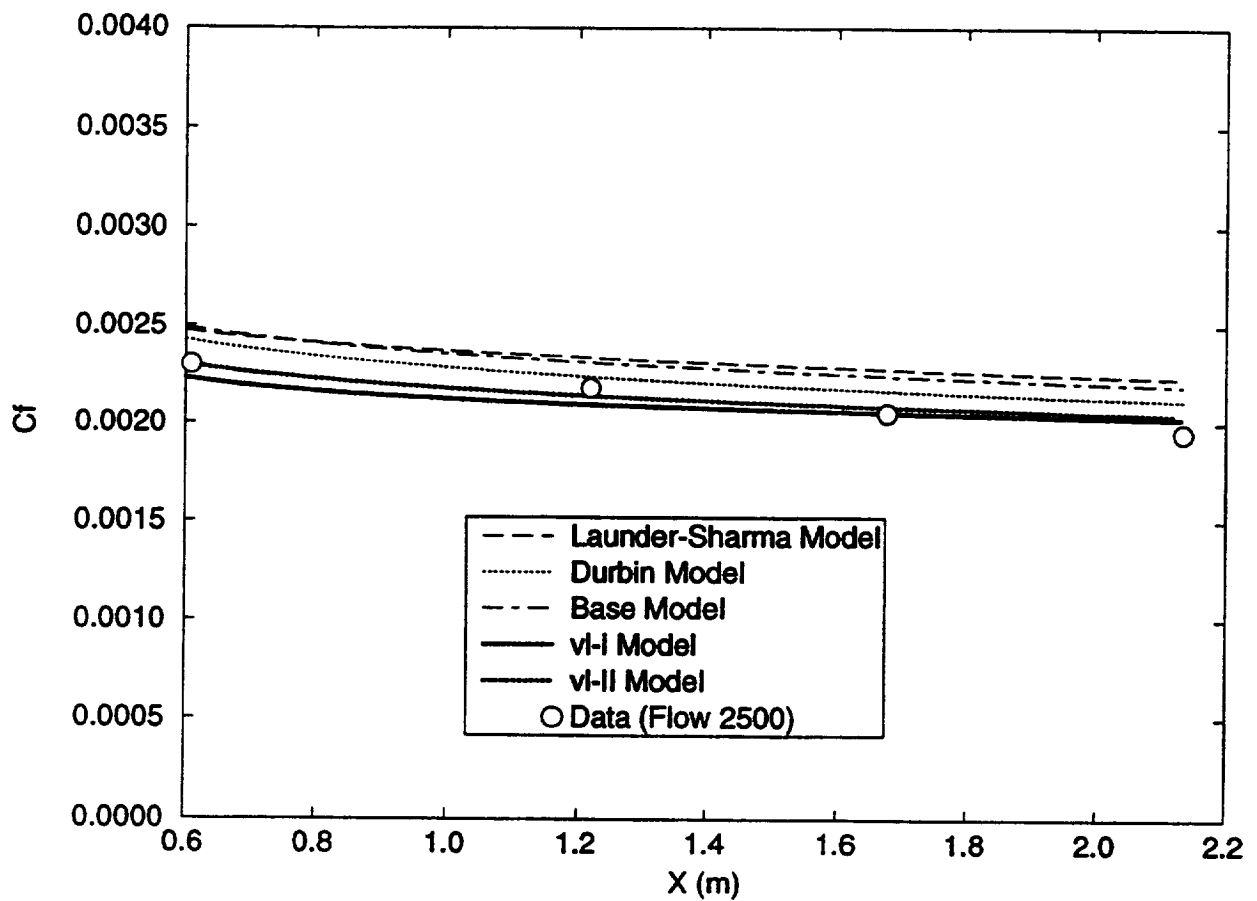


Figure 3.26 Comparison of wall skin friction coefficients predicted by using various k - ϵ based turbulence models with measured data for an equilibrium boundary layer with adverse pressure gradient (Bradshaw measurements: Flow 2500).

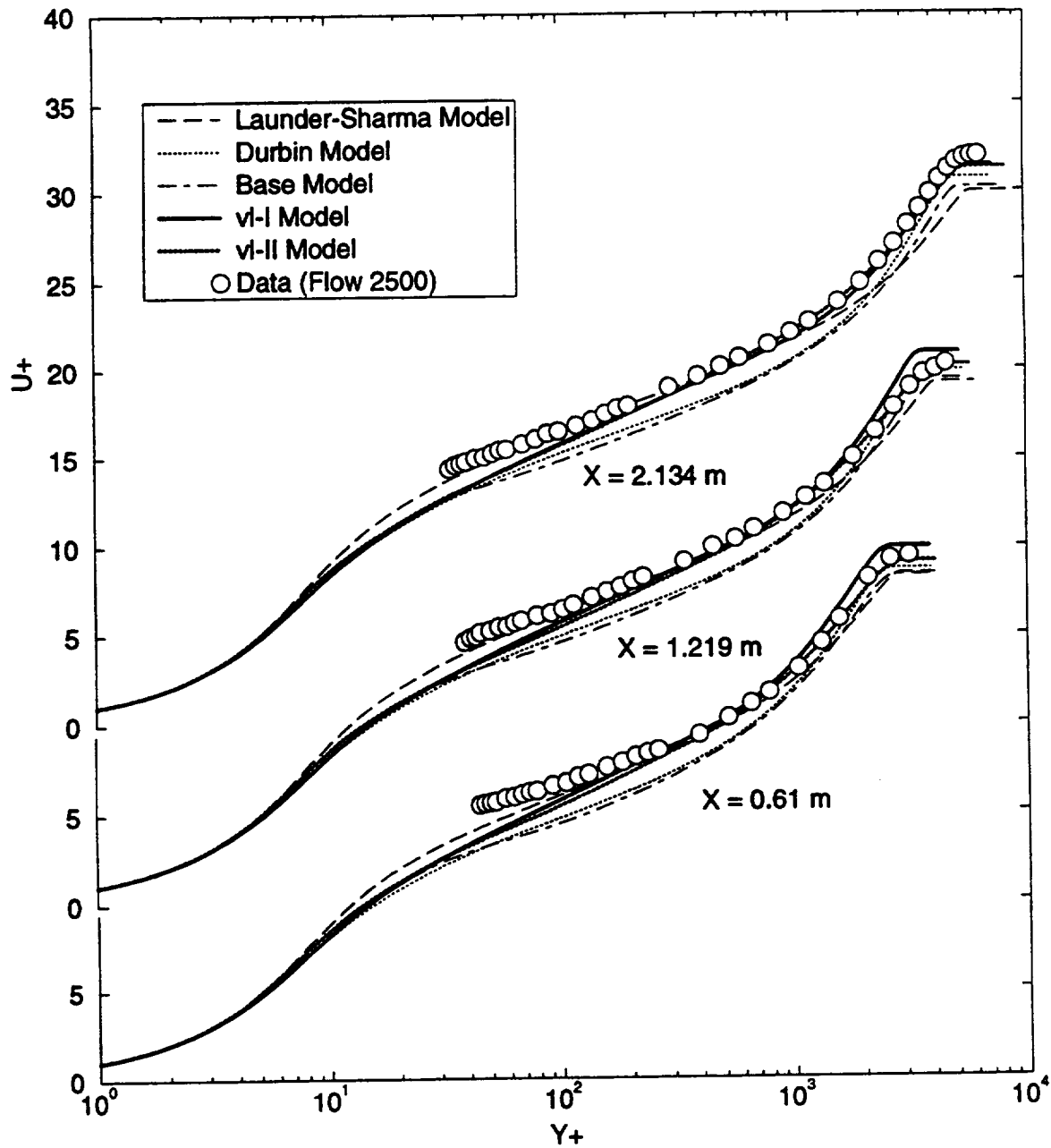


Figure 3.27 Comparison of mean velocity profiles predicted by using various $k-\epsilon$ based turbulence models with measured data for an equilibrium boundary layer with adverse pressure gradient (Bradshaw measurements: Flow 2500) at $x = 0.610$ m, 1.219 m, and 2.134 m.

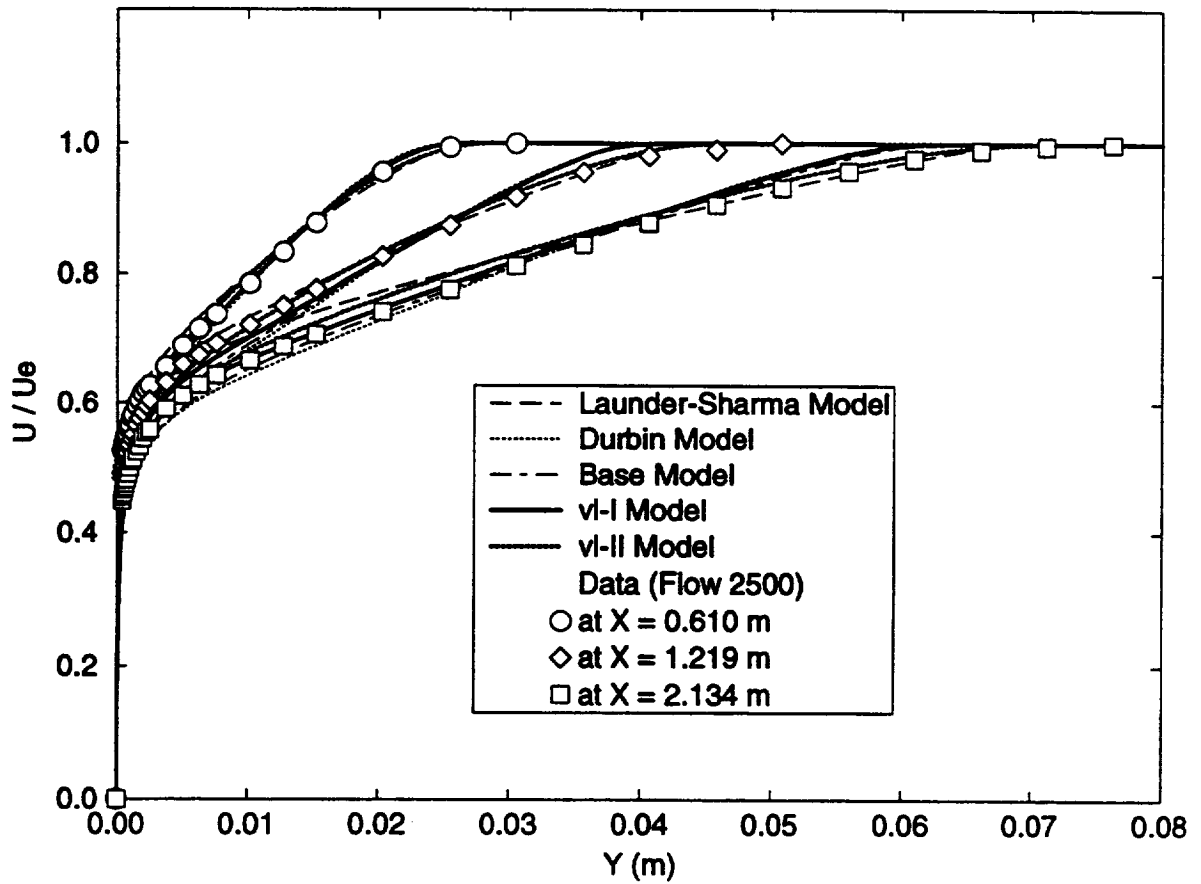


Figure 3.28 Comparison of mean velocity profiles predicted by using various $k-\epsilon$ based turbulence models with measured data for an equilibrium boundary layer with adverse pressure gradient (Bradshaw measurements: Flow 2500) at $x = 0.610$ m, 1.219m, and 2.134 m.

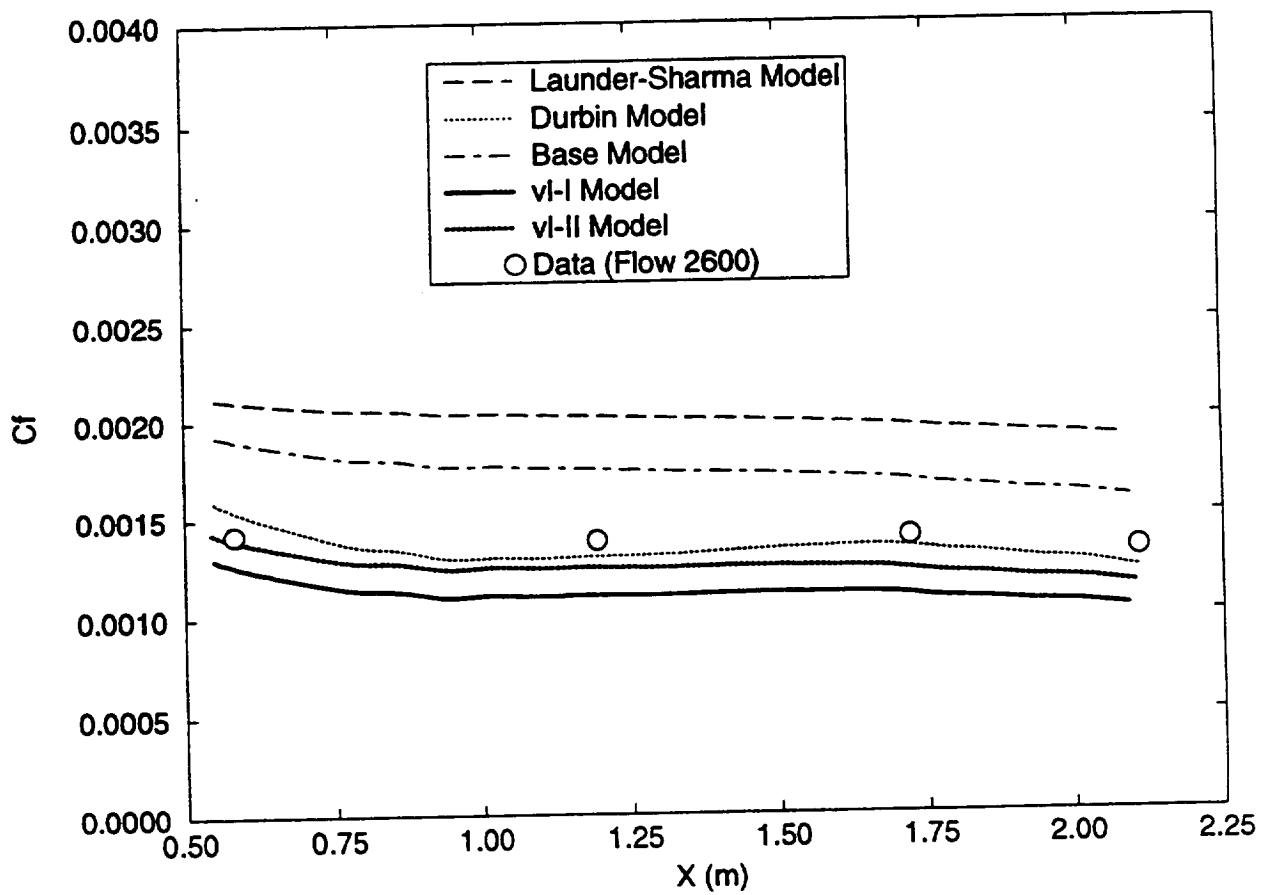


Figure 3.29 Comparison of wall skin friction coefficients predicted by using various k- ϵ based turbulence models with measured data for an equilibrium boundary layer with adverse pressure gradient (Bradshaw measurements: Flow 2600).

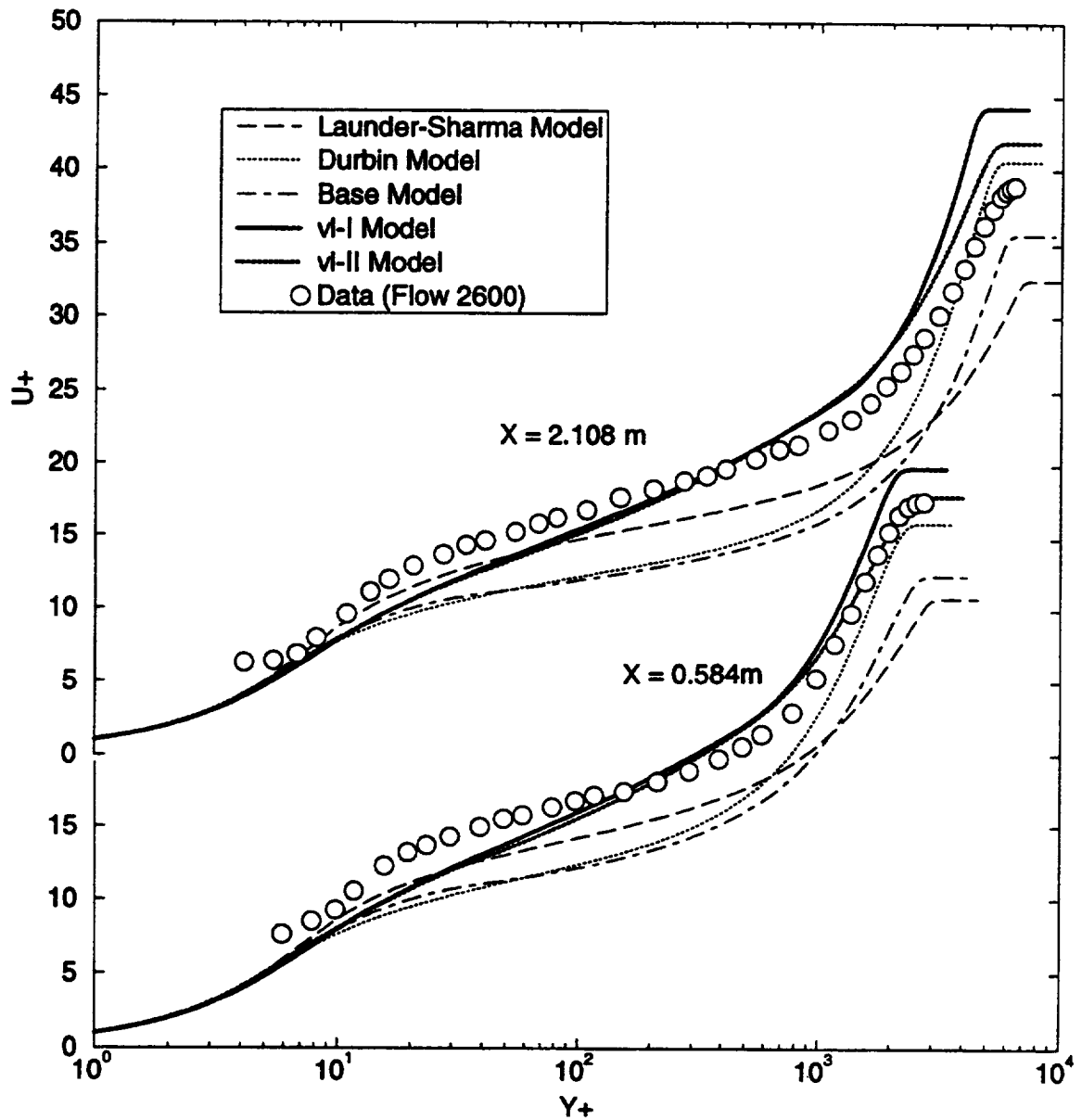


Figure 3.30 Comparison of mean velocity profiles predicted by using various k - ϵ based turbulence models with measured data for an equilibrium boundary layer with adverse pressure gradient (Bradshaw measurements: Flow 2600) at $x = 0.584 \text{ m}$ and 2.108 m .

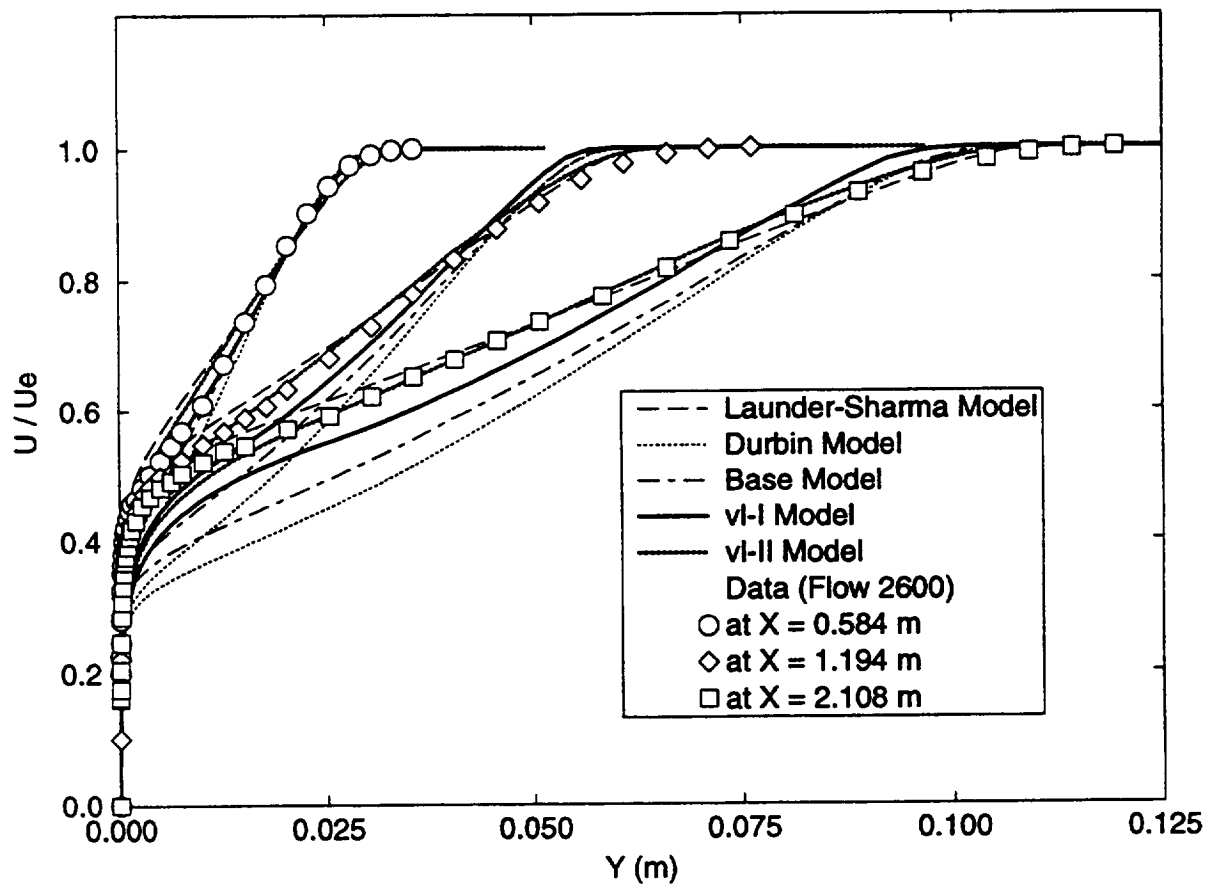


Figure 3.31 Comparison of mean velocity profiles predicted by using various $k-\epsilon$ based turbulence models with measured data for an equilibrium boundary layer with adverse pressure gradient (Bradshaw measurements: Flow 2600) at $x = 0.584$ m, 1.194 m, and 2.108 m.

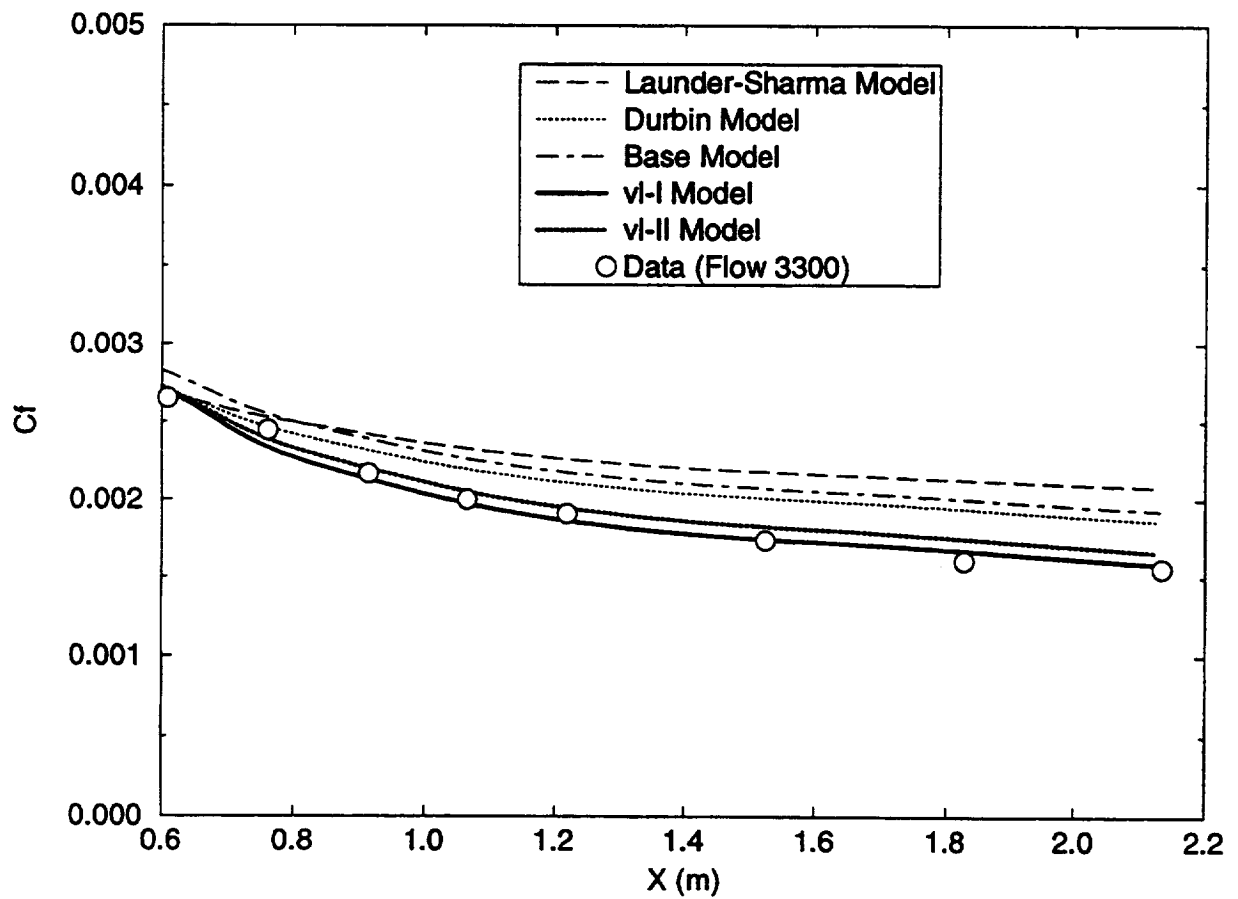


Figure 3.32 Comparison of wall skin friction coefficients predicted by using various k - ϵ based turbulence models with measured data for a boundary layer with sudden adverse pressure gradient (Bradshaw measurements: Flow 3300).

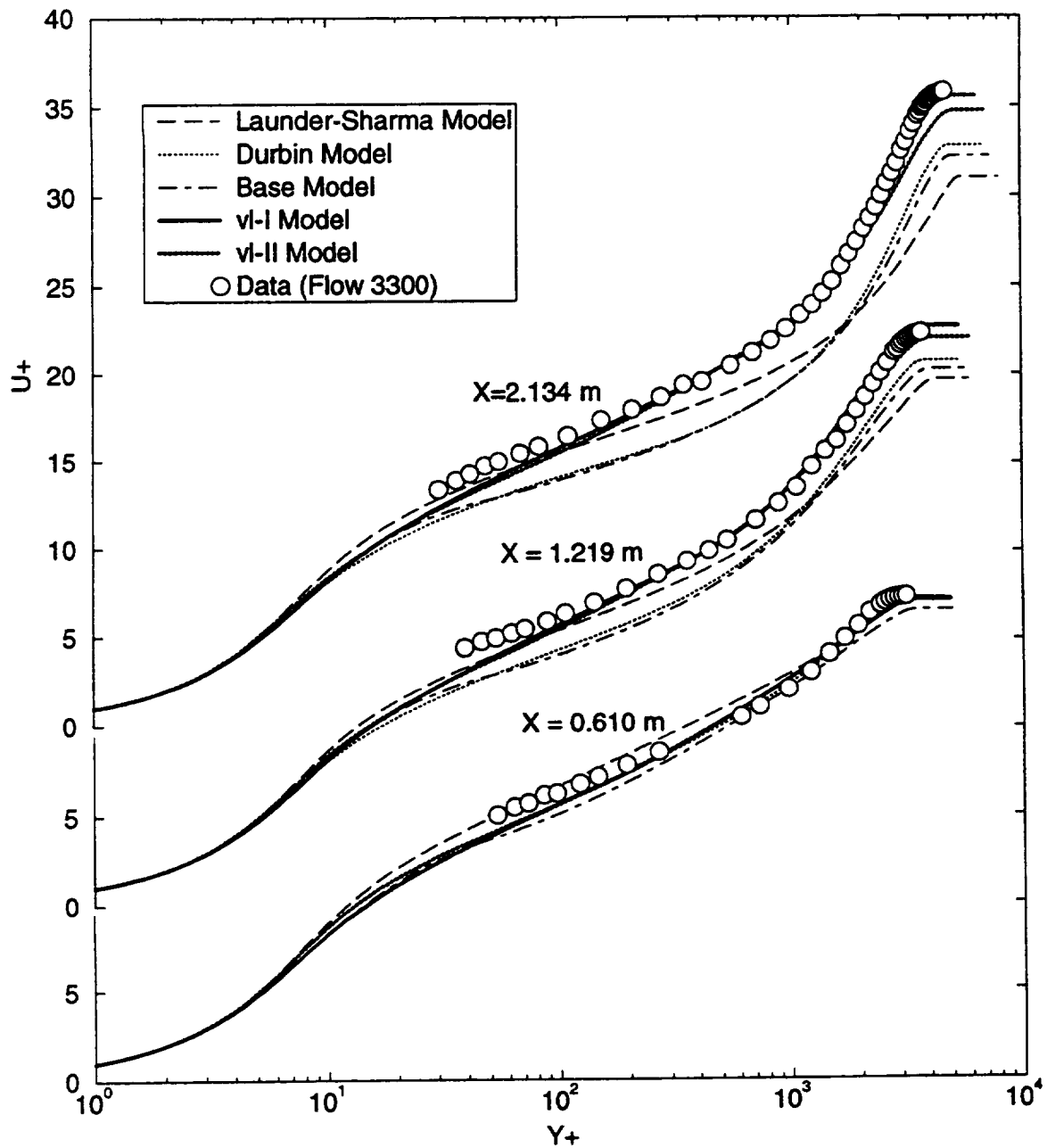


Figure 3.33 Comparison of mean velocity profiles predicted by using various k - ϵ based turbulence models with measured data for a boundary layer with sudden adverse pressure gradient (Bradshaw measurements: Flow 3300) at $x = 0.610$ m, 1.219 m, and 2.134 m.

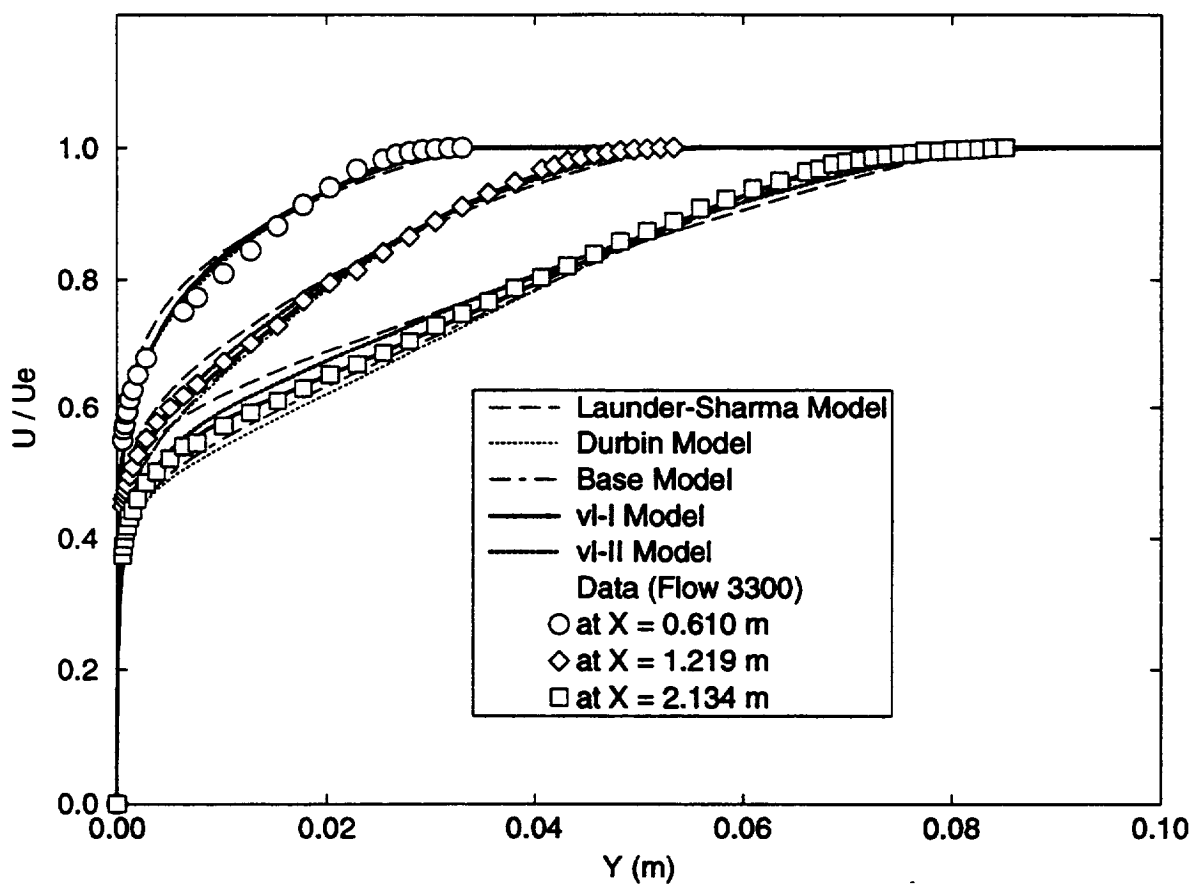


Figure 3.34 Comparison of mean velocity profiles predicted by using various $k-\epsilon$ based turbulence models with measured data for a boundary layer with sudden adverse pressure gradient (Bradshaw measurements: Flow 3300) at $x = 0.610$ m, 1.219 m, and 2.134 m.

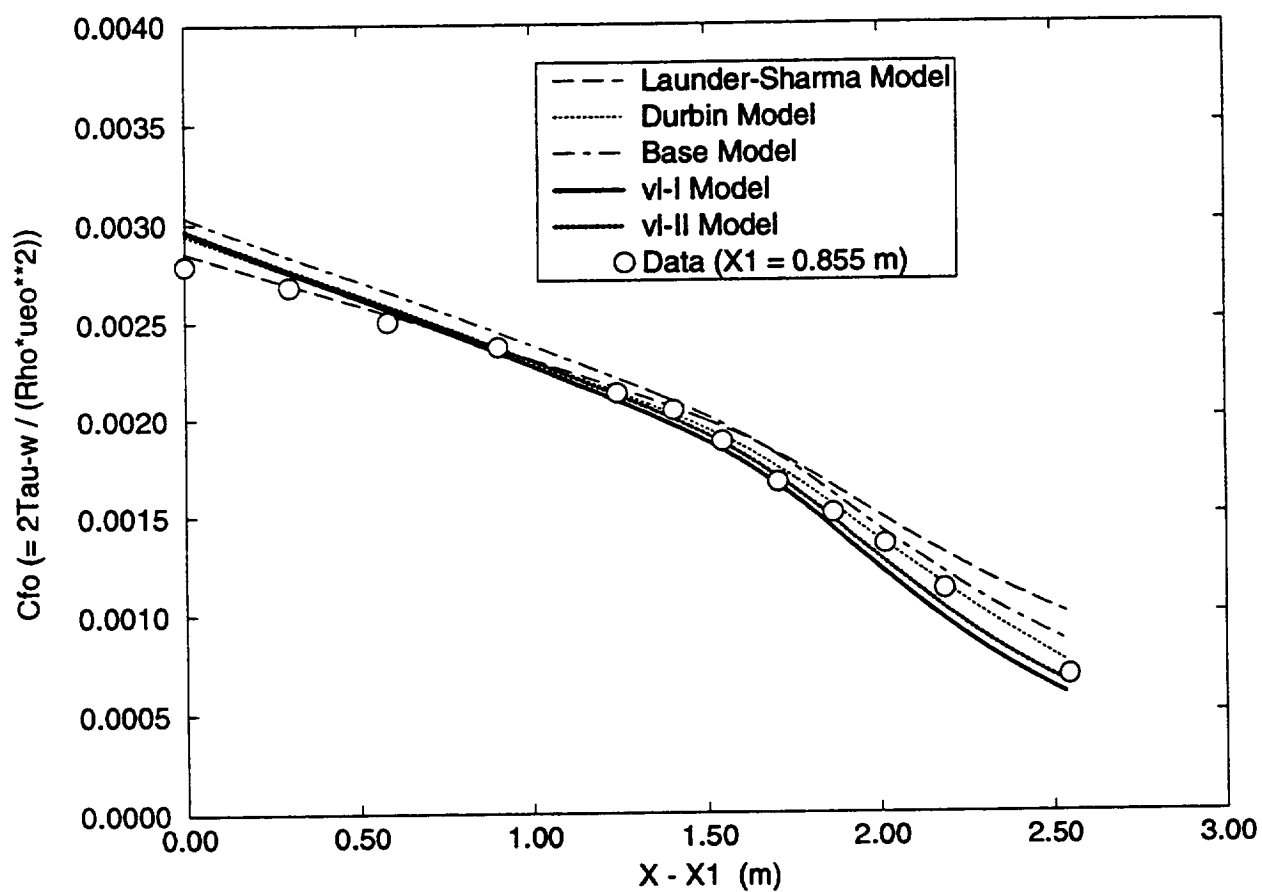


Figure 3.35 Comparison of skin friction coefficients predicted by using various $k-\epsilon$ based turbulence models with measured data for an increasingly adverse pressure gradient flow of Samuel and Joubert.

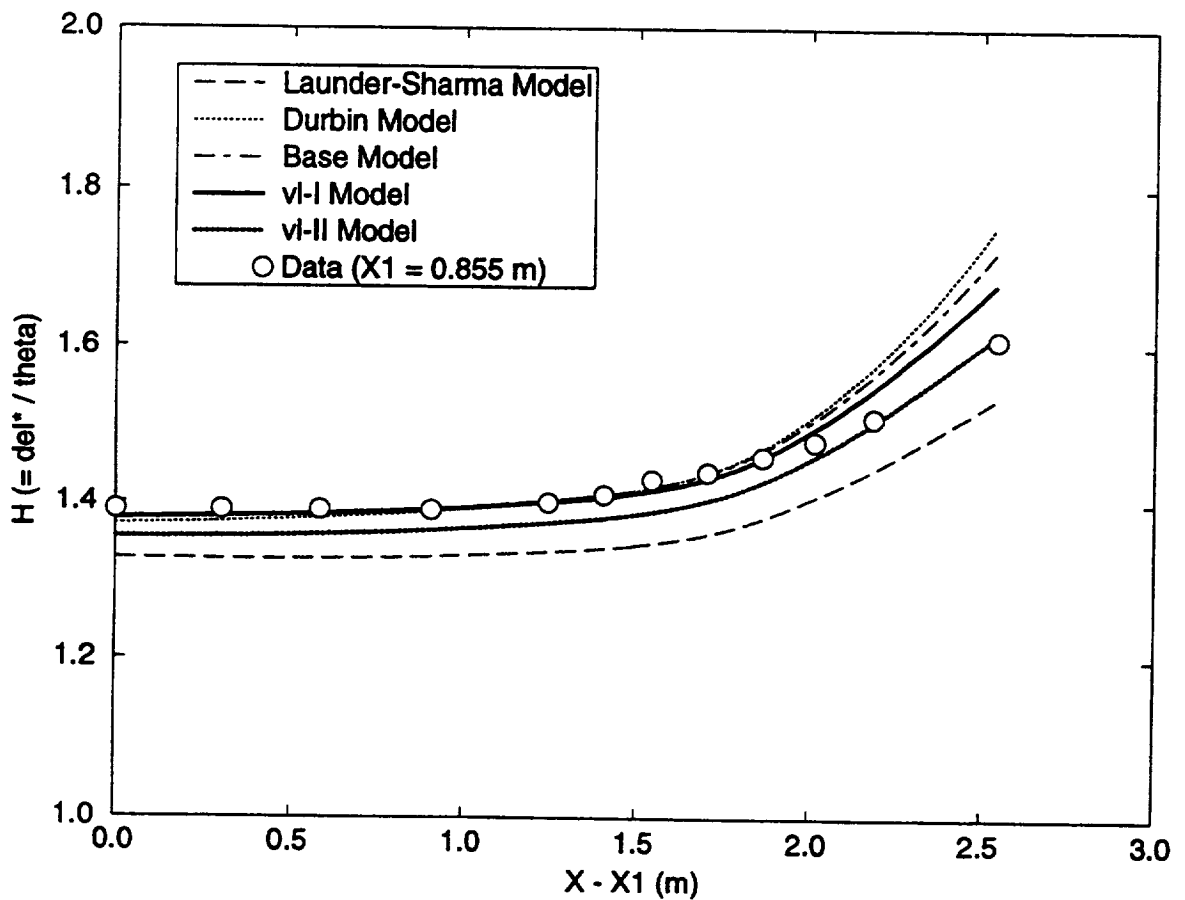


Figure 3.36 Comparison of shape parameter distributions predicted by using various k - ϵ base turbulence models with measured data for an increasingly adverse pressure gradient flow of Samuel and Joubert.

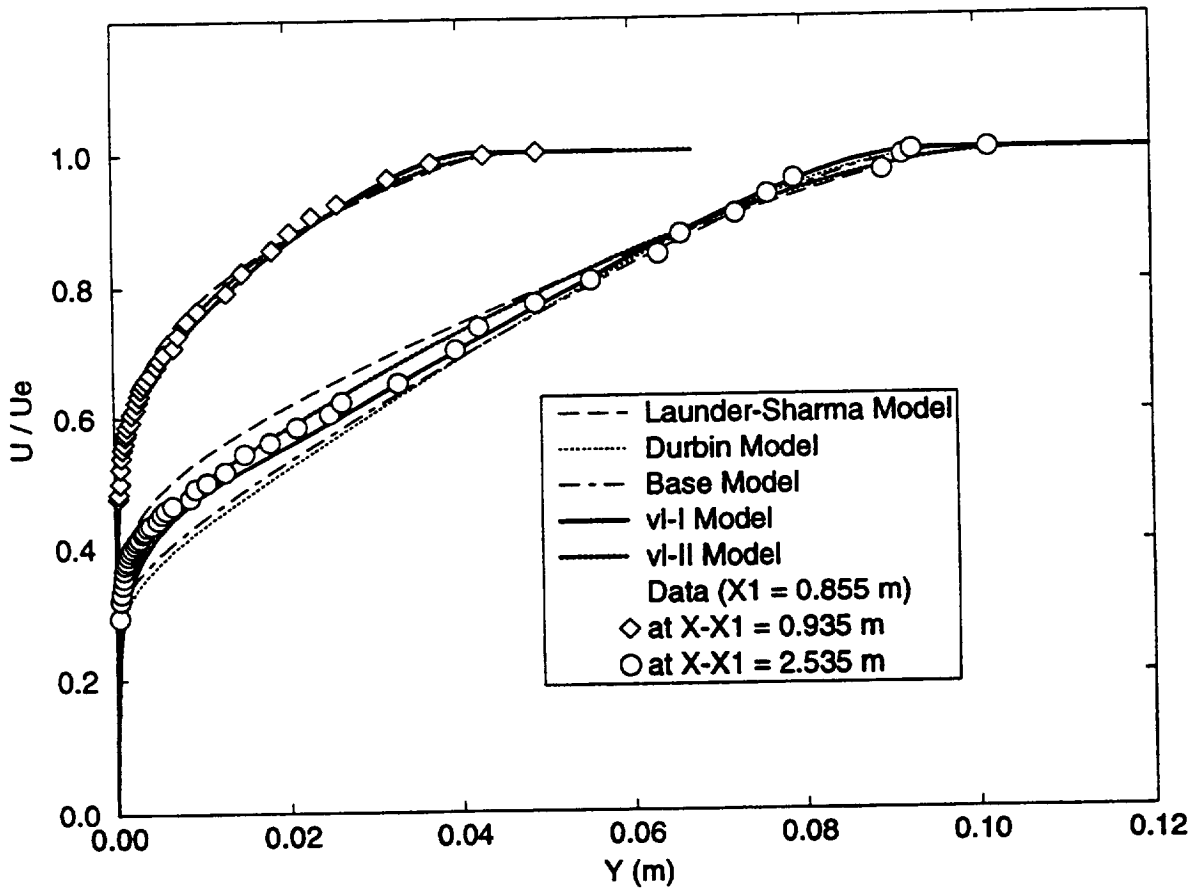


Figure 3.37 Comparison of mean velocity profiles predicted by using various k - ϵ based turbulence models with measured data for an increasingly adverse pressure gradient flow of Samuel and Joubert at $x-x_1 = 0.935$ m and 2.535 m.

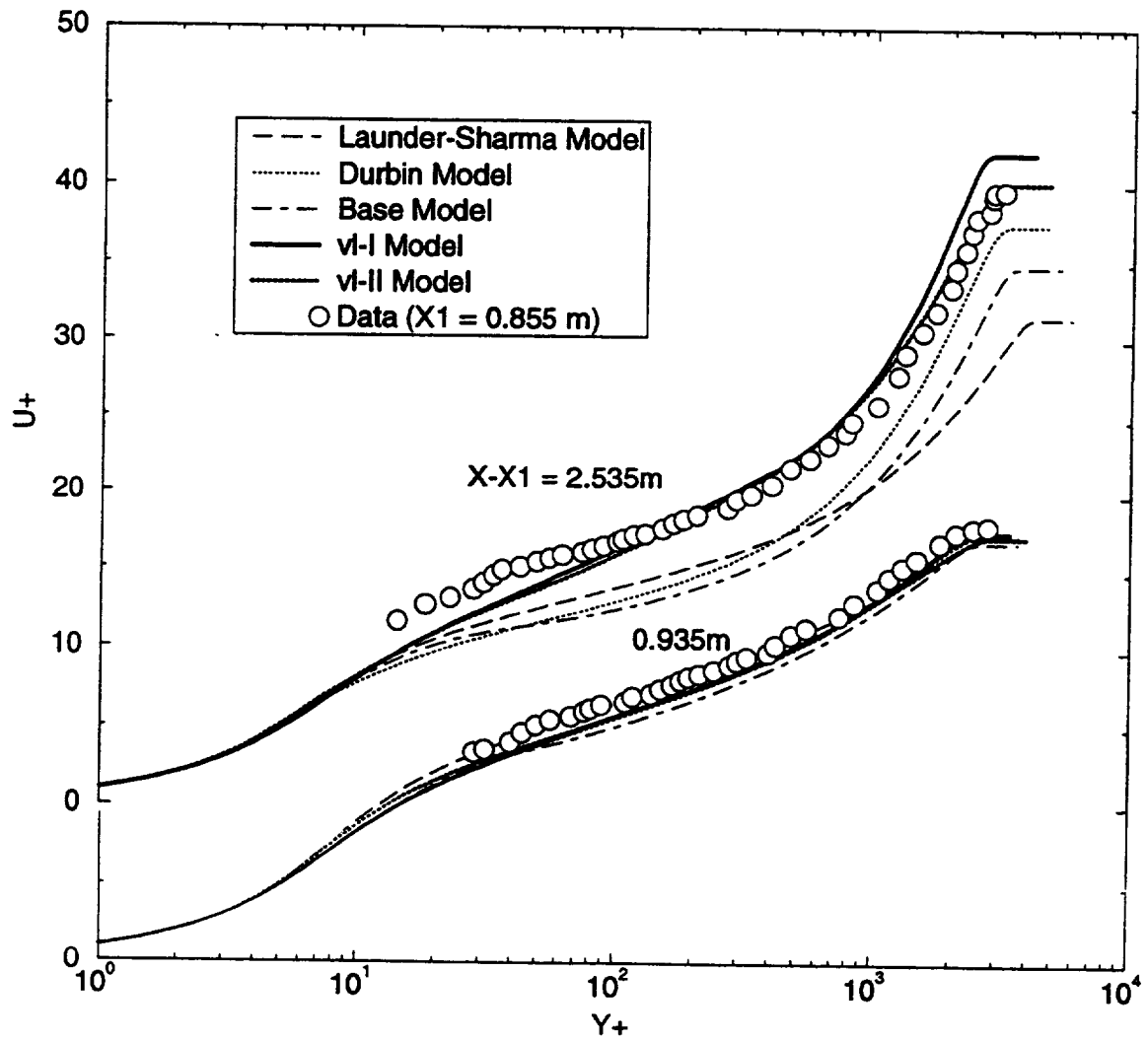


Figure 3.38 Comparison of mean velocity profiles predicted by using various k - ϵ based turbulence models with measured data for an increasingly adverse pressure gradient flow of Samuel and Joubert at $x-x_1 = 0.935\text{ m}$ and 2.535 m .

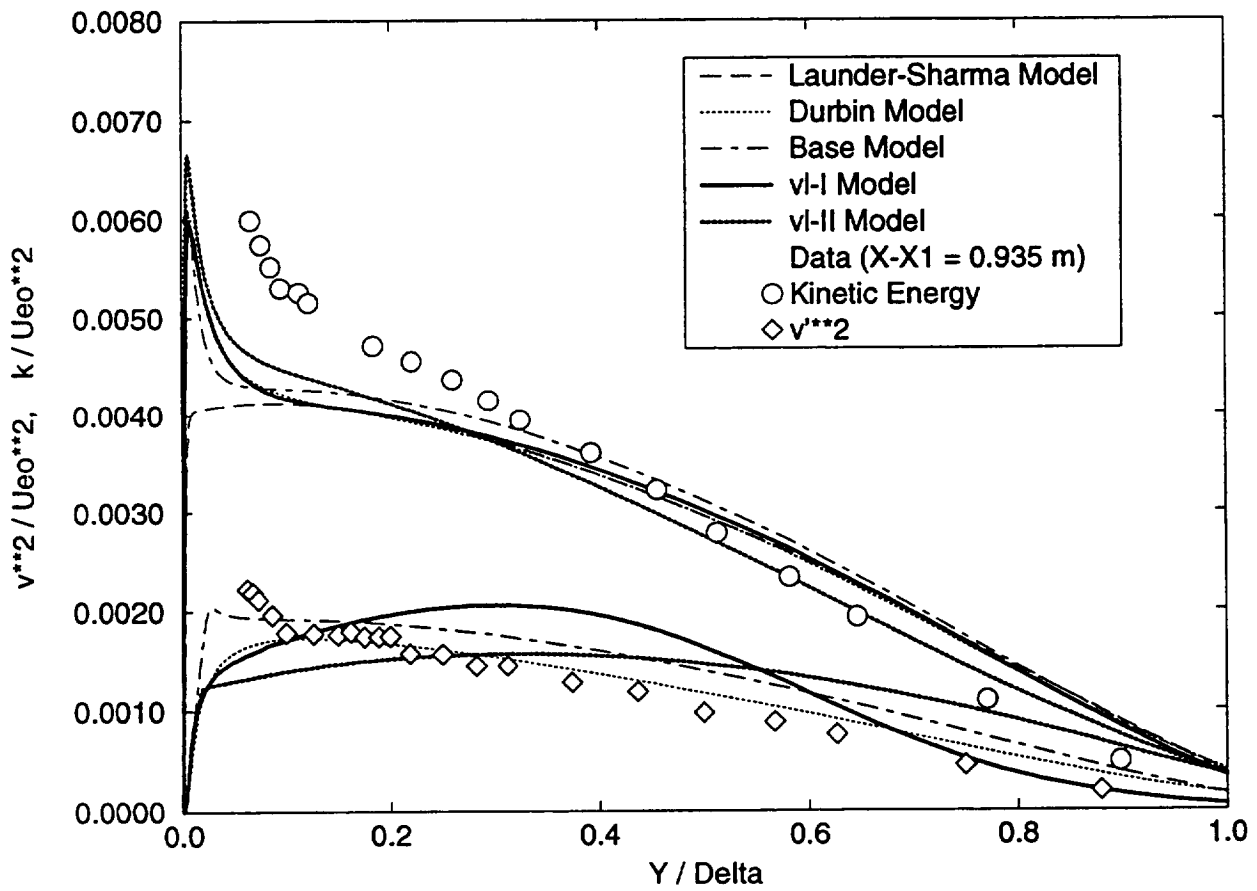


Figure 3.39 Comparison of kinetic energy and v'^2 profiles predicted by using various k - ϵ based turbulence models with measured data for an increasingly adverse pressure gradient flow of Samuel and Joubert at $x-x_1 = 0.935$ m.

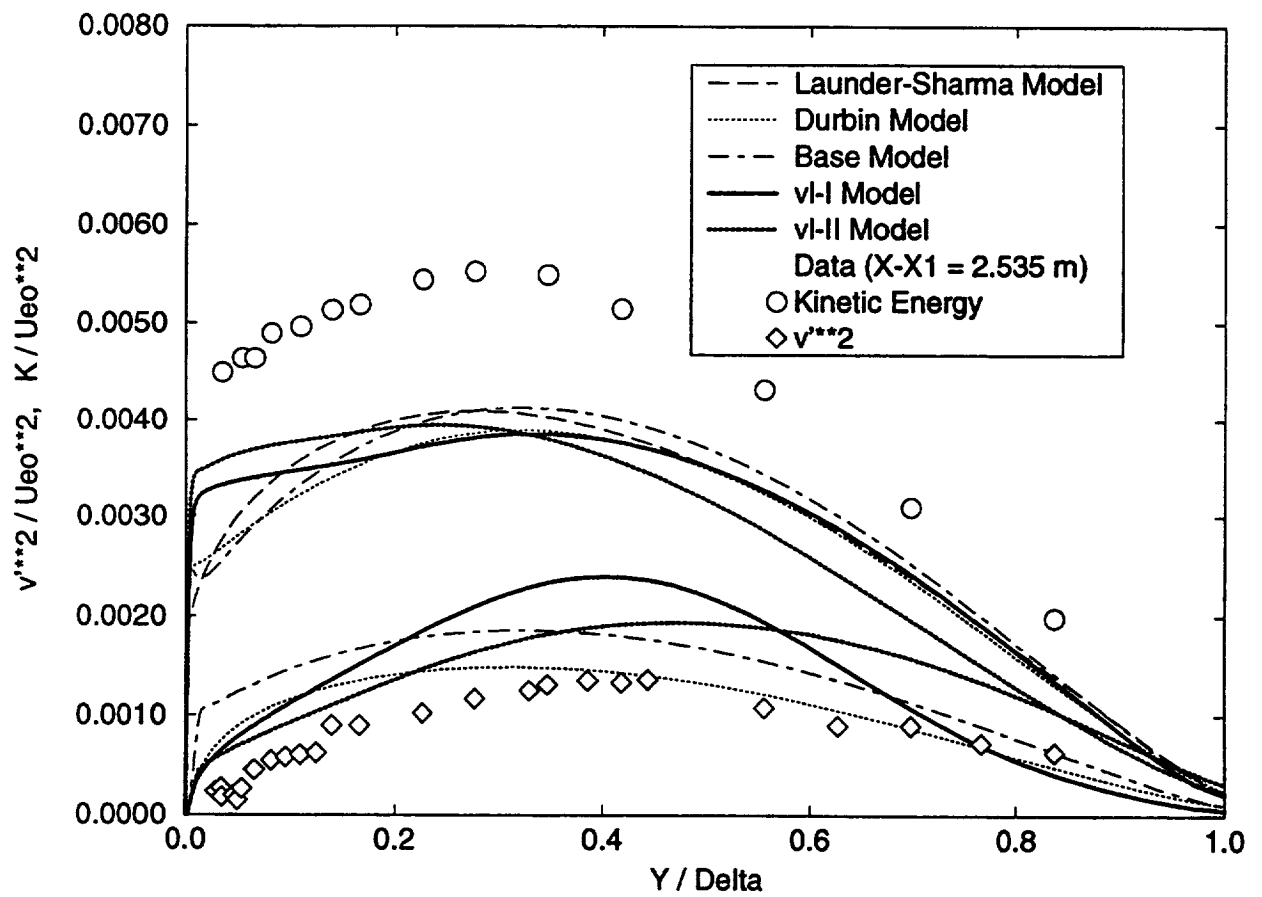


Figure 3.40 Comparison of kinetic energy and v'^2 profiles predicted by using various k - ϵ based turbulence models with measured data for an increasingly adverse pressure gradient flow of Samuel and Joubert at $x-x_1 = 2.535$ m.

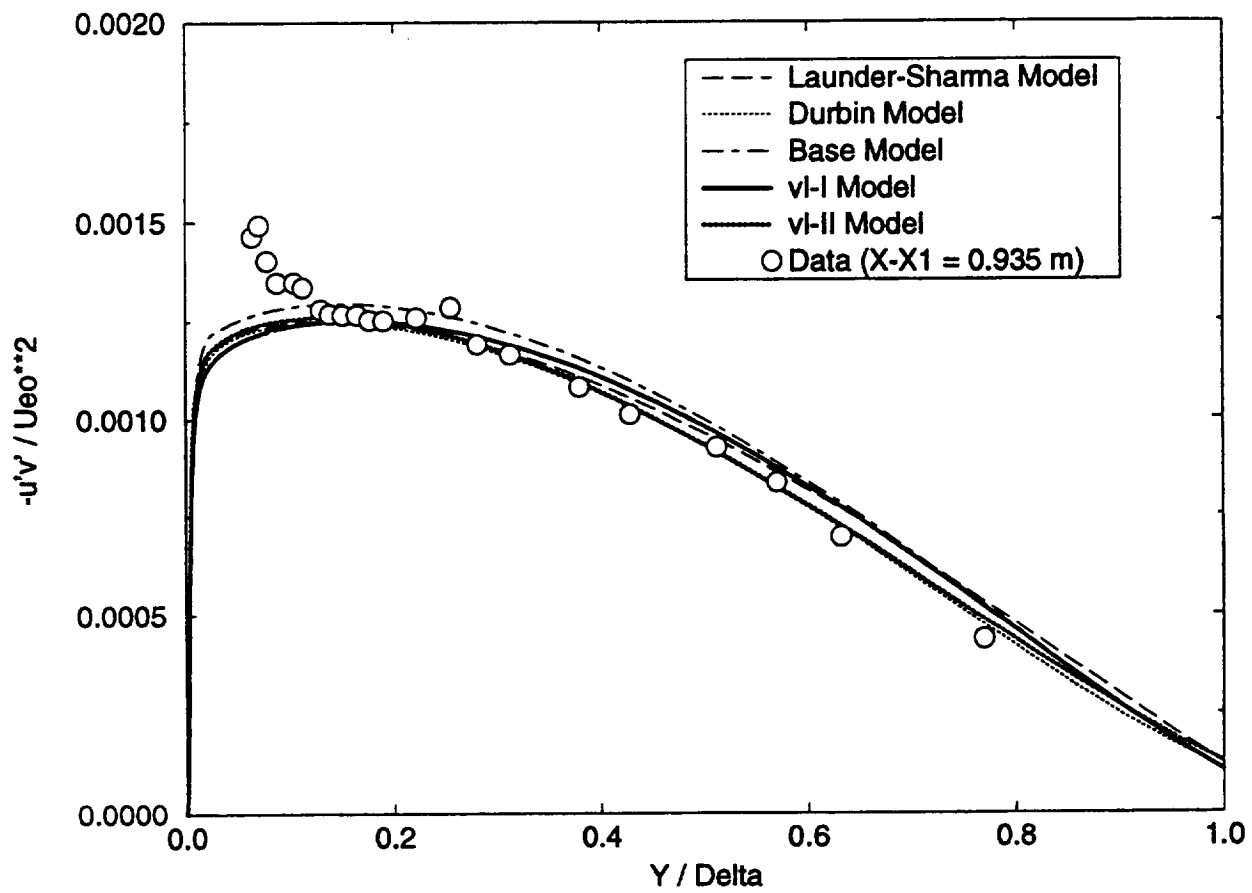


Figure 3.41 Comparison of shear stress profiles predicted by using various $k-\epsilon$ based turbulence models with measured data for an increasingly adverse pressure gradient flow of Samuel and Joubert at $x-x_1 = 0.935$ m.

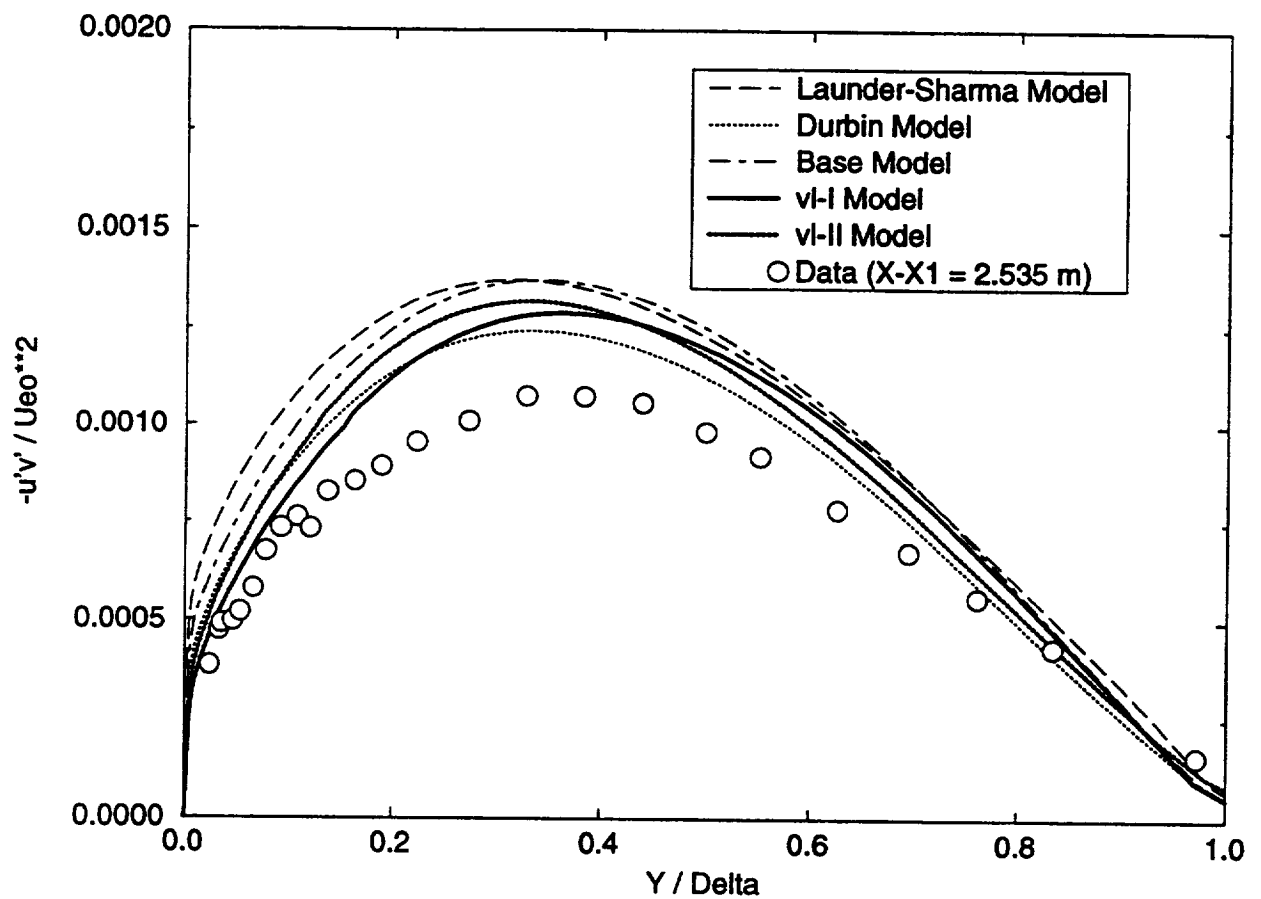


Figure 3.42 Comparison of shear stress profiles predicted by using various $k-\epsilon$ based turbulence models with measured data for an increasingly adverse pressure gradient flow of Samuel and Joubert at $x-x_1 = 2.535$ m.

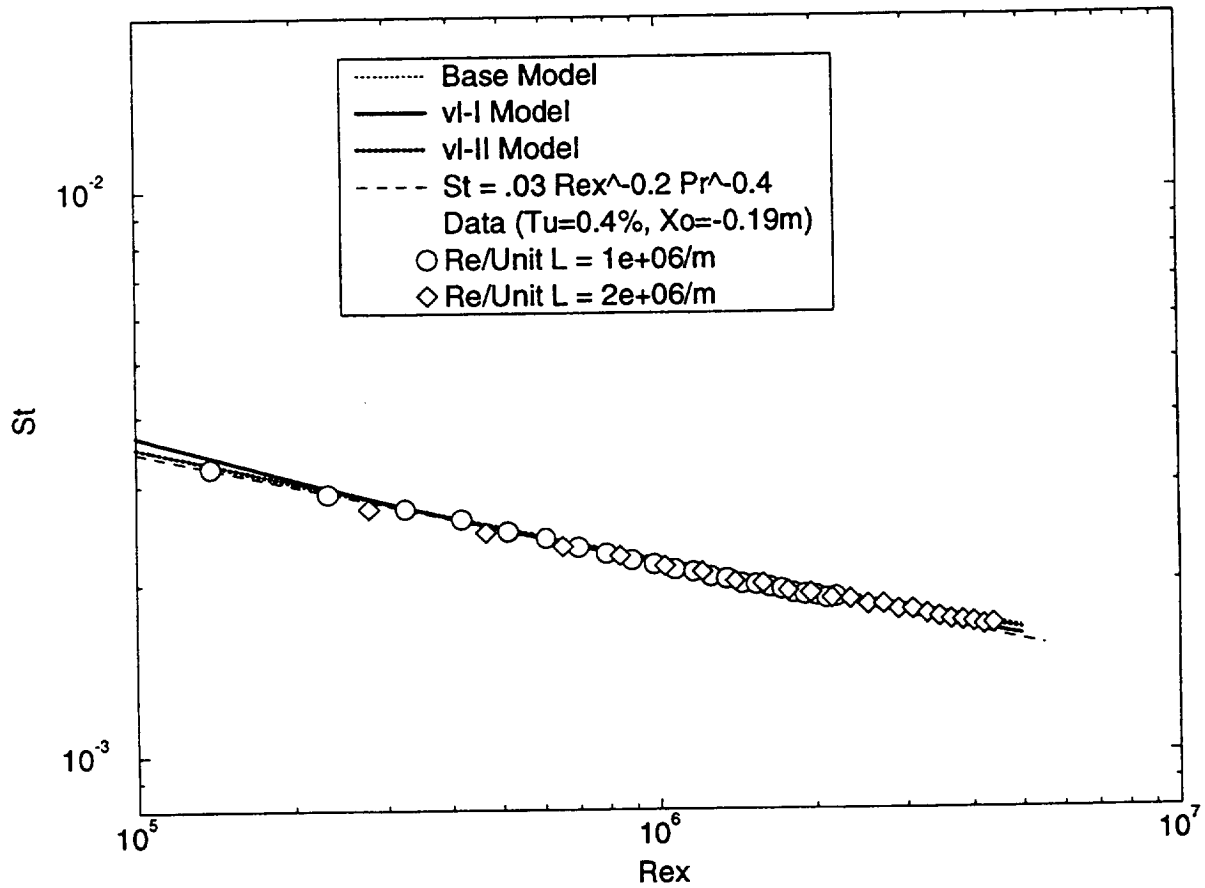


Figure 3.43 Comparison of surface heat transfer distributions calculated using the $v'l$ -I, $v'l$ -II, and base $k-\epsilon$ turbulence models with measured data for a uniformly heated flat plate ($Re_{L=1} = 1.0 \times 10^6$ and 2.0×10^6).

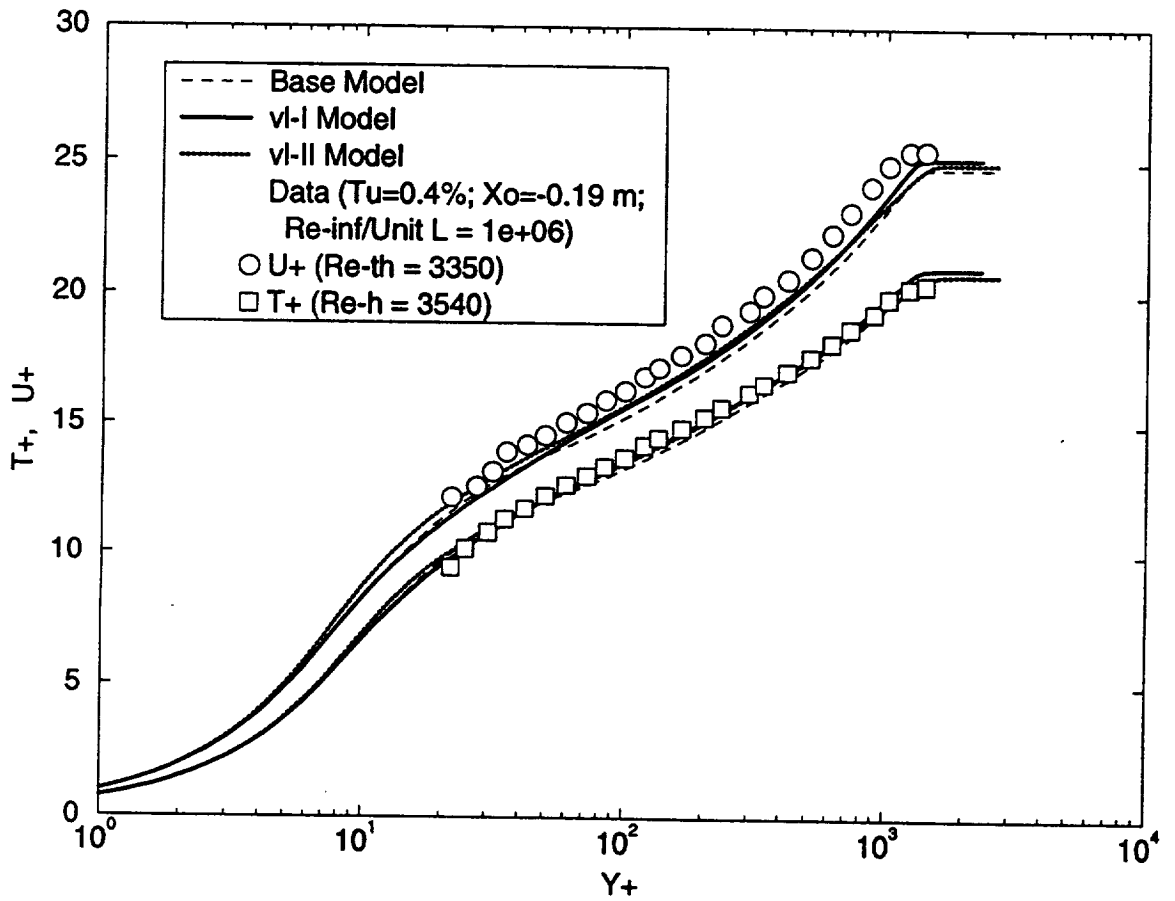


Figure 3.44 Comparison of mean velocity and temperature profiles predicted by using the $v'l$ -I, $v'l$ -II, and base k - ϵ turbulence models with measured data for a uniformly heated flat plate ($Re_{L=1} = 1.0 \times 10^6$; $Re_\theta = 3,350$; $Re_h = 3,540$).

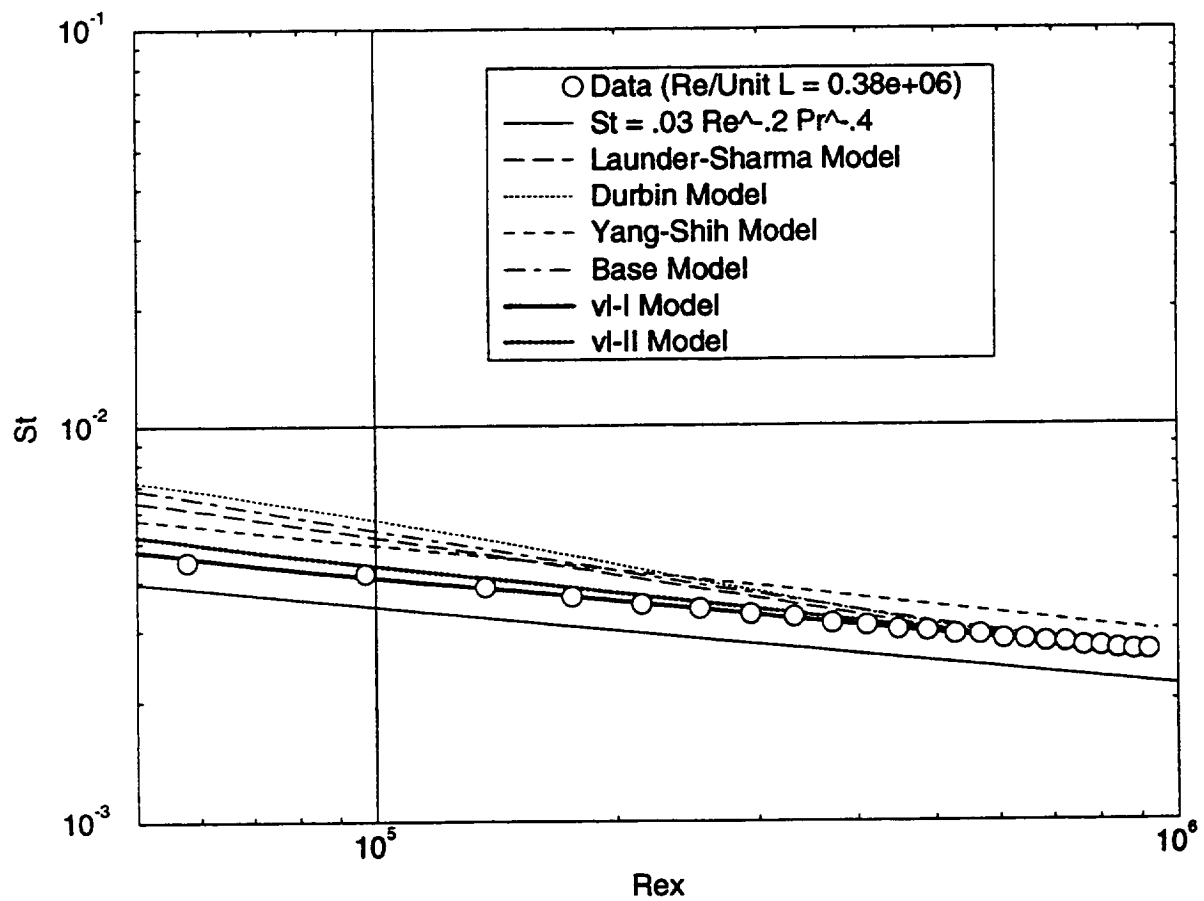


Figure 3.45 Comparison of surface heat transfer distributions calculated using various k - ϵ based turbulence models with measured data for a uniformly heated flat plate ($Re_{L=1} = 0.38 \times 10^6$; $Tu = 19\% - 7\%$).

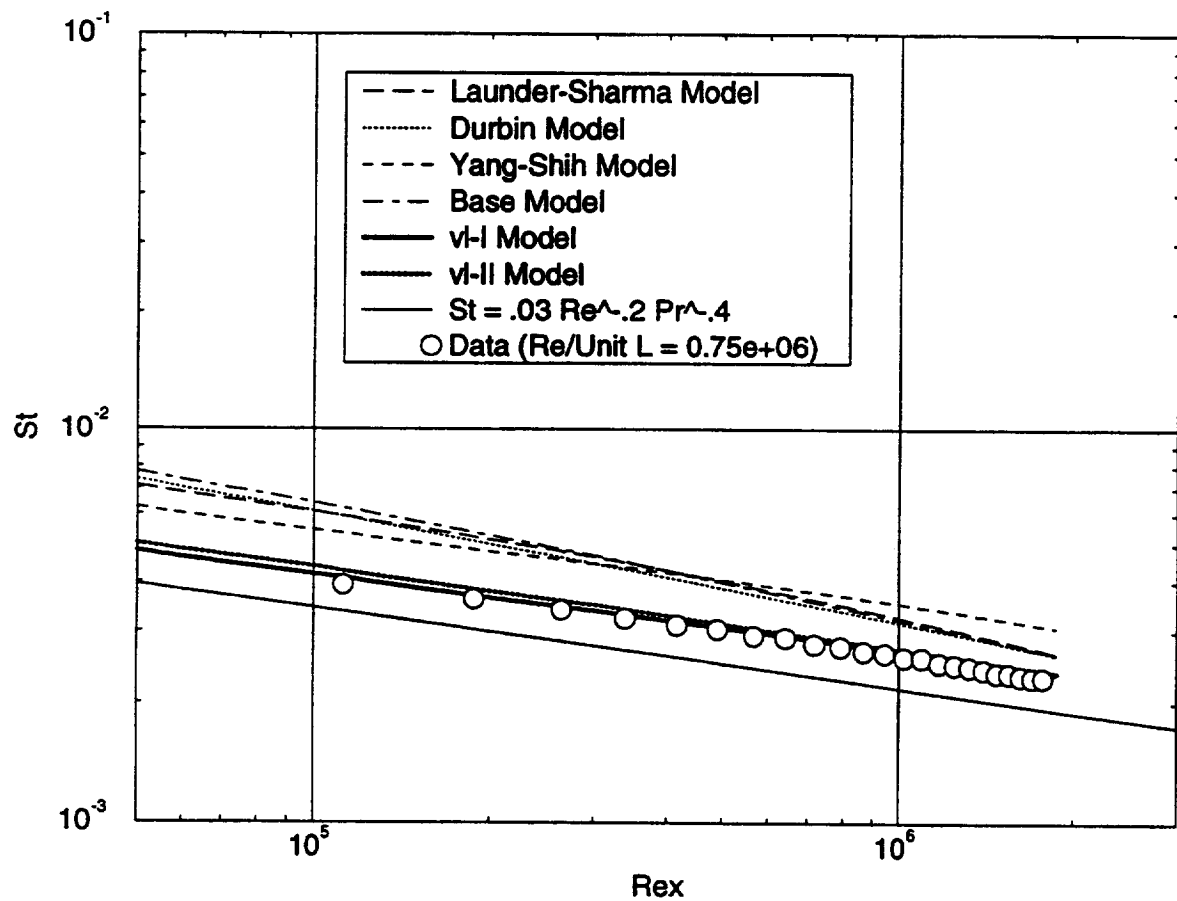


Figure 3.46 Comparison of surface heat transfer distributions calculated using various $k-\epsilon$ based turbulence models with measured data for a uniformly heated flat plate ($Re_{L=1} = 0.75 \times 10^6$; $Tu = 19\% - 7\%$).

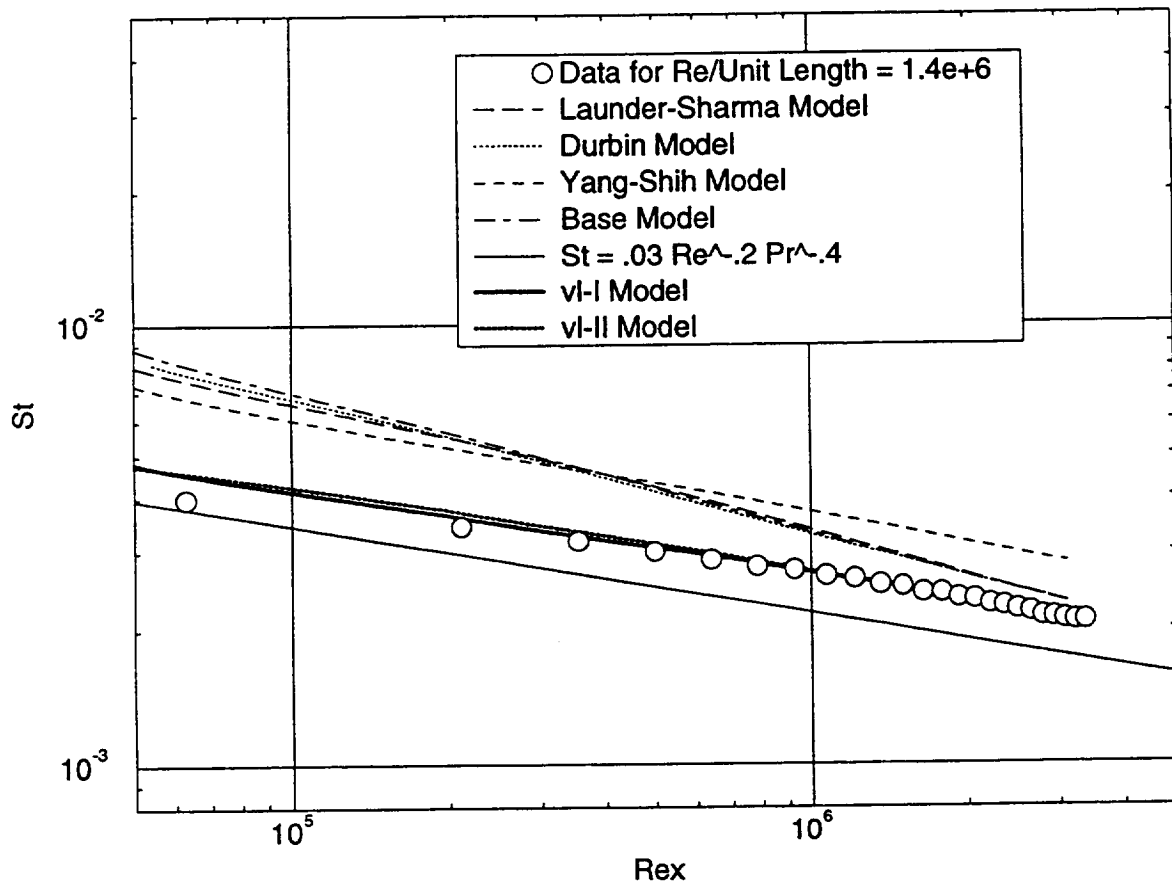


Figure 3.47 Comparison of surface heat transfer distributions calculated using various $k-\epsilon$ based turbulence models with measured data for a uniformly heated flat plate ($Re_{L=1} = 1.4 \times 10^6$; $Tu = 19\% - 7\%$).

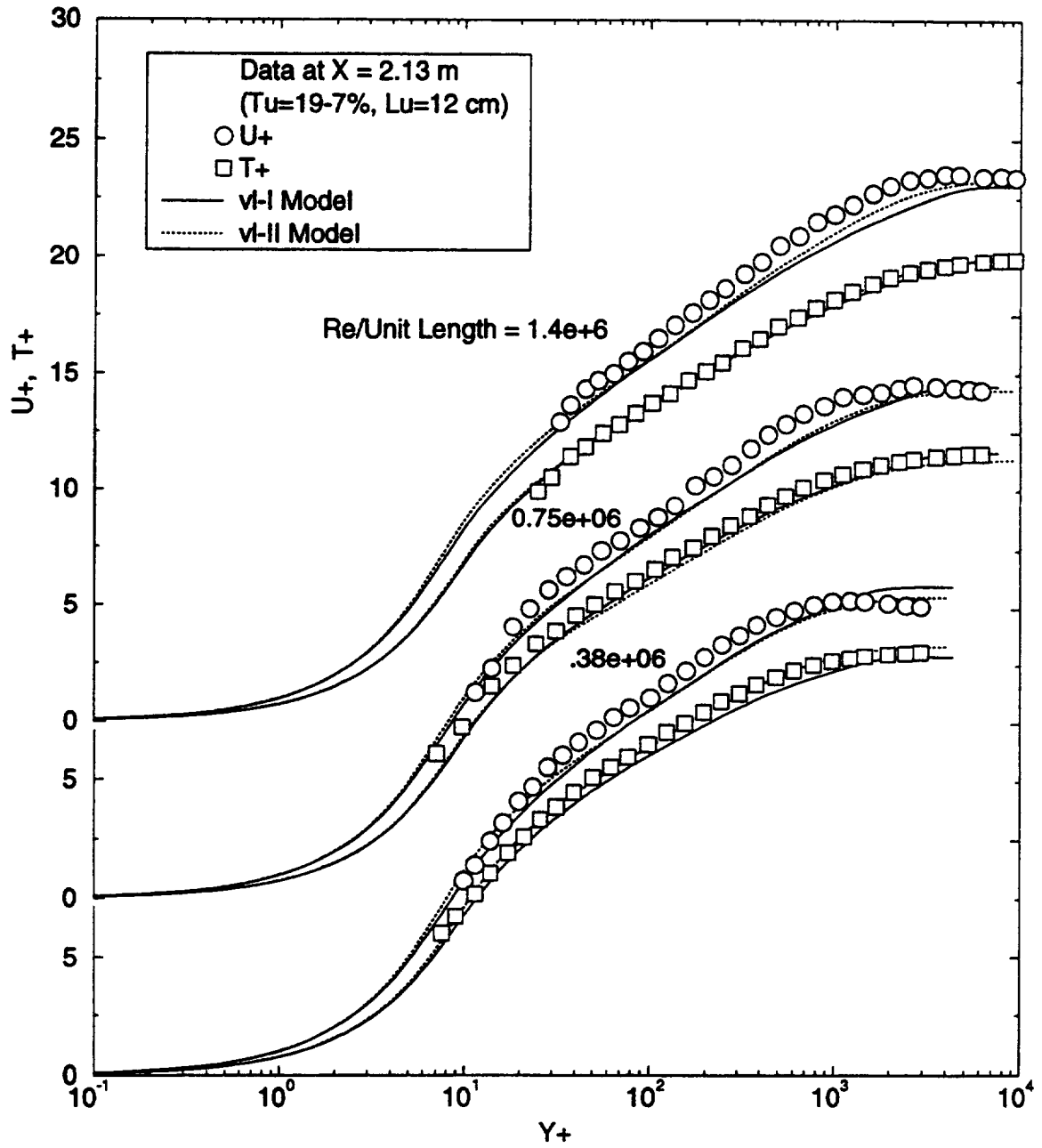


Figure 3.48 Comparison of mean velocity and temperature profiles predicted by using various $k-\epsilon$ based turbulence models with measured data for a uniformly heated flat plate ($Re_{L=1} = 0.38 \times 10^6$, 0.75×10^6 , and 1.4×10^6 ; $Tu = 19\% - 7\%$) at $x = 2.13$ m.

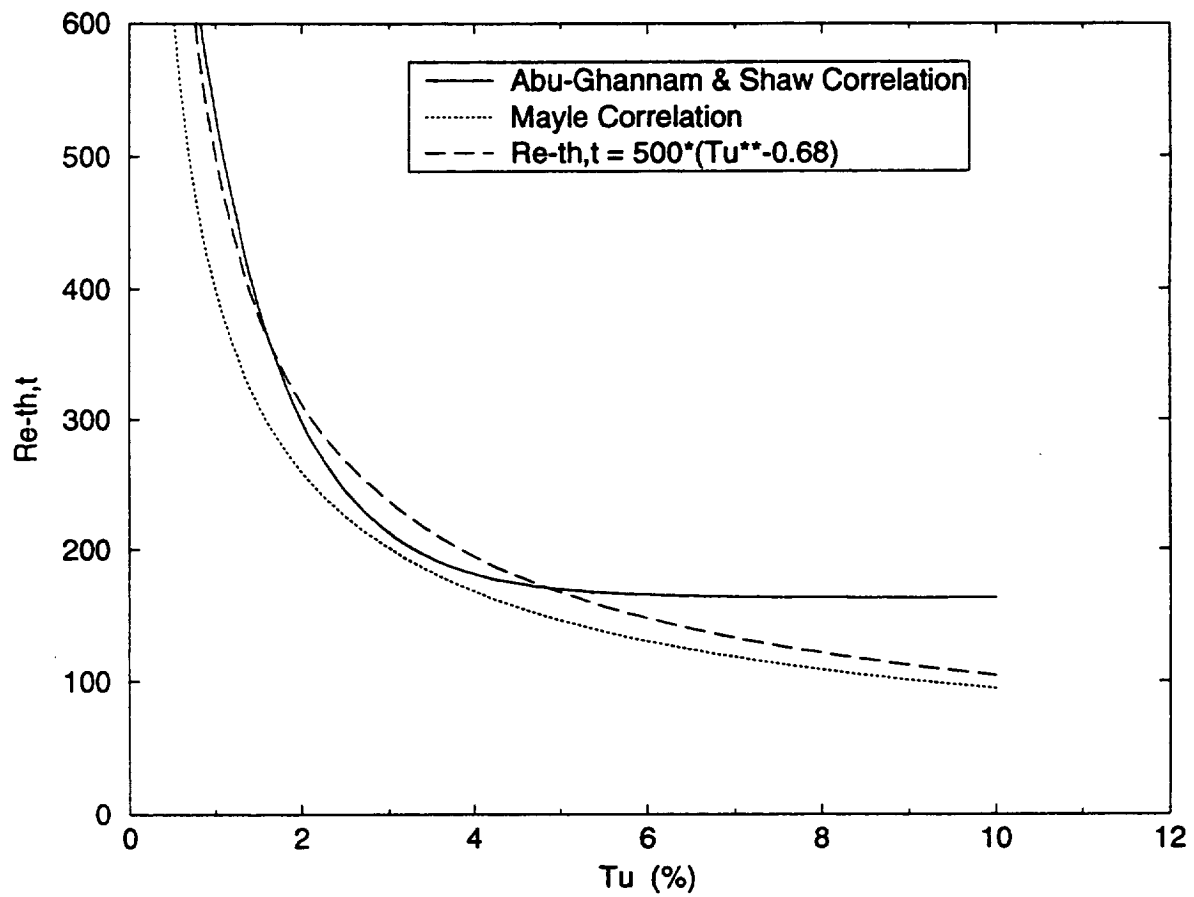


Figure 3.49 Comparison of correlations for detecting the laminar-turbulent transition onset.

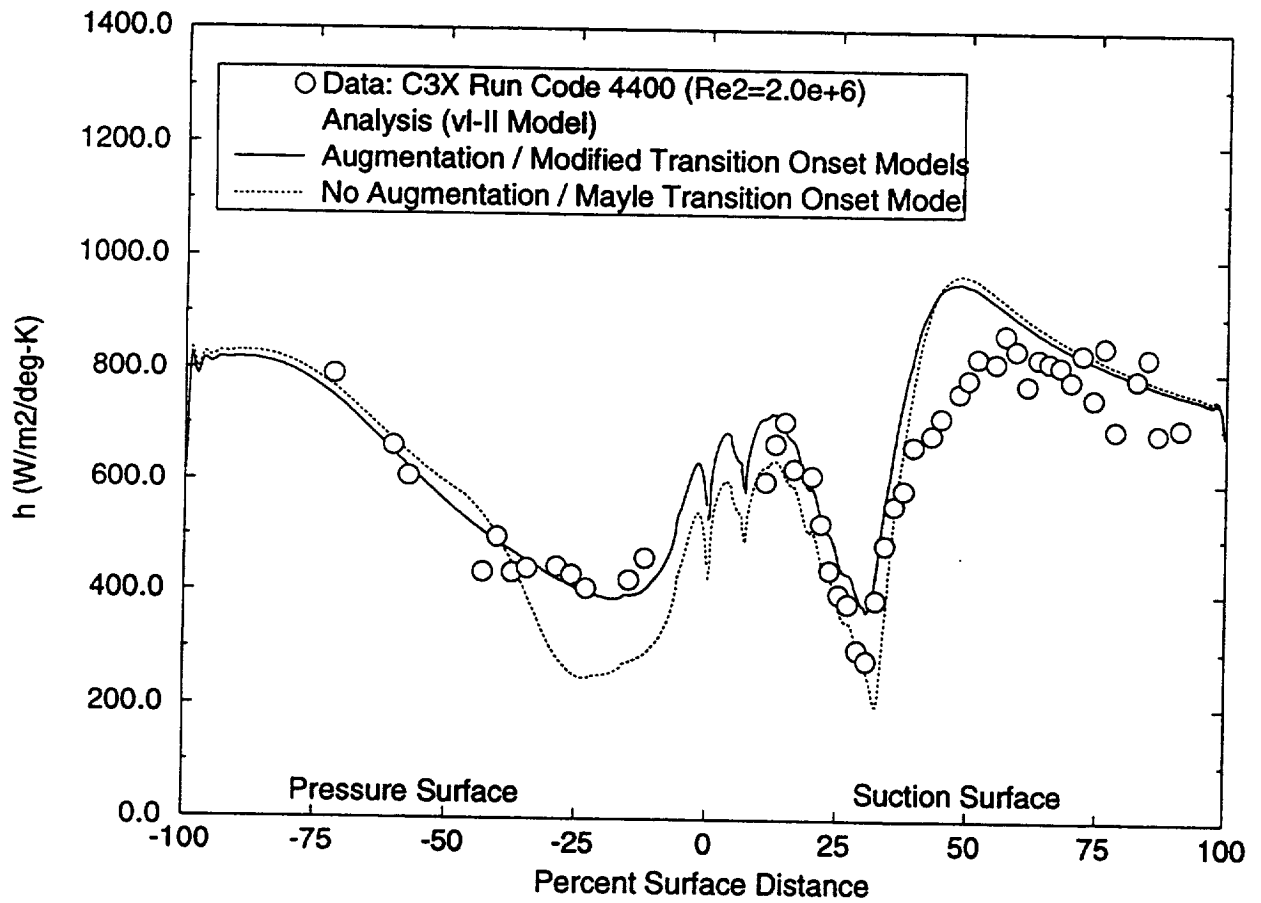


Figure 3.50 Evaluation of the laminar-turbulent transition and heat transfer augmentation models in the presence of the freestream turbulence. The data were measured by Turner, et al. from a C3X airfoil at the condition of $\text{Re}_{C2} = 2.0 \times 10^6$, $M_1 = 0.16$, $M_2 = 0.9$, and $Tu = 6.55\%$.

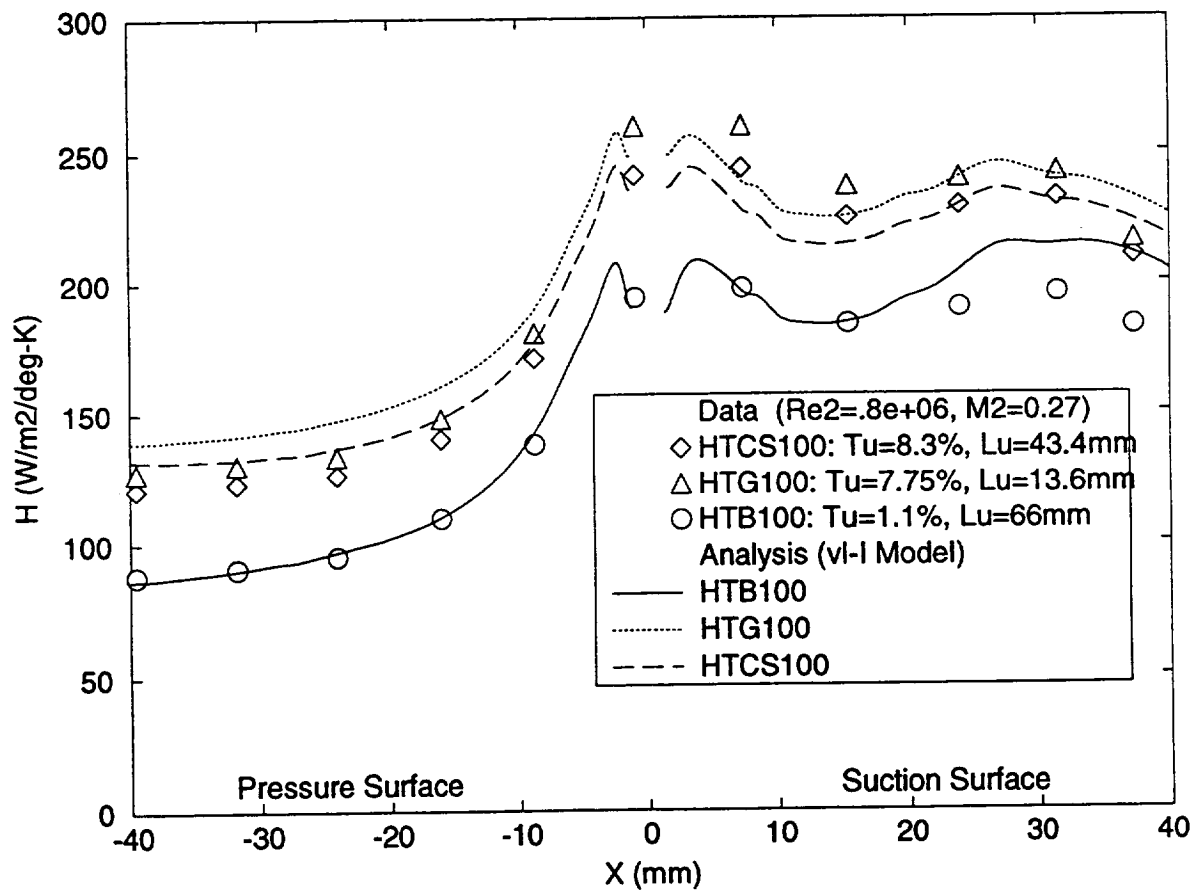


Figure 3.51 Evaluation of the heat transfer augmentation model in the presence of the freestream turbulence. The data were measured by Ames from a C3X airfoil at the condition of $Re_{C2} = 0.8 \times 10^6$, $M_1 = 0.08$, $M_2 = 0.27$, $Tu = 1\% - 8\%$, and $Lu = 1.3 \text{ cm} - 6.6 \text{ cm}$.

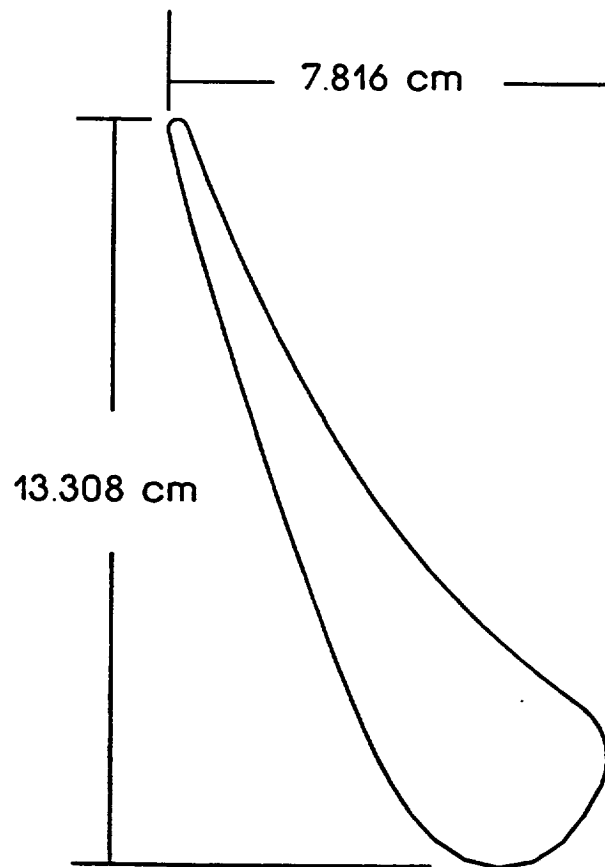


Figure 3.52 C3X vane geometry as setup in cascade (Ames' measurements).

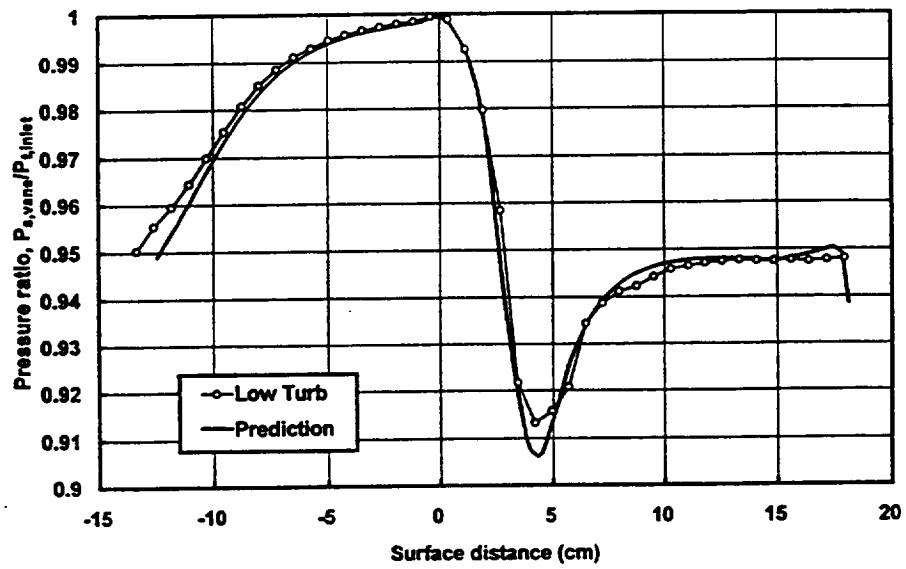


Figure 3.53 Comparison of airfoil surface pressures computed using a stream function analysis with measured data for a C3X vane at $M_2 = 0.27$.

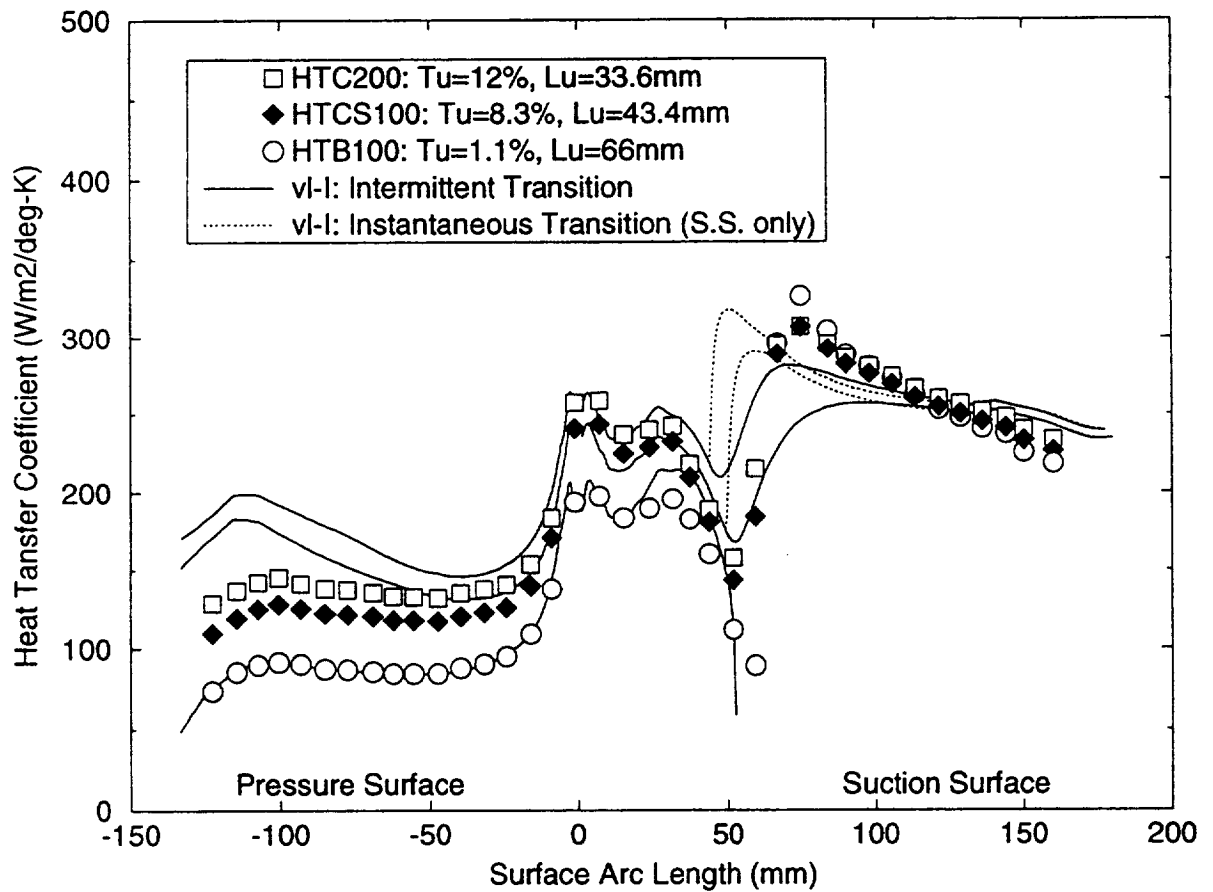


Figure 3.54 Comparison of measured and computed surface heat transfer distributions for a C3X vane at $Re_{C2} = 0.8 \times 10^6$, $M_1 = 0.08$, $M_2 = 0.27$, and $Tu = 1\% - 12\%$. The computed data were obtained by using the $v'l$ -I model.

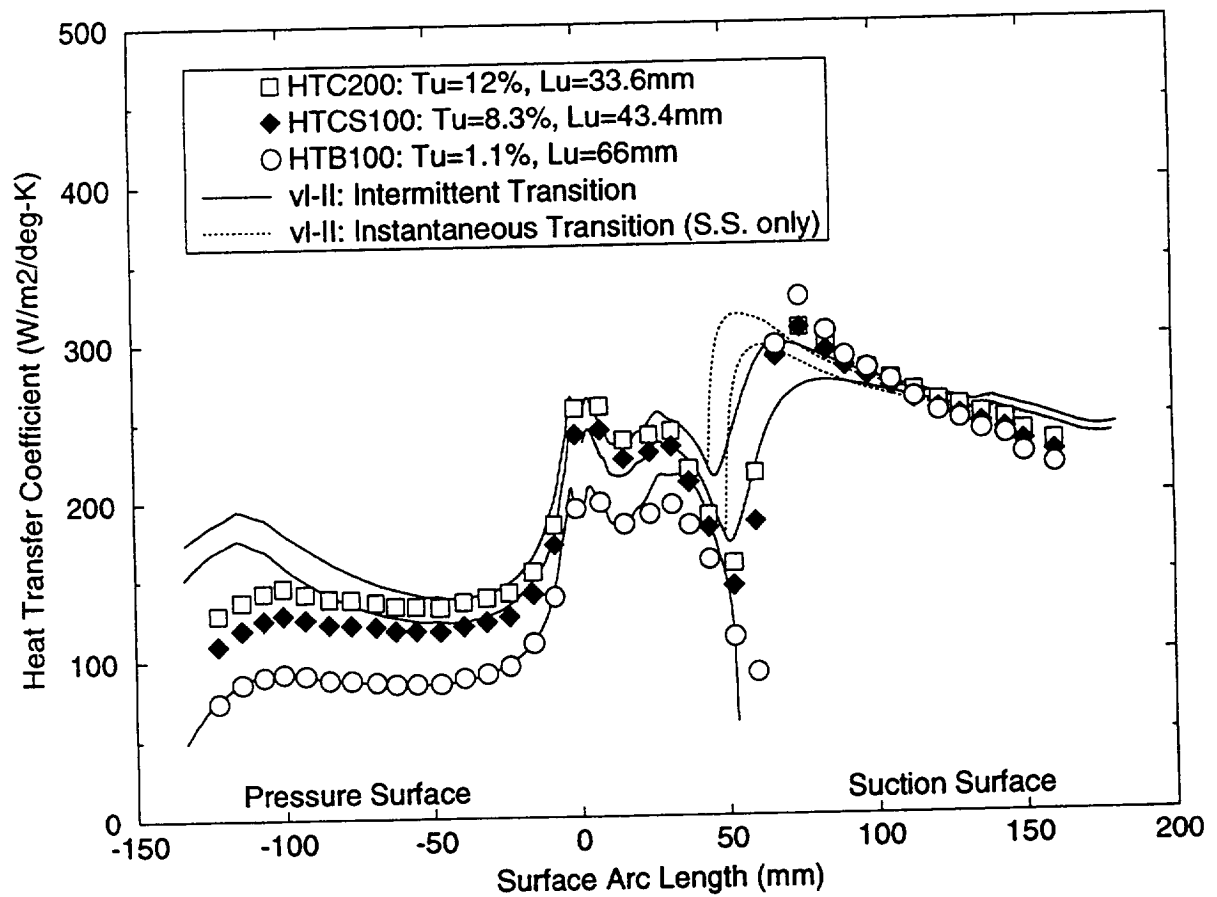


Figure 3.55 Comparison of measured and computed surface heat transfer distributions for a C3X vane at $Re_{C2} = 0.8 \times 10^6$, $M_1 = 0.08$, $M_2 = 0.27$, and $Tu = 1\% - 12\%$. The computed data were obtained by using the $v'l-II$ model.

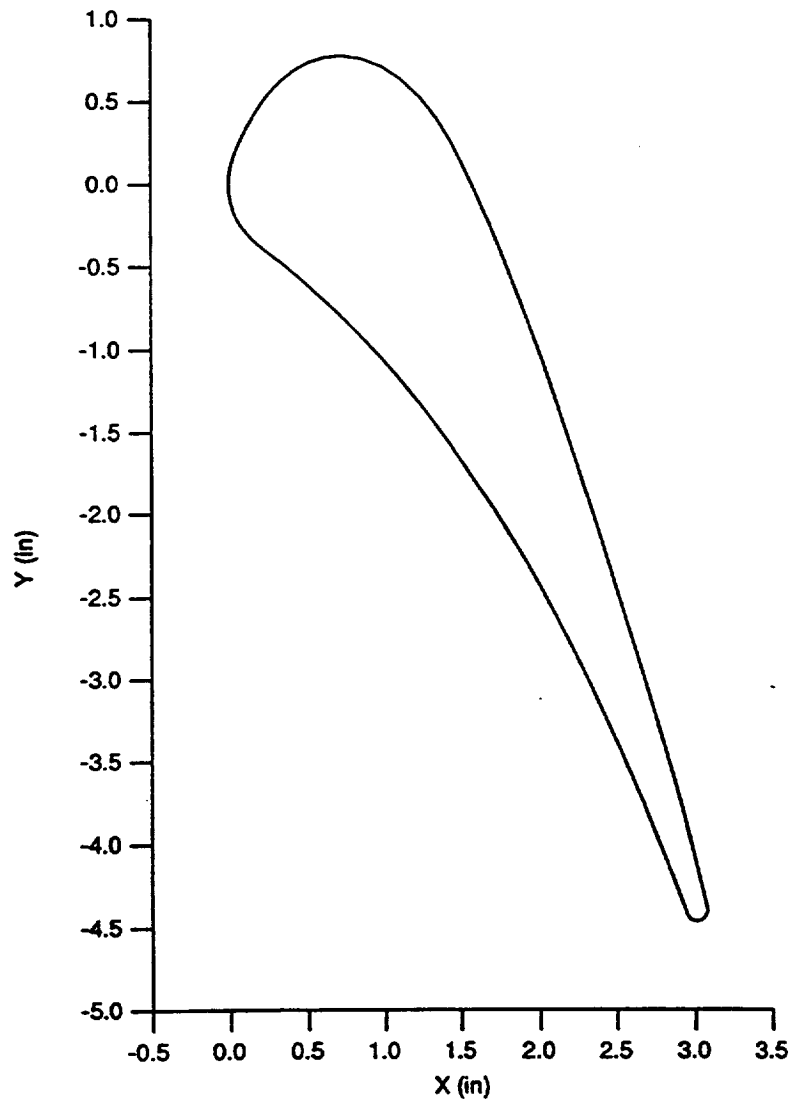


Figure 3.56 C3X vane geometry as setup in cascade (Turner, et al. measurements).

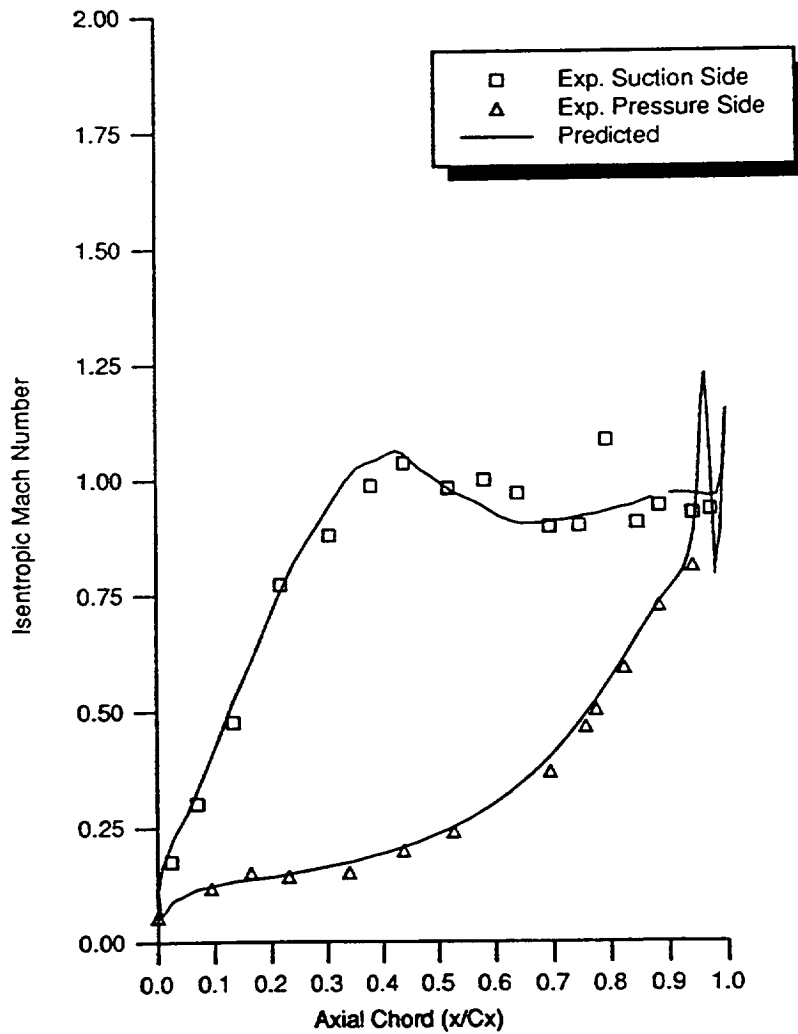


Figure 3.57 Comparison of airfoil surface velocities computed using an Euler analysis with measured data for a C3X vane at $M_2 = 0.9$, $Re_{C2} = 2.0 \times 10^6$.

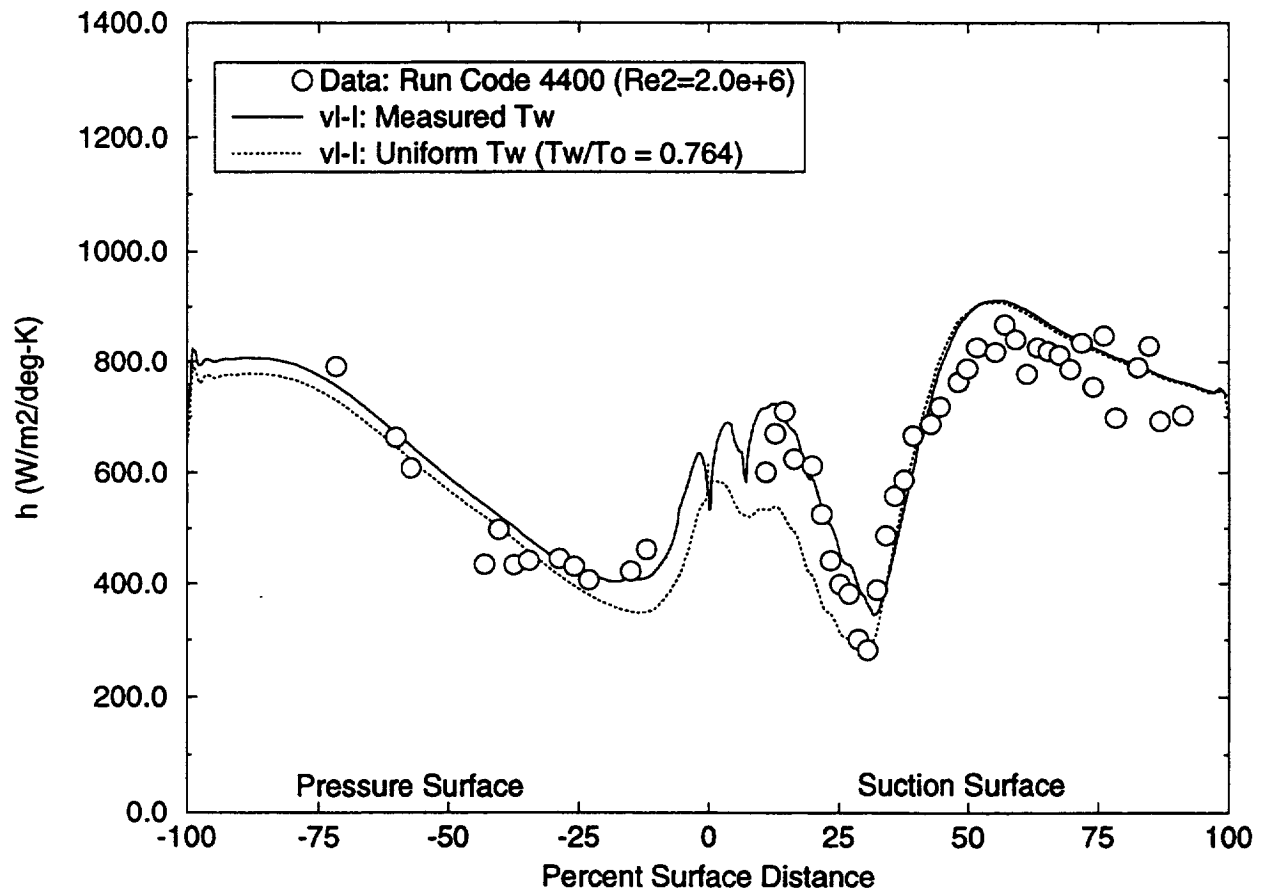


Figure 3.58 Comparison of C3X airfoil surface heat transfer coefficients computed with measured surface temperatures and uniform surface temperatures at $Re_{C2} = 2.0 \times 10^6$, $M_1 = 0.16$, $M_2 = 0.9$, and $T_u = 6.55\%$. The computed data were obtained by using the v'l-I model.

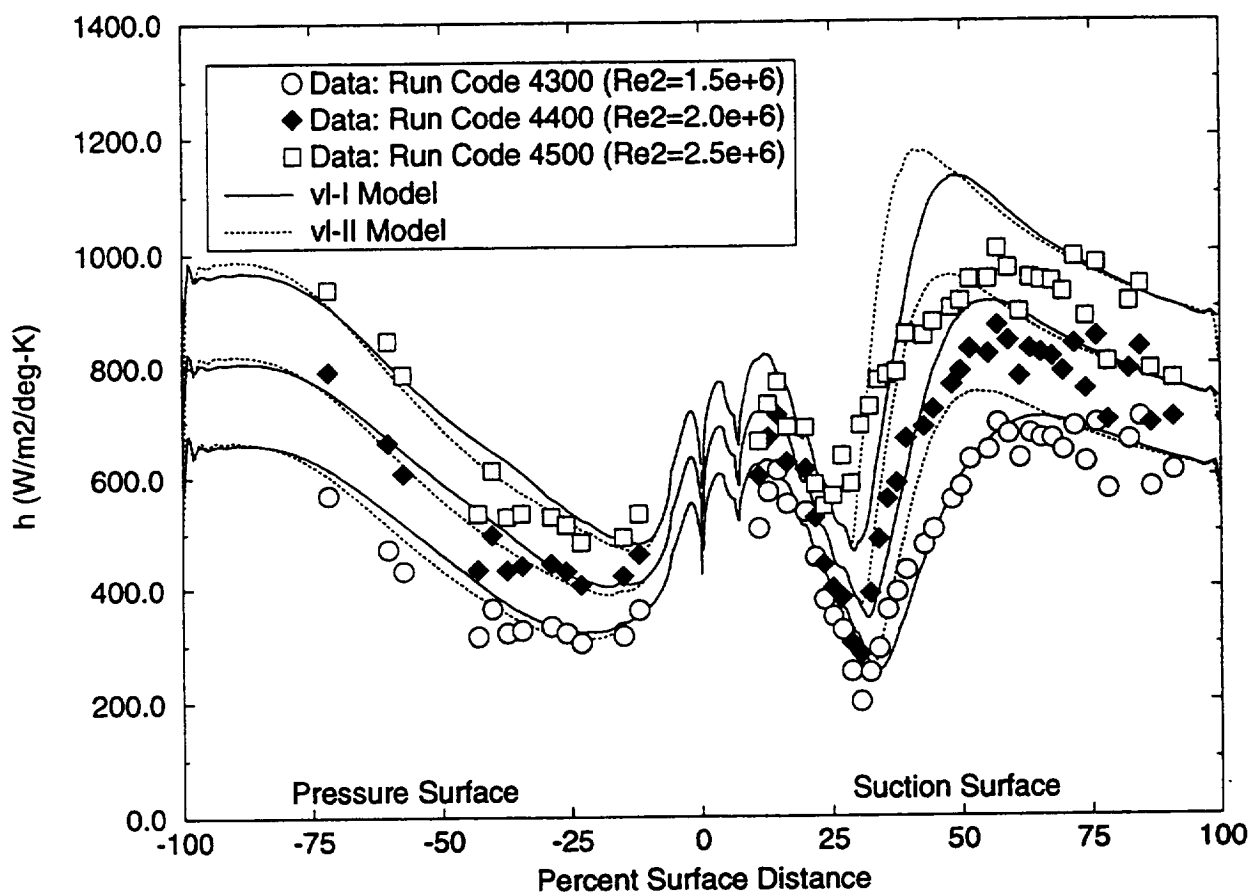


Figure 3.59 Comparison of computed C3X airfoil surface heat transfer coefficients with measured data at $Re_{C2} = 1.5 \times 10^6$, 2.0×10^6 , and 2.6×10^6 ; $M_1 = 0.16$; $M_2 = 0.9$; and $Tu = 6.55\%$.

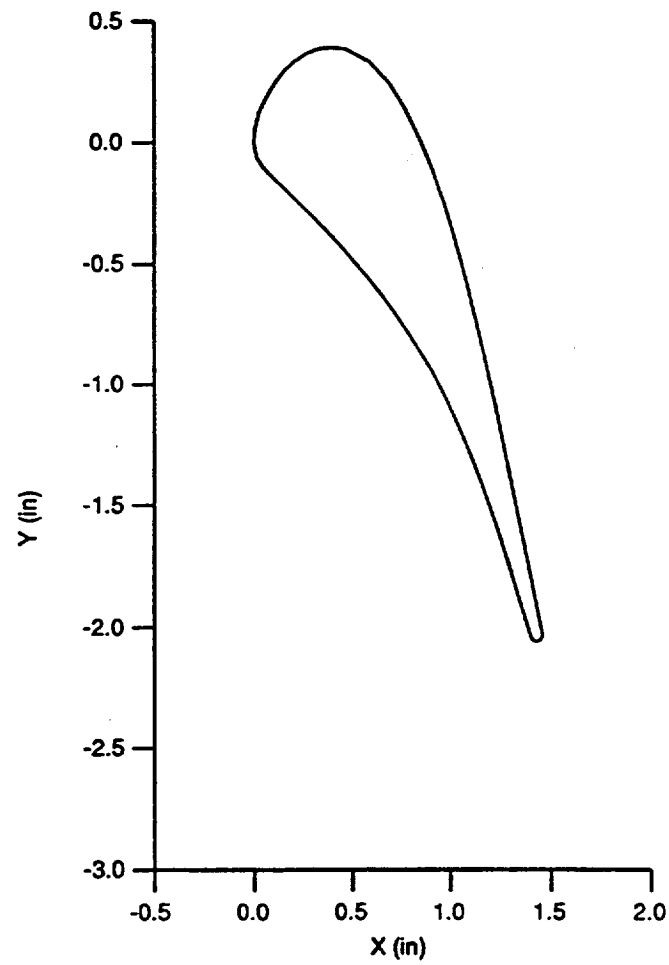


Figure 3.60 VKI vane geometry as setup in cascade (Arts, et al. measurements).

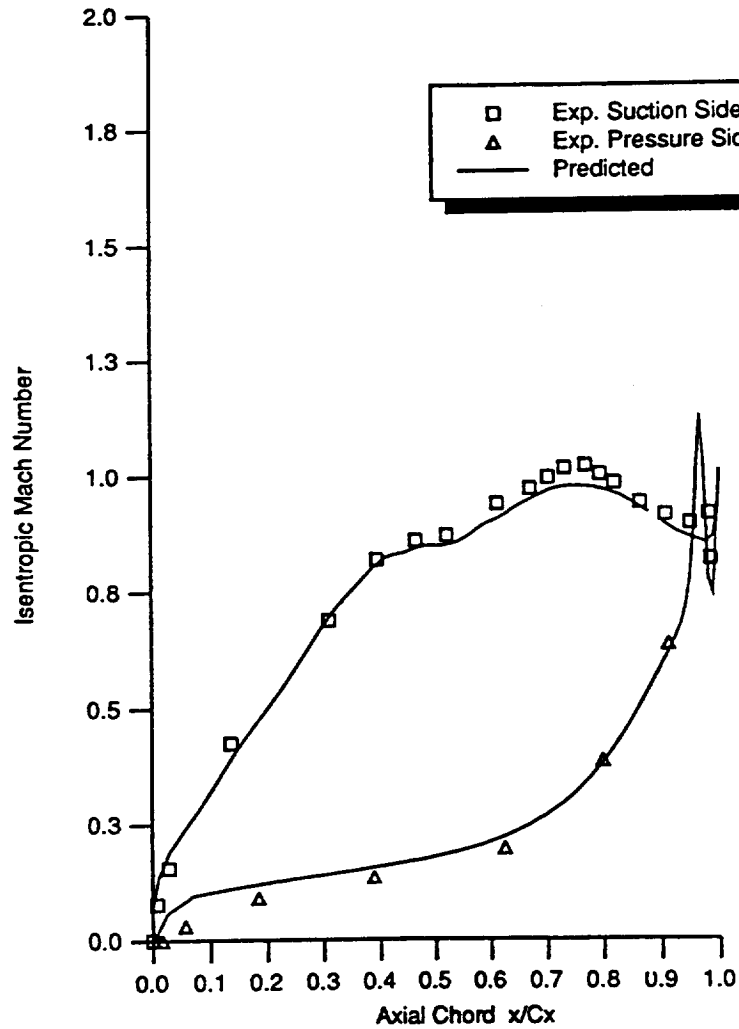


Figure 3.61 Comparison of airfoil surface velocities computed using an Euler analysis with measured data for a VKI vane at $M_2 = 0.9$, $Re_{C2} = 1.0 \times 10^6$.

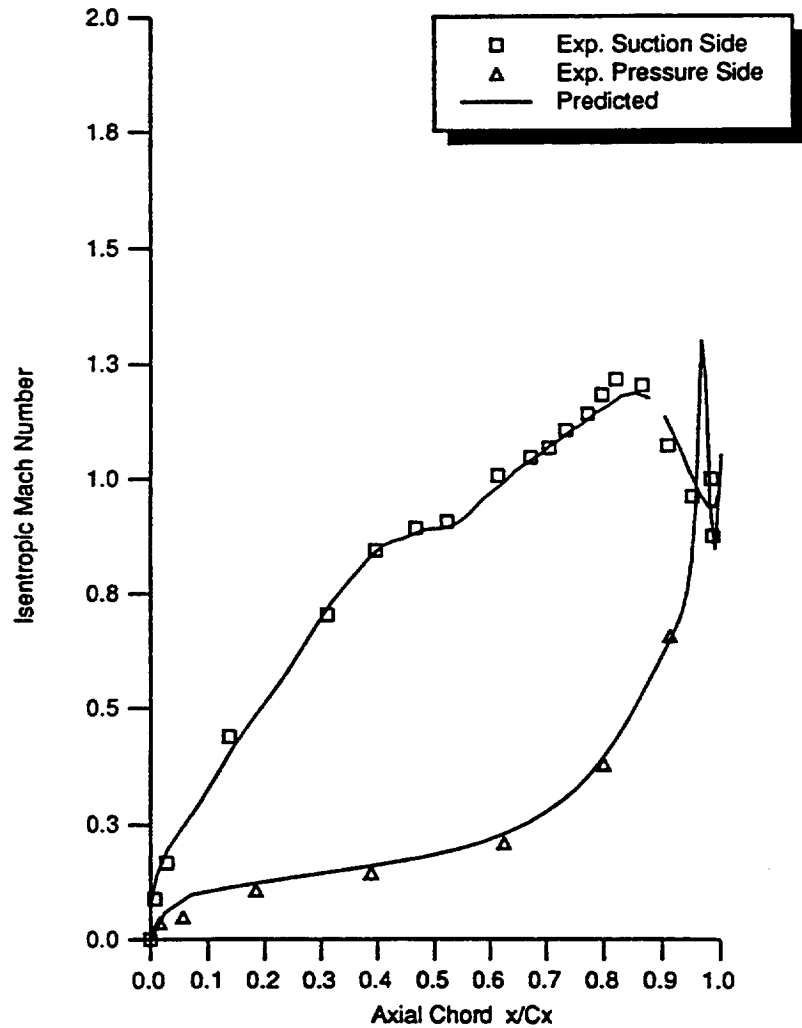


Figure 3.62 Comparison of airfoil surface velocities computed using an Euler analysis with measured data for a VKI vane at $M_2 = 1.02$, $Re_{C2} = 1.0 \times 10^6$.

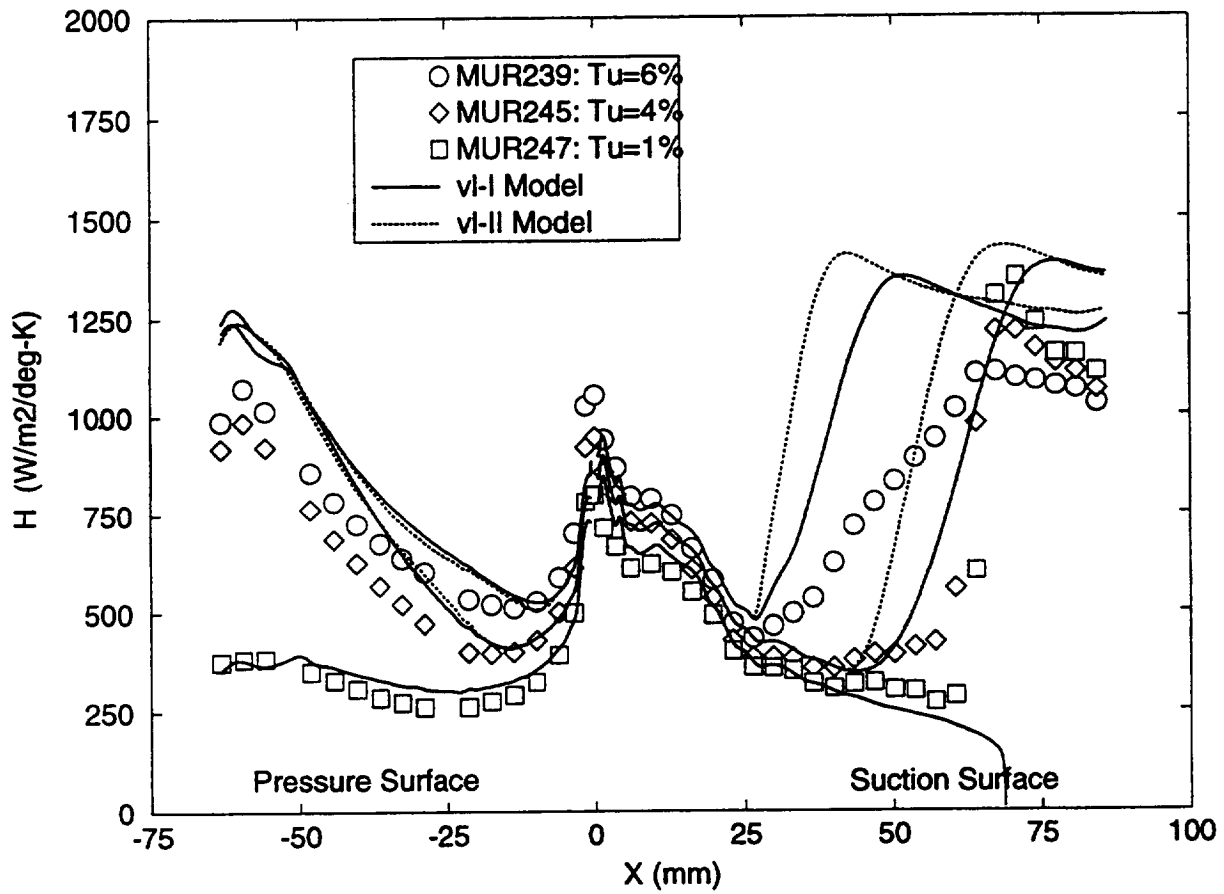


Figure 3.63 Comparison of computed VKI airfoil surface heat transfer coefficients with measured data at $Re_{C2} = 2.0 \times 10^6$, $M_2 = 0.9$, and $Tu = 1\% - 6\%$.

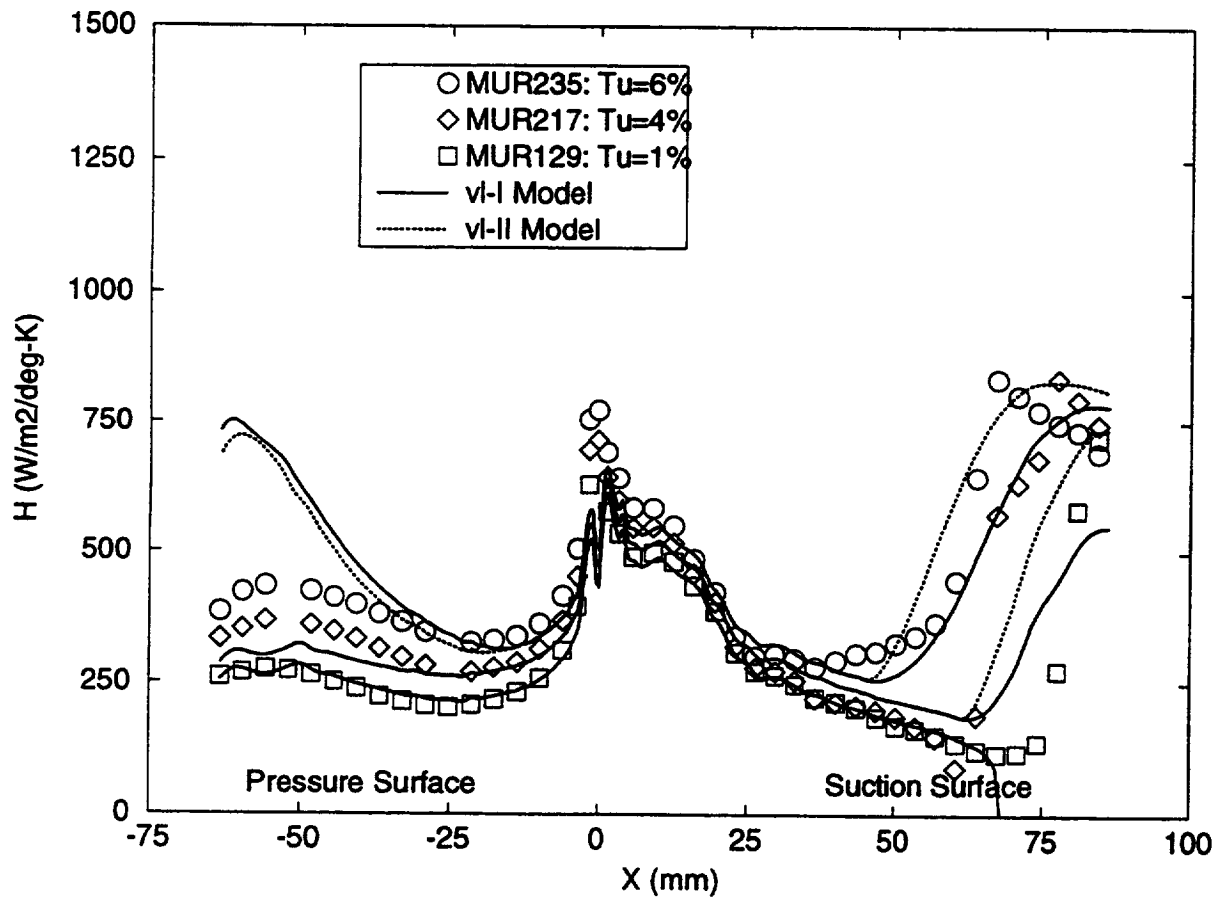


Figure 3.64 Comparison of computed VKI airfoil surface heat transfer coefficients with measured data at $Re_{C2} = 1.0 \times 10^6$, $M_2 = 0.9$, and $T_u = 1\% - 6\%$.

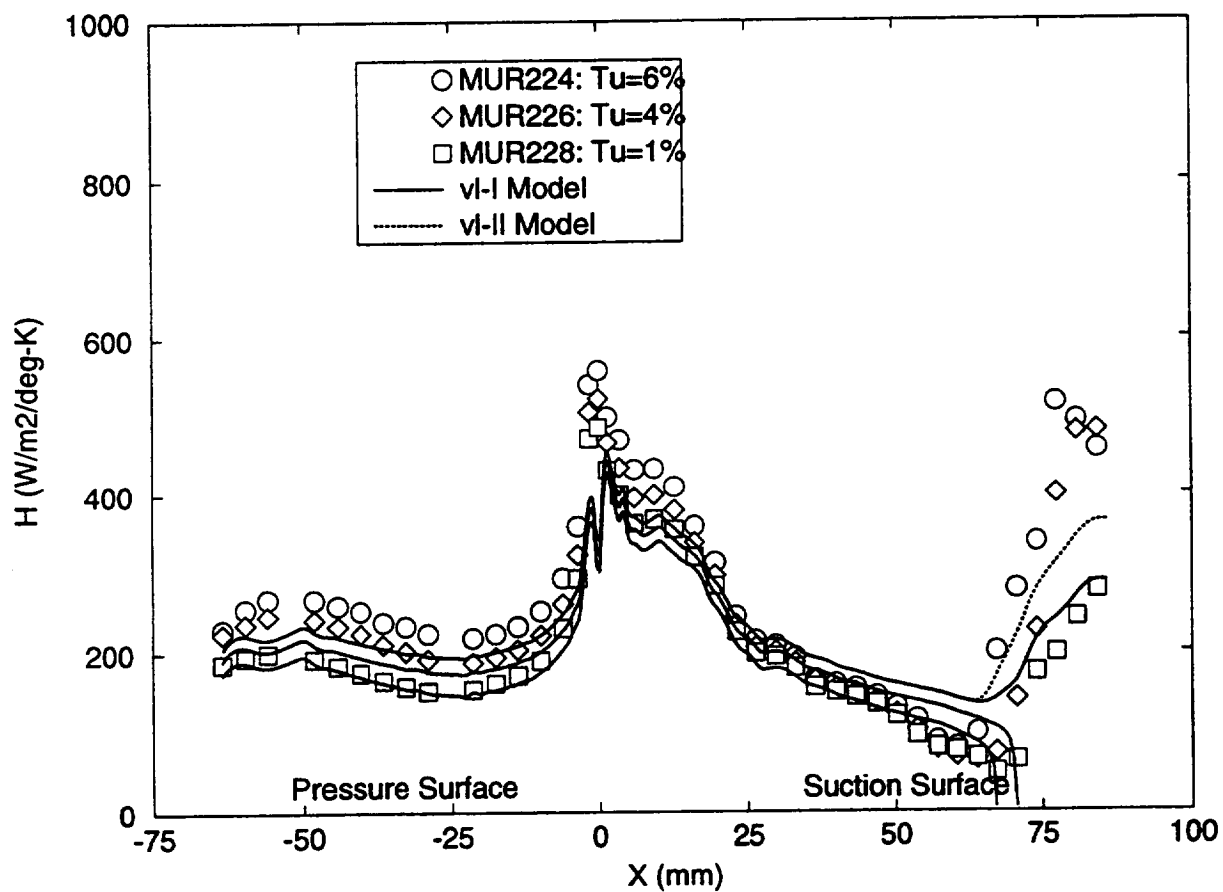


Figure 3.65 Comparison of computed VKI airfoil surface heat transfer coefficients with measured data at $Re_{C2} = 0.5 \times 10^6$, $M_2 = 0.9$, and $Tu = 1\% - 6\%$.

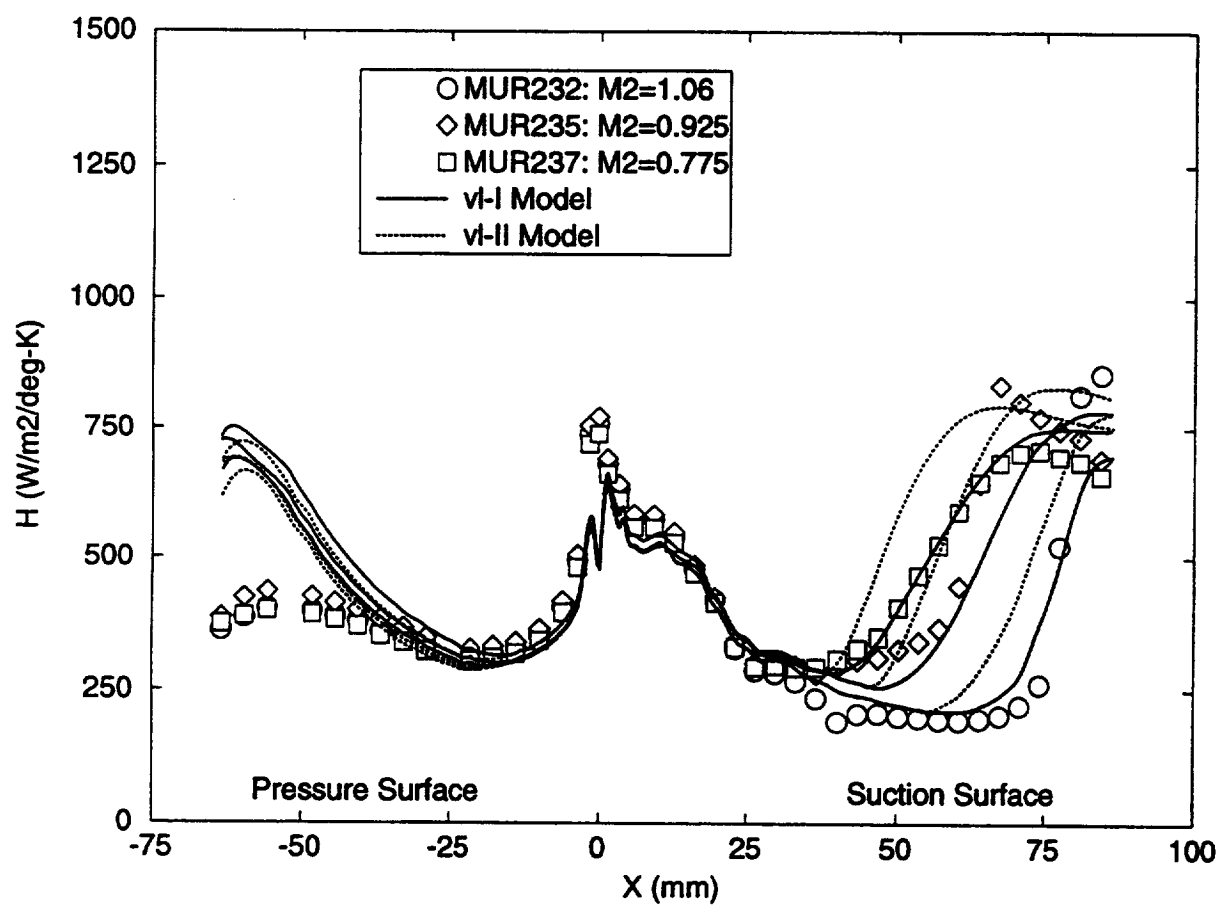


Figure 3.66 Comparison of computed VKI airfoil surface heat transfer coefficients with measured data at $Re_{C2} = 1.0 \times 10^6$, $T_u = 6\%$, and $M_2 = 0.78 - 1.06$.

IV. Conclusions

In this study, two k - ϵ base velocity and length scale closure models were successfully developed. In the first model designated $v'l$ -I, the velocity scale of the eddy viscosity formulation was evaluated from integrating the normal component energy spectrum; and the length scale from the local distance from the wall. The energy spectrum was based on the local dissipation rate. In the second ($v'l$ -II) model, the velocity scale was written in a combination of simplified integral formulations of the energy spectrum and the local length and time scales; and the length scale from the conventional scale of $k^{3/2}/\epsilon$ coupled with a wall blocking of $(y/\eta_K)^{4/3}$ and the local distance from the wall of ky . The kinetic energy and dissipation rate were obtained from a modeled form of k and ϵ transport equations.

These models were tested in various turbulent flows including non-equilibrium, anisotropic flows. The results showed that the proposed velocity and length scale approaches provided substantial improvements in the flow prediction, especially for the non-equilibrium, anisotropic flows tested. Existing k - ϵ models including the Durbin's relaxation models failed to predict such non-equilibrium, anisotropic flows. The good performance of the proposed models resulted from the velocity scale and length scale formulations, which constrained the eddy diffusivity to physically realizable levels, and accounted for the reduced mixing more adequately.

The base low Reynolds number k - ϵ model, which provided a basis to developing the velocity and length scale closure models, took advantage of improvements by Durbin[8] and Yang and Shih[7]. The model was formulated by combining the k and ϵ transport equations of Durbin and the conventional form of eddy viscosity equation with the Yang and Shih damping function. The base k - ϵ provided generally similar quality solutions to Durbin's and often better than conventional k - ϵ models. However, this model's prediction for non-equilibrium, anisotropic turbulent flows was degraded as were other k - ϵ based models.

For airfoil heat transfer predictions, a set of simple correlations for laminar-turbulent transition and laminar heat transfer augmentation induced by the presence of the freestream turbulence was presented. For the transition prediction, the Mayle correlation was modified such that, for low turbulence level, the modified correlation behaved similarly to the Abu-Ghannam and Shaw correlation; while, for high turbulence levels, it asymptotically approaches Mayle's. The augmentation correlation was written in terms of the freestream turbulence level, Tu_{Ue} , the energy scale, Lu , and the wall blocking correction, $(y/Lu)^{4/3}$, as observed experimentally. These correlations

were tested for three different airfoils with various flow conditions. The calculated surface heat transfer was generally satisfactory.

References

1. Rudey, R. A., and Graham, R. W., "A Review of NASA Combustor and Turbine Heat Transfer Research," ASME Paper 84-GT-113.
2. Moffat, R. J., "Turbine Blade Cooling," Heat Transfer and Fluid Flow in Rotating Machinery, edited by Wen-Jei Yang, Hemisphere Publishing Corporation, 1985, p. 3.
3. Launder, B. E., and Spalding, D. B., 1974, "The Numerical Computation of Turbulent Flow," *Computer Methods in Applied Mechanics and Engineering*, Vol. 3, p. 269.
4. Jones, W. P., and Launder, B. E., 1973, "The Calculation of Low-Reynolds Number Phenomena with a Two-Equation Model of Turbulence," *Int. J. Heat and Mass Transfer*, Vol. 16, p.1119.
5. Wilcox, D. C., "Reassessment of the Scale Determining Equation for Advanced Turbulence Models," *AIAA Journal*, Vol. 26, No. 11, November 1988, pp. 1299-1310.
6. Yakhot, V., and Orszag, S. A., 1986, "Renormalization Group Analysis of Turbulence. I. Basic Theory," *J. Scientific Computing*, Vol.1, No. 1, p.1.
7. Yang, Z., and Shih, T. H., 1993, "New Time Scale Based k- ϵ Model for Near-Wall Turbulence," *AIAA Journal*, Vol. 31, No. 7, p. 1191.
8. Durbin, P. A., 1993 "Application of a Near-Wall Turbulence Model to Boundary Layers and Heat Transfer," *Int. J. Heat and Fluid Flow*, Vol. 14, No. 4, pp. 316-323.
9. Speziale, C. G., and Thangam, S., 1992, "Analysis of an RNG Based Turbulence Model for Separated Flows," NASA CR-189600, January 1992.
10. Ames, F. E., 1994, "Experimental Study of Vane Heat Transfer and Aerodynamics at Elevated Levels of Turbulence," NASACR-4633, November, 1994.
11. Cebeci, T., and Smith, A. M. O., 1974, Analysis of Turbulent Boundary Layers, Academic Press, New York.
12. Kays, W. M., and Crawford, M. E., 1980, Convective Heat and Mass Transfer, McGraw-Hill, New York.
13. Kwon, O. K., Turner, E. R., and Kou, Y. M., 1983, "Prediction of Stagnation Flow Heat Transfer on Turbomachinery Airfoils," AIAA Paper No. 83-1173.
14. Kwon, O. K., and Pletcher, R. H., 1983, "Prediction of Sudden Expansion Flows Using the Boundary Equations," ASME Paper No. 83-FE-11.

15. Durbin, P. A., 1991 "Near-Wall Turbulence Closure Modeling Without Damping Functions," *Theoretical and Computational Dynamics*, Vol. 3, p. 1.
16. Spalart, P. R., 1988, "Direct Simulation of a Turbulent Boundary Layer up to $Re_\theta = 1410$," *J. Fluid Mech*, Vol. 187, p.61.
17. Anderson, D. A., Tannehill, J. C., and Pletcher, R. H., 1984, Computation Fluid Mechanics and Heat Transfer, Hemisphere Publishing Corporation, Washington.
18. Tennekes, H., and Lumley, J. L., 1972, A First Course in Turbulence, the MIT Press, Cambridge, Massachusetts.
19. Hunt, J. C. R., and Graham, J. M. R., 1978, "Free-Stream Turbulence Near Plane Boundaries," *J. Fluid Mech*, Vol. 84, p. 209.
20. Thomas, N. H., and Hancock, P. E., 1977, "Grid Turbulence Near a Moving Wall," *J. Fluid Mech*, Vol. 82, Part 3, p. 481.
21. Ames, F. E., and Moffat, R. J., 1990, "Heat Transfer with High Intensity, Large Scale Turbulence: The Flat Plate Turbulent Boundary Layer and the Cylindrical Stagnation Point," Report No., HMT-44, Thermosciences Division of Mechanical Engineering, Stanford University.
22. Hinze, J., 1975, Turbulence, 2nd Ed., McGraw-Hill, New York.
23. Kim, J., Moin, P., and Moser, R., 1987, "Turbulence Statistics in Fully Developed Channel Flow at Low Reynolds Number," *Journal of Fluid Mechanics*, Vol. 177, p. 133.
24. Kim, J., and Moin, P., 1989, "Transport of Passive Scalars in a Turbulent Channel Flow," *Turbulent Shear Flows*, 6, p.85.
25. Wiegardt, K., and Tillmann, W., 1969, "Equilibrium Boundary Layer of Constant Pressure," Computation of Turbulent Boundary Layers-1968 AFSOR-IFP-Stanford Conference, edited by D. E. Coles and E. A. Hirst, Vol. 2, Stanford Univ., Stanford, CA, p. 98.
26. Purtell, L. P., Klebanoff, S., and Buckley, F. T., 1981, "Turbulent Boundary Layer at Low Reynolds Number, *Physics of Fluids*, Vol. 24, p.802.
27. Herring, H., and Norbury, J., 1969, "Equilibrium Boundary Layer in Mild Negative Pressure Gradient," Computation of Turbulent Boundary Layers-1968 AFSOR-IFP-Stanford Conference, edited by D. E. Coles and E. A. Hirst, Vol. 2, Stanford Univ., Stanford, CA, p. 249.

28. Herring, H., and Norbury, J., 1969, "Boundary Layer in Strong Negative Pressure Gradient," Computation of Turbulent Boundary Layers-1968 AFSOR-IFP-Stanford Conference, edited by D. E. Coles and E. A. Hirst, Vol. 2, Stanford Univ., Stanford, CA, p. 259.
29. Launder, B. E., and Sharma, B. I., 1974, "Application of the Energy-dissipation Model of Turbulence to the Calculation of Flow near a Spinning Disc," *Letters in Heat and Mass Transfer*, Vol. 1, p. 131.
30. Bradshaw, P., 1969, "Equilibrium Boundary Layer in Mild Positive Pressure Gradient," Computation of Turbulent Boundary Layers-1968 AFSOR-IFP-Stanford Conference, edited by D. E. Coles and E. A. Hirst, Vol. 2, Stanford Univ., Stanford, CA, p. 233.
31. Bradshaw, P., 1969, "Equilibrium Boundary Layer in Moderate Positive Pressure Gradient," Computation of Turbulent Boundary Layers-1968 AFSOR-IFP-Stanford Conference, edited by D. E. Coles and E. A. Hirst, Vol. 2, Stanford Univ., Stanford, CA, p. 241.
32. Bradshaw, P., 1969, "Boundary Layer, Initially at Constant Pressure, Developing into Equilibrium Flow in Moderate Positive Pressure Gradient," Computation of Turbulent Boundary Layers-1968 AFSOR-IFP-Stanford Conference, edited by D. E. Coles and E. A. Hirst, Vol. 2, Stanford Univ., Stanford, CA, p. 322.
33. Samuel, A. E., and Joubert, P. N., 1974, "A Boundary Layer Developing in an Increasingly Adverse Pressure Gradient," *J. Fluid Mech*, Vol. 66, Pt. 3, p. 481.
34. Hylton, L. D., Mihelc, M. S., Turner, E. R., Nealy, D. A., and York, R. E., "Analytical and Experimental Evaluation of the Heat Transfer Distribution Over the Surfaces of Turbine Vanes," NASA CR-168015, Final Report, May 1983.
35. Emmons, H. W., 1951, "The Laminar-Turbulent Transition in Boundary Layer - Part I," *Journal of Aeronautical Science*, Vol. 18, p. 490.
36. Mayle, R. E., 1991, "The Role of Laminar-Turbulent Transition in Gas Turbine Engines," The 1991 IGTI Scholar Lecture, *J. of Turbomachinery*, Vol. 113, p. 509.
37. Turner, E. R., Wilson, M. D., Hylton, L. D., and Kaufman, R. M., "Turbine Vane External Heat Transfer, Volume 1. Analytical and Experimental Evaluation of Surface Heat Transfer Distributions with Leading Edge Showerhead Film Cooling," NASA CR-174827, Final Report, July 1985.
38. Arts, T., Lambert de Rouvroit, M., and Rutherford, A. W., 1990, "Aero-thermal Investigation of a Highly Loaded Transonic Linear Turbine Guide Vane Cascade," von Karman Institute for Fluid Dynamics, Technical Note 174.

39. Schmidt, R. C., and Patankar, S. V., 1988, "Two-Equation Low-Reynolds-Number Turbulence Modeling of Transitional Boundary Layer Flows Characteristic of Gas Turbine Blades," NASA Contract Report 4145, May 1988.
40. Rodi, W., and Scheuerer, G., 1985, "Calculation of Heat Transfer to Convection-Cooled Gas Turbine Blades," *J. of Engineering for Gas Turbines and Power*, Vol. 107, p. 20.

APPENDIX A. Initial Profiles

This Appendix presents two procedures for generating the starting boundary layer profiles of U , H , k and ϵ . These procedures were developed for two-dimensional non-similar laminar and turbulent flows, respectively, based on the assumption that the mass, momentum, and energy conservation equations were uncoupled. Although such an assumption might result in generating inaccurate profiles, it was introduced for the simplicity of the procedures. For two-dimensional similar flows, the velocity and enthalpy (or temperature) profiles should be generated by using a similarity analysis which can be found in elsewhere [13].

1. Laminar Flow.

The initial profiles for laminar flows can be generated similarly to the procedure suggested by Smith and Patankar[39]. The U -velocity profile was assumed to be represented by the Pohlhausen polynomial as,

$$\begin{aligned} \frac{U}{U_e} = & \left[2 \left(\frac{y}{\delta} \right) - 2 \left(\frac{y}{\delta} \right)^3 + \left(\frac{y}{\delta} \right)^4 \right] \\ & + \frac{\Lambda}{6} \left[\left(\frac{y}{\delta} \right) - 3 \left(\frac{y}{\delta} \right)^2 + 7 \left(\frac{y}{\delta} \right)^3 - \left(\frac{y}{\delta} \right)^4 \right] \end{aligned} \quad (A-1)$$

where δ denotes the boundary layer thickness; U_e , the freestream velocity; y , the local normal coordinate; and Λ , an acceleration parameter defined by

$$\Lambda = \frac{\delta^2}{\nu} \frac{\partial U_e}{\partial x} \quad (A-2)$$

The Pohlhausen polynomial, Equations (A-1), provides the following correlation for the boundary layer thickness parameter;

$$\frac{\theta}{\delta} = \frac{1}{63} \left(\frac{37}{5} - \frac{\Lambda}{15} - \frac{\Lambda^2}{144} \right) \quad (A-3)$$

where θ denotes the momentum thickness. From Equations (A-1) to (A-3), the velocity profile can be obtained provided that the local boundary layer momentum thickness, θ , and the freestream velocity, U_e , are given. The freestream velocities are generally known in advance. The momentum thickness can be estimated by applying Thwaites method, which requires integration of the following approximate relationship;

$$\theta^2 = \frac{0.45 \nu}{U_e^6} \int_0^x U_e^5 dx \quad (A-4)$$

The starting enthalpy profile was derived from the approximate temperature-velocity relationship given below;

$$T = T_w + (T_e - T_w) \frac{U}{U_e} \left[\frac{y}{\delta_T} \right] \quad (A-5)$$

where the term $U/U_e [y/\delta_T]$ implies that δ_T has replaced δ in Equation (A-1). The subscripts w and e denote the wall and freestream conditions, respectively. The thermal boundary layer δ_T at the starting point x_i is evaluated from the following approximate relationship;

$$\delta_T = \frac{\delta}{1.026 \text{Pr}^{1/3}} \left[1 - \left(\frac{x_0}{x_i} \right)^{3/4} \right]^{1/3} \quad (A-6)$$

where x_0 denotes the unheated starting length. When x_i is less than x_0 , the wall is assumed to be adiabatic; T_w is set equal to T_e . The total enthalpy profile is then obtained by using the total enthalpy definition;

$$H = c_p T + \frac{U^2}{2} \quad (A-7)$$

The initial profiles for k and ϵ in the laminar region are specified as proposed by Rodi and Scheuerer [40];

$$k = k_e \left(\frac{U}{U_e} \right)^2 \quad (A-8)$$

$$\epsilon = b_1 k \frac{\partial U}{\partial y}, \quad \epsilon > \epsilon_e \quad (A-9)$$

where the constant b_1 is set equal to 1.0 as suggested by Schmidt and Patankar [39]. The subscript e denotes the freestream condition.

2. Turbulent Flow.

For two-dimensional turbulent boundary layers, the shear stress can be written as;

$$\tau = \mu \frac{\partial U}{\partial y} - \overline{\rho u'v'} \quad (\text{A-10})$$

where τ denotes the shear stress; μ , the molecular viscosity; ρ , the density; U , the mean velocity; y , the normal coordinate; and $-\overline{\rho u'v'}$, the Reynolds stress. The Prandtl's mixing length theory provides

$$-\overline{\rho u'v'} = \rho l_m^2 \left(\frac{dU}{dy} \right)^2 \quad (\text{A-11})$$

where l_m denotes the mixing length. Using Equation (A-11), Equations (A-10) can be rewritten as

$$\mu \frac{dU}{dy} + \rho l_m^2 \left(\frac{dU}{dy} \right)^2 = \tau \quad (\text{A-12})$$

Solving this quadratic equation for (du/dy) and rewriting in dimensionless variables gives

$$\frac{dU^+}{dy^+} = \frac{-1 + \sqrt{1 + 4l_m^{+2} \left(\frac{\tau}{\tau_w} \right)}}{2l_m^{+2}} \quad (\text{A-13})$$

with

$$U^+ = \frac{U}{u_\tau} \quad (\text{A-14})$$

$$y^+ = \frac{u_\tau y}{\nu} \quad (\text{A-15})$$

$$l_m^+ = \frac{u_\tau l_m}{\nu} \quad (\text{A-16})$$

where $\tau_w (\equiv \rho u_\tau^2)$ denotes the wall shear stress; and u_τ , the friction velocity. The shear stress profile and the mixing length can be written in the following form;

$$\frac{\tau}{\tau_w} = 1 - \left(\frac{y}{\delta}\right)^{9/7} \quad (\text{A-17})$$

$$l_m = \min \left[\kappa y \left\{ 1 - \exp\left(-\frac{y^+}{25}\right) \right\}, 0.85 \theta \right] \quad (\text{A-18})$$

where κ denotes the von Karman constant; and θ , the momentum thickness.

For two-dimensional turbulent boundary layers, the friction coefficient can be written in terms of a Reynolds number based on local momentum thickness as [12];

$$\frac{c_f}{2} = 0.0125 \text{Re}_\theta^{-1/4} \quad (\text{A-19})$$

with the momentum thickness as

$$\frac{\theta}{x} = 0.036 \text{Re}_x^{-0.2} \quad (\text{A-20})$$

Since the skin friction is defined as

$$u_\tau = U_e \left(\frac{c_f}{2} \right)^{1/2} \quad (\text{A-21})$$

By assuming that $\theta = \delta/9$ based on the Spalart's direct numerical simulation for $\text{Re}_\theta = 1410$, Equation (A-13) along with Equations (A-17)-(A-21) can be integrated from wall to the boundary layer edge to generate the starting velocity profile.

For the starting enthalpy profile, the thermal boundary layer thickness is approximated based on the power law as;

$$\delta_T = \delta \left[1 - \left(\frac{x_0}{x} \right)^{9/10} \right]^{7/9} \quad (\text{A-22})$$

where δ_T denotes the thermal boundary layer thickness; δ , the hydrodynamic boundary layer thickness; x , the axial coordinate; and x_0 , the extent of the unheated region. The temperature profile is assumed to be represented by the power law

$$\frac{T_w - T}{T_w - T_e} = \left(\frac{y}{\delta_T} \right)^{1/7} \quad (\text{A-23})$$

The total enthalpy profile is then obtained by using Equation (A-7).

The starting profile for the kinetic energy is obtained by using the logarithmic law approximation for the outer region and a wall boundary condition for the inner region. The logarithmic law gives

$$k_o = \left(\frac{\tau}{\tau_w} \right) \frac{u_\tau^2}{\sqrt{C_\mu}} \quad (\text{A-24})$$

where the constant C_μ is set to 0.085. At the wall, the following condition is assumed to be valid;

$$\epsilon_w = 2 \nu \left(\frac{\partial k^{1/2}}{\partial y} \right)^2 \quad (\text{A-25})$$

where ϵ_w denotes the dissipation rate at the wall. Equation (A-25) can be approximated in the following form

$$k_i \approx \frac{\epsilon_w y^2}{2 \nu} \quad (\text{A-26})$$

The turbulent kinetic energy profile is then generated by taking the smaller between k_o and k_i obtained from Equation (A-24) and (A-26), respectively, that is

$$k = \min(k_i, k_o) \quad (\text{A-27})$$

The starting dissipation rate profile is generated by using the following equation which is derived based on the Spalart's direct numerical simulation data for $Re_\theta = 1410$;

$$\epsilon = \left(\frac{\tau}{\tau_w} \right) \frac{u_\tau^4}{\nu} \frac{1}{\kappa \left[y^+ + 70 \exp \left(- \frac{y^+}{10} \right) \right]} \quad (\text{A-28})$$

APPENDIX B. Airfoil Surface Velocities

This Appendix presents the airfoil surface velocity distribution for two C3X airfoils measured by Ames [10] and Turner, et al.[37], and a VKI airfoil measured by Art, et al.[38]. The velocities were calculated from an in-house stream function analysis for the low Mach number C3X airfoil measured by Ames and a two-dimensional Euler analysis for the high Mach number flow measured by Turner, et al. and Arts, et al. These velocities were used as the freestream velocity boundary condition to the boundary layer equations. The surface distance shown in the table was measured from the airfoil stagnation point.

1. C3X Airfoil Measured by Ames.

<u>Suction Surface</u>		<u>Pressure Surface</u>	
Surface Distance (cm)	Surface Velocity (m/sec)	Surface Distance (cm)	Surface Velocity (m/sec)
0.0	0.0	0.0	0.0
0.050292	1.057656	0.041666	0.920496
0.140818	3.483864	0.133350	3.096768
0.231038	7.303008	0.224790	7.443216
0.321259	11.58545	0.415534	12.91742
0.411785	15.46860	0.608076	15.98066
0.502310	18.80311	0.801624	17.27606
0.592531	21.70176	0.995934	18.06550
0.683666	24.28342	1.188964	18.66900
0.775106	26.64257	1.382024	19.24202
0.866851	29.37358	1.612148	19.88515
1.050646	33.12262	1.842760	20.58314
1.234135	37.67023	2.073646	21.30857
1.417625	42.75125	2.300722	22.05228
1.602638	48.60036	2.527554	22.80818

Suction Surface

Surface Distance (cm)	Surface Velocity (m/sec)
1.788262	55.33034
1.974190	63.51118
2.224430	73.78903
2.474671	86.53577
2.723693	98.60585
3.054401	108.6795
3.389071	117.9485
3.724046	124.6845
4.030370	128.5677
4.335475	129.4608
4.640580	127.6380
5.022190	123.7884
5.404409	119.2835
5.787542	114.5682
6.142634	110.9533
6.497117	108.0364
6.851294	105.4578
7.273442	103.2571
7.695895	101.5898
8.118348	99.93173
8.739226	98.46259
9.360103	97.39884
9.980981	96.63074
10.58174	96.14002
11.18250	95.81388
11.78326	95.62186
12.34684	95.53651
12.91041	95.53346
13.47399	95.61881
14.01867	95.81693
14.56365	95.99676
15.10833	95.79559
16.10045	95.03969
17.09257	93.79610

Pressure Surface

Surface Distance (cm)	Surface Velocity (m/sec)
2.754112	23.49398
2.889748	24.03348
3.025140	24.49982
3.160776	24.97531
3.296168	25.46299
3.431286	25.95982
3.566678	26.49626
3.724656	27.09062
3.882390	27.72461
4.040368	28.47442
4.288536	29.44673
4.536948	30.57144
4.785360	32.02534
5.238232	34.14674
5.691378	36.70402
6.144250	39.59962
6.645158	42.97070
7.146036	46.74108
7.646914	50.87417
8.150352	55.33949
8.653790	60.08827
9.156954	65.05042
9.662160	70.12534
10.16737	75.10577
10.67257	80.95488
11.58292	88.36152
12.49323	95.85046
13.40434	119.4877

2. C3X Airfoil Measured by Turner, et al.

<u>Suction Surface</u>		<u>Pressure Surface</u>	
Surface Distance (cm)	Surface Velocity (m/sec)	Surface Distance (cm)	Surface Velocity (m/sec)
0.0	0.0	0.0	0.0
0.011735	1.010564	0.011735	1.010564
0.080437	7.858201	0.308397	25.61506
0.442935	46.22996	0.769498	43.87398
0.796077	81.19296	1.117488	50.10440
1.176589	110.1041	1.405677	53.88325
1.321491	121.5721	2.144085	62.71425
1.550487	141.2529	2.915077	72.43526
1.894820	179.6716	3.677107	82.64180
2.199620	217.6802	4.405122	93.96731
2.473269	260.3564	5.086502	106.0568
2.719578	297.6505	5.717560	119.1889
2.947142	331.5757	6.299698	132.9646
3.159191	368.4648	6.836542	147.5510
3.361426	395.3240	7.332604	162.5862
3.557229	415.3274	7.792913	178.1309
3.746510	440.9708	8.221980	193.9081
3.933871	458.2034	8.623767	209.9989
4.120896	466.2768	9.001780	226.0300
4.306915	477.5640	9.359463	242.0950
4.493941	486.8429	9.699254	257.7801
4.683801	487.6681	10.02338	273.2672
4.876404	487.7892	10.33360	288.0142
5.072177	488.8423	10.63173	302.5229
5.272430	485.0663	10.91870	315.8881
5.477835	479.7714	11.19518	329.2098
5.688330	475.9730	11.46203	340.8785
5.904799	469.6762	11.71910	353.1521
6.128583	463.8851	11.96642	362.9300
6.359347	458.6872	12.20313	374.6560

<u>Suction Surface</u>		<u>Pressure Surface</u>	
Surface Distance (cm)	Surface Velocity (m/sec)	Surface Distance (cm)	Surface Velocity (m/sec)
6.598371	453.4477	12.42996	382.5110
6.847454	448.5242	12.64204	395.4759
7.105863	445.0139	12.83711	403.3124
7.377684	440.3892	13.01389	424.7910
7.662428	437.1895	13.17099	447.1755
7.964820	432.8197	13.30458	537.5836
8.286476	430.3899	13.38779	487.7935
8.633308	427.3025	13.46003	301.9295
9.008120	427.3310	13.53041	49.50016
9.419387	426.8260	13.60414	211.6049
9.871862	429.2386	13.68576	424.3395
10.37320	430.5925	13.78248	551.5895
10.93086	433.7928		
11.55015	436.3305		
12.23263	440.1463		
12.97320	444.4038		
13.75745	448.8682		
14.55947	454.0547		
15.34360	458.3140		
16.07232	461.1491		
16.71481	464.7768		
17.25107	465.0763		
17.65856	470.4713		
17.96967	487.9197		
18.17440	551.5895		

3. VKI Airfoil Measured by Arts, et al.

(1) For MUR129, 217, and 235

<u>Suction Surface</u>		<u>Pressure Surface</u>	
Surface Distance (cm)	Surface Velocity (m/sec)	Surface Distance (cm)	Surface Velocity (m/sec)
0.0	0.0	0.0	0.0
0.053584	6.105144	0.052060	5.519928
0.106924	16.20622	0.107442	13.73429
0.160020	27.91663	0.163586	21.61032
0.212598	37.11550	0.219974	27.36799
0.265420	44.80255	0.331226	31.29382
0.318516	51.63922	0.441442	34.16198
0.371612	58.42711	0.551444	36.87166
0.424678	67.09258	0.658124	39.37711
0.532882	78.64450	0.765048	41.64178
0.641604	90.60180	0.872246	43.71137
0.751332	103.0072	0.978164	45.63466
0.863102	117.5553	1.084082	47.45126
0.974354	134.9563	1.190000	49.11547
1.084844	154.0673	1.274308	50.56632
1.206764	173.3459	1.358646	51.91658
1.329446	192.2587	1.443228	53.22113
1.452616	211.7781	1.516898	54.44033
1.568958	232.5014	1.590538	55.61990
1.685026	254.6574	1.664452	56.79642
1.800362	275.2862	1.738122	57.97296
1.938010	292.0014	1.811792	59.14034
2.076206	308.2747	1.885432	60.34735
2.214616	317.9643	1.969770	61.63666
2.399294	322.0761	2.054108	62.97168

Suction Surface

Surface Distance (cm)	Surface Velocity (m/sec)
2.583942	326.5902
2.769352	327.1114
2.960126	331.6864
3.150352	340.2147
3.341126	348.1578
3.619500	355.5583
3.898392	363.7910
4.177528	369.6675
4.410700	374.6449
4.644146	378.5494
4.877318	380.7165
5.153924	382.5697
5.430530	383.1214
5.707136	382.2619
5.962894	379.7778
6.218926	375.2576
6.474958	369.7346
6.718554	363.6874
6.962150	356.8934
7.205716	348.8924
7.679954	339.6783
8.154162	332.4515
8.628126	341.7387

Pressure Surface

Surface Distance (cm)	Surface Velocity (m/sec)
2.138172	64.62065
2.296424	66.93713
2.454646	69.74129
2.612654	72.82891
2.771638	76.23048
2.930652	79.98257
3.089666	84.56981
3.303788	90.59875
3.517636	97.81337
3.731758	106.0094
3.948440	115.3820
4.165092	126.0439
4.381744	138.2878
4.600438	152.3817
4.819132	168.1795
5.037826	189.9209
5.468874	222.6716
5.899922	261.5641
6.331458	348.1334

(2) For MUR224, 226, and 228

<u>Suction Surface</u>		<u>Pressure Surface</u>	
Surface Distance (cm)	Surface Velocity (m/sec)	Surface Distance (cm)	Surface Velocity (m/sec)
0.0	0.0	0.0	0.0
0.053584	6.025896	0.052060	5.446776
0.106924	15.99286	0.107442	13.55446
0.160020	27.25217	0.163586	21.32990
0.212598	36.63086	0.219974	27.01138
0.265420	44.21734	0.331226	30.88538
0.318516	50.96561	0.441442	33.71698
0.371612	57.66511	0.551444	36.39312
0.424678	66.22085	0.658124	38.86200
0.532882	77.62037	0.765048	41.09923
0.641604	89.42222	0.872246	43.14139
0.751332	101.6660	0.978164	45.03725
0.863102	116.0252	1.084082	46.83252
0.974354	133.1976	1.190000	48.47539
1.084844	152.0586	1.274308	49.90795
1.206764	171.0873	1.358646	51.23993
1.329446	189.7532	1.443228	52.52923
1.452616	209.0196	1.516898	53.73014
1.568958	229.4717	1.590538	54.89448
1.685026	251.3381	1.664452	56.05577
1.800362	271.6987	1.738122	57.21706
1.938010	288.1975	1.811792	58.36920
2.076206	304.2575	1.885432	59.56097
2.214616	313.8221	1.969770	60.83503
2.399294	317.8790	2.054108	62.15177
2.583942	322.3351	2.138172	63.77940
2.769352	322.8503	2.296424	66.06235
2.960126	327.3643	2.454646	68.83298
3.150352	335.7799	2.612654	71.88098
3.341126	343.6224	2.771638	75.23683

Suction Surface

Surface Distance (cm)	Surface Velocity (m/sec)
3.619500	350.9254
3.898392	359.0514
4.177528	364.8517
4.410700	369.7651
4.644146	373.6147
4.877318	375.7544
5.153924	377.5862
5.430530	378.1318
5.707136	377.2814
5.962894	374.8308
6.218926	370.3655
6.474958	364.9188
6.718554	358.9508
6.962150	352.2452
7.205716	344.3448
7.679954	335.2526
8.154162	328.1202
8.628126	337.2856

Pressure Surface

Surface Distance (cm)	Surface Velocity (m/sec)
2.930652	78.94015
3.089666	83.46643
3.303788	89.41918
3.517636	96.53930
3.731758	104.6287
3.948440	113.8794
4.165092	124.4011
4.381744	136.4833
4.600438	150.3975
4.819132	165.9880
5.037826	187.4459
5.468874	219.7730
5.899922	258.1534
6.331458	343.5980

(3) For MUR239, 245, and 247

<u>Suction Surface</u>		<u>Pressure Surface</u>	
Surface Distance (cm)	Surface Velocity (m/sec)	Surface Distance (cm)	Surface Velocity (m/sec)
0.0	0.0	0.0	0.0
0.053584	6.096000	0.052060	5.504688
0.106924	16.16659	0.107442	13.69162
0.160020	27.53868	0.163586	21.54022
0.212598	37.01491	0.219974	27.27960
0.265420	44.68063	0.331226	31.19628
0.318516	51.49596	0.441442	34.05835
0.371612	58.26557	0.551444	36.76193
0.424678	66.90665	0.658124	39.25824
0.532882	78.42504	0.765048	41.51681
0.641604	90.34577	0.872246	43.58030
0.751332	102.7176	0.978164	45.49750
0.863102	117.2230	1.084082	47.31106
0.974354	134.5753	1.190000	48.96917
1.084844	153.6283	1.274308	50.41697
1.206764	172.8521	1.358646	51.76418
1.329446	191.7070	1.443228	53.06568
1.452616	211.1654	1.516898	54.28183
1.568958	231.8248	1.590538	55.45531
1.685026	253.9075	1.664452	56.63184
1.800362	274.4602	1.738122	57.80227
1.938010	291.1145	1.811792	58.96661
2.076206	307.3176	1.885432	60.17057
2.214616	316.9585	1.969770	61.45682
2.399294	321.0550	2.054108	62.78880
2.583942	325.5447	2.138172	64.43167
2.769352	326.0628	2.296424	66.74206
2.960126	330.6044	2.454646	69.54012
3.150352	339.0534	2.612654	72.61860
3.341126	346.8868	2.771638	76.00798

Suction Surface

Surface Distance (cm)	Surface Velocity (m/sec)
3.619500	354.1746
3.898392	362.2914
4.177528	368.0430
4.410700	372.8466
4.644146	376.4859
4.877318	378.3635
5.153924	379.8600
5.430530	380.0582
5.707136	378.9274
5.962894	376.2969
6.218926	371.7889
6.474958	366.4306
6.718554	360.6637
6.962150	354.2172
7.205716	346.6551
7.679954	337.9348
8.154162	331.0555
8.628126	340.6140

Pressure Surface

Surface Distance (cm)	Surface Velocity (m/sec)
2.930652	79.75092
3.089666	84.32292
3.303788	90.33358
3.517636	97.52686
3.731758	105.6985
3.948440	115.0437
4.165092	125.6721
4.381744	137.8732
4.600438	151.9245
4.819132	167.6705
5.037826	189.3357
5.468874	221.9736
5.899922	260.7015
6.331458	346.8319

(4) For MUR232

<u>Suction Surface</u>		<u>Pressure Surface</u>	
Surface Distance (cm)	Surface Velocity (m/sec)	Surface Distance (cm)	Surface Velocity (m/sec)
0.0	0.0	0.0	0.0
0.053340	6.059424	0.052334	5.568696
0.106680	16.33118	0.107686	14.00556
0.159502	27.93187	0.160782	22.06752
0.212354	37.58489	0.220218	27.93187
0.264932	45.37862	0.331470	31.89122
0.318272	52.30978	0.441716	34.77463
0.371338	59.20130	0.551688	37.52393
0.424190	68.01307	0.658368	40.07206
0.532394	79.74787	0.765292	42.37330
0.641360	91.86672	0.872490	44.47032
0.751088	104.4580	0.978408	46.42104
0.862828	119.2347	1.084326	48.26508
0.974080	136.8887	1.190244	49.95672
1.084570	156.3197	1.274582	51.43195
1.193810	175.9306	1.359164	52.80660
1.329172	195.1787	1.443472	54.13248
1.452372	215.0669	1.517142	55.36997
1.568714	236.2291	1.591056	56.56783
1.684538	258.9124	1.664726	57.76570
1.800088	280.1783	1.738366	58.96051
1.937522	297.5000	1.812036	60.15228
2.075932	314.5262	1.885706	61.38062
2.214372	325.0143	1.970014	62.69431
2.399020	329.7418	2.054352	64.05372
2.583698	335.1703	2.138416	65.73012
2.769108	336.4626	2.296668	68.08927
2.959852	342.3544	2.454890	70.94830
3.150108	353.2784	2.613142	74.09383
3.340364	365.0041	2.771912	77.56246

Suction Surface

Surface Distance (cm)	Surface Velocity (m/sec)
3.618982	376.7877
3.898148	388.1780
4.177040	393.6644
4.410456	398.5656
4.643628	404.5519
4.877044	409.3860
5.153650	415.5521
5.430012	421.3403
5.706618	426.8114
5.962650	432.3100
6.218682	435.5714
6.474714	437.4276
6.718310	437.5648
6.961876	434.3674
7.205472	424.7175
7.679680	398.5809
8.153644	358.5058
8.627882	347.7433

Pressure Surface

Surface Distance (cm)	Surface Velocity (m/sec)
2.930896	81.38770
3.089910	86.06638
3.304032	92.22029
3.518154	99.58730
3.732032	107.9632
3.948684	117.5522
4.165336	128.4671
4.382018	141.0249
4.600712	155.4998
4.819406	171.7792
5.038100	194.2704
5.469118	228.4324
5.900166	269.7968
6.331702	362.9497

(5) For MUR237

<u>Suction Surface</u>		<u>Pressure Surface</u>	
Surface Distance (cm)	Surface Velocity (m/sec)	Surface Distance (cm)	Surface Velocity (m/sec)
0.0	0.0	0.0	0.0
0.054346	6.166104	0.051572	5.394960
0.107686	15.91970	0.106924	13.17041
0.160508	26.91079	0.162824	20.67154
0.213116	36.06698	0.219456	26.20061
0.265938	43.47972	0.330464	30.02890
0.319034	50.07864	0.440954	32.84525
0.372374	56.63489	0.550926	35.47872
0.425196	65.00774	0.657606	37.89883
0.533400	76.16342	0.764530	40.08730
0.642366	87.70315	0.871484	42.09288
0.752094	99.68789	0.977402	43.95521
0.863834	113.7392	1.083320	45.71695
0.974842	130.5154	1.189208	47.32630
1.085332	148.9100	1.273820	48.73447
1.207252	167.4327	1.358128	50.03902
1.330208	185.5744	1.442466	51.30089
1.453378	204.2556	1.516380	52.48046
1.569720	224.0097	1.590050	53.62042
1.685544	244.9739	1.663690	54.75732
1.800850	264.2738	1.737604	55.89422
1.938528	279.6967	1.811274	57.02198
2.076968	294.4094	1.884944	58.18937
2.215378	302.5811	1.969008	59.43600
2.399782	305.5163	2.053346	60.72530
2.584704	308.2107	2.137654	62.31636
2.769870	307.1378	2.295662	64.55054
2.960614	309.1251	2.453884	67.25412
3.151114	313.5630	2.612136	70.22897
3.341126	316.2300	2.771150	73.50252

Suction Surface

Surface Distance (cm)	Surface Velocity (m/sec)
3.620018	318.2325
3.898910	321.0519
4.178046	322.5516
4.411462	323.0819
4.644634	322.5698
4.877806	321.3324
5.154412	320.0674
5.431018	318.5160
5.707624	316.6628
5.963656	314.3189
6.219444	311.4416
6.475476	308.3753
6.719072	305.2359
6.962638	301.9105
7.206234	298.1858
7.680442	294.0924
8.154680	291.0962
8.628888	303.5503

Pressure Surface

Surface Distance (cm)	Surface Velocity (m/sec)
2.930134	77.11135
3.089148	81.51571
3.303026	87.29777
3.517148	94.20758
3.731270	102.0409
3.945636	110.9777
4.164574	121.1184
4.380982	132.7221
4.599676	146.0297
4.818370	160.8521
5.037064	181.0664
5.468112	210.9765
5.899404	245.1659
6.330696	318.9549

REPORT DOCUMENTATION PAGE			Form Approved OMB No. 0704-0188	
Public reporting burden for this collection of information is estimated to average 1 hour per response, including the time for reviewing instructions, searching existing data sources, gathering and maintaining the data needed, and completing and reviewing the collection of information. Send comments regarding this burden estimate or any other aspect of this collection of information, including suggestions for reducing this burden, to Washington Headquarters Services, Directorate for Information Operations and Reports, 1215 Jefferson Davis Highway, Suite 1204, Arlington, VA 22202-4302, and to the Office of Management and Budget, Paperwork Reduction Project (0704-0188), Washington, DC 20503.				
1. AGENCY USE ONLY (Leave blank)		2. REPORT DATE July 1995		3. REPORT TYPE AND DATES COVERED Final Contractor Report
4. TITLE AND SUBTITLE Advanced k-epsilon Modeling of Heat Transfer			5. FUNDING NUMBERS WU-505-62-10 C-NAS3-25950 (Task 14)	
6. AUTHOR(S) Okey Kwon and Forrest E. Ames				
7. PERFORMING ORGANIZATION NAME(S) AND ADDRESS(ES) Allison Engine Company P.O. Box 420 Indianapolis, Indiana 46206-0420			8. PERFORMING ORGANIZATION REPORT NUMBER E-9748	
9. SPONSORING/MONITORING AGENCY NAME(S) AND ADDRESS(ES) National Aeronautics and Space Administration Lewis Research Center Cleveland, Ohio 44135-3191			10. SPONSORING/MONITORING AGENCY REPORT NUMBER NASA CR-4679	
11. SUPPLEMENTARY NOTES Project Manager, John R. Schwab, Internal Fluid Mechanics Division, NASA Lewis Research Center, organization code 2640, (216) 433-8446.				
12a. DISTRIBUTION/AVAILABILITY STATEMENT Unclassified - Unlimited Subject Category 34 This publication is available from the NASA Center for Aerospace Information, (301) 621-0390.			12b. DISTRIBUTION CODE	
13. ABSTRACT (Maximum 200 words) This report describes two approaches to low Reynolds-number k-epsilon turbulence modelling which formulate the eddy viscosity on the wall-normal component of turbulence and a length scale. The wall-normal component of turbulence is computed via integration of the energy spectrum based on the local dissipation rate and is bounded by the isotropic condition. The models account for the anisotropy of the dissipation and the reduced mixing length due to the high strain rates present in the near-wall region. The turbulent kinetic energy and its dissipation rate were computed from the k and epsilon transport equations of Durbin. The models were tested for a wide range of turbulent flows and proved to be superior to other k-epsilon models, especially for nonequilibrium anisotropic flows. For the prediction of airfoil heat transfer, the models included a set of empirical correlations for predicting laminar-turbulent transition and laminar heat transfer augmentation due to the presence of freestream turbulence. The predictions of surface heat transfer were generally satisfactory.				
14. SUBJECT TERMS Turbulence modeling; Heat transfer			15. NUMBER OF PAGES 155	
			16. PRICE CODE A08	
17. SECURITY CLASSIFICATION OF REPORT Unclassified	18. SECURITY CLASSIFICATION OF THIS PAGE Unclassified	19. SECURITY CLASSIFICATION OF ABSTRACT Unclassified	20. LIMITATION OF ABSTRACT	